UCLA
UCLA Electronic Theses and Dissertations

Title

Identifying the Molecular Drivers of Cellular Senescence in Macrophages

Permalink

https://escholarship.org/uc/item/7z86q182

ISBN

9798247931980

Author

Salladay-Perez, Ivan Alexander

Publication Date

2026-05-29

Peer reviewed|Thesis/dissertation

eScholarship.org Powered by the California Digital Library
University of California

UNIVERSITY OF CALIFORNIA

Los Angeles

Identifying the Molecular Drivers of Cellular Senescence in Macrophages

A dissertation submitted in partial satisfaction

of the requirements for the degree

Doctor of Philosophy in Molecular Biology

by

Ivan Alexander Salladay-Perez

2026

© Copyright by

Ivan Alexander Salladay-Perez

2026

ABSTRACT OF THE DISSERTATION

Identifying the Molecular Drivers of Cellular Senescence in Macrophages

by

Ivan Alexander Salladay-Perez

Doctor of Philosophy in Molecular Biology

University of California, Los Angeles, 2026

Professor Anthony J. Covarrubias, Chair

Aging is characterized by chronic low-grade inflammation, termed inflammaging, which contributes to the development of metabolic and degenerative diseases. Cellular senescence is a key driver of this process; however, the identity and molecular features of senescent immune cells remain poorly defined. This dissertation investigates macrophage senescence as a central mechanism underlying immune aging. First, we establish that macrophages can undergo bona fide cellular senescence in response to DNA damage and metabolic stress, acquiring stable cell-cycle arrest and a senescence-associated secretory phenotype (SASP). Through multi-omic profiling, we identify a distinct transcriptional and metabolic signature of senescent macrophages characterized by p21 expression, type-I interferon signaling, and mitochondrial DNA–driven inflammation

We further demonstrate that excess cholesterol loading via acetylated low-density lipoprotein is sufficient to induce a stable, lipid-laden senescent macrophage phenotype, providing a reproducible experimental model for studying lipid-induced senescence. Importantly, we identify $p21^{+}TREM2^{+}$ macrophages as a major source of inflammaging in vivo, accumulating in aged and diseased tissues and contributing to metabolic dysfunction. Targeting these cells with senolytic therapies reduces inflammation and disease burden. Together, this work establishes macrophage senescence as a key driver of immune aging and highlights new therapeutic strategies to combat age-associated disease.

The dissertation of Ivan Alexander Salladay-Perez is approved.

Ajit Divakaruni

Steven J. Bensinger

Elizabeth Aguiar Vallim

Alexander Hoffmann

Anthony J. Covarrubias, Committee Chair

University of California, Los Angeles

2026

This dissertation is dedicated to:

To my wife and children, Thalia Jovana Hernandez, Jayleen Liah Lopez-Hernandez, and Arabella Evie Salladay-Hernandez. I love this family and I wouldn't trade it for anything. I appreciate every second I have with this family, my family.

To Thalia, I want to say thank you for being there with me at every step of the process. Our relationship has been through the COVID19 stay home order, two Trump terms, The death of my grandfather, a beautiful marriage, and the birth of our daughter. Let's not forget we both finished grad school together. There are days that I want to give up and fall back to something I was supposed to do like construction or roofing, but seeing you throughout the years not give up on your goals moved me to keep fighting for mine. More importantly, the day-to-day love you give me has moved me to become a better man, father, and student. If it wasn't for you I wouldn't be in the position that I'm in today. I love you endlessly, and having you in my life reminds me that no challenge feels impossible when we face it together.

To Jayleen and Arabella. You are the best daughters any father can ask for. Seeing you two happy and excited for the day fills my heart with a warmth I have never felt before. I am getting my PhD soon and you guys may not know what it means, but I hope in the future both of you realize that this is a big accomplishment for me. I was in highschool too and in highschool I was bottom of my class. In fact, I did so badly my sophomore year I was already enrolled into an adult school to make up for the bad 10th grade year. My mom, your grandma, was not having it. Grandma is a fighter and she never gave up on me when I was in high school. She moved me to a whole new school, basically any school that will take me and have me as a junior and not a continuation student. I ended up attending a high school in Artesia and it was there where I fell

in love with being a student. I did sports and I caught a grip of school. So going to UCLA and earning a PhD was a dream I never thought I could accomplish. So my message to you both is to always remember that your mother and I will always love you and we will never give up on you both the same way grandma never gave up on me.

TABLE OF CONTENTS

Abstract of Dissertation…..……..ii

Committee Page……..iv

Dedication Page…….……..v

Acknowledgments……..……ix

Vita..……...…xii

Chapter 1: An introduction to aging research…...……...……..…….1

1.1 Hallmarks of Cellular Aging and Senescence……..……..……..…….....2

1.2 Survey of stress induced cellular senescence response……..……4

Chapter 2: A literature review into cellular senescence in macrophages…….……..……15

2.1 Overview of existing research……...16

2.2 Identification of gaps in literature……18

2.3 Central Hypothesis……..…….18

Chapter 3: Approach……..……20

3.1 Aim 1: Identify the molecular drivers of macrophage senescence *in vitro*……..……21

3.2 Aim 2: Determine the physiological relevance of senescent macrophages *in vivo*.…23

Chapter 4: Materials and methods……...……..25

4.1 Mice and mouse derived macrophage culture……..26

4.2 Reverse transcription-quantitative PCR and primers……...….28

4.3 Multi-omic analysis…….……30

4.4 Immunofluorescence and tissue staining……..…35

4.5 Western blot analysis and antibodies……...…36

4.6 Shotgun lipidomics…….….37

4.7 *In vivo* experiments……..37

4.8 Human macrophage culture…….38

4.9 Synthetic guide RNA design and CRISPR……..……39

4.10 Statistics…….……40

Chapter 5: Results……..……42

5.1 Exogenous DNA damage drives *Cdkn1a* (p21)+ senescence in macrophages ……..41

5.2 Senescent macrophages upregulate SASP and sterile type 1 interferon signaling…..51

5.3 p21+ senescent macrophages accumulate in the aged liver…….59

5.4 Senescent macrophages form lipid droplets and express TREM2…….……..……66

5.5 Excess Ac-LDL drives of macrophage senescence *in vitro*……..……72

5.6 ABT-263 efficiently and selectively targets senescent macrophages for apoptosis.…77

5.7 ABT-263 targets a senescent macrophage signature in MASLD…….……82

5.8 Human Scar-associated macrophages express a unique senescent signature……..89

Chapter 6: Discussion and conclusions……..95

Chapter 7: Future directions: From biomarker to bedside…….99

7.1 Limitations: Distinct state may not mean novel driver in MASH…….100

7.2 The double-edged nature of senescence is underplayed..……102

7.3 Broader implications: The missing steps to move into the clinic……..103

Bibliography……...…..104

Acknowledgments:

To my old knowledge, the idea of earning an advanced degree in biology was reserved for the incredibly gifted and those capable of great scholarship. Little did I believe that years later I would be standing in front of the mirror telling myself, you are incredibly gifted and beyond capable of great scholarship. I am days away from defending my thesis alongside a great mentor, Anthony J. Covarrubias, and I am proud to say I earned my place in academic science. With my advanced degree from UCLA, I believe I can become the leader I have always dreamed of becoming and help solve the future's biggest biomedical challenges to ensure health for all. With this, I would like to acknowledge my thesis advisor, Anthony J. Covarrubias, my committee, the MBIDP graduate program, and the members of the Covarrubias Lab.

To Dr. Covarrubias, I would like to thank you for all the support you have provided me since the beginning of my graduate training. Imposter syndrome runs at full strength during the first year of graduate school, but being in your lab and learning more about what you have gone through to be in the position you are in motivates me to continue and reminds me that people from underserved communities in Los Angeles can be leader figures in science and education. Having you as a mentor reminds me that anything is possible as long as we work exceptionally hard individually and, more importantly, as a team. Thank you for being the leader I needed throughout my graduate education. There were plenty of moments where I let science get the best of me, and in the moments where I needed a mentor to push me through hard times, you were there with clarity and a vision for a more successful future.

To my committee and the MBIDP graduate program, I acknowledge that your support was exactly what I needed to reach this level of graduate education. To Dr. Elizabeth Tarling, Dr. Ajit Divakaruni, Dr. Steven Bensinger, and Dr. Alex Hoffmann, thank you for being there for all my questions related to lipids, metabolism, and the inflammatory response. There was never a moment where I felt neglected or undermined throughout my training. In fact, it was quite the opposite. Seeing you all in the audience during many of my talks and seminars grounds me and moves me to give my best performances. I would also like to acknowledge Dr. Hillary Coller for meeting me years before joining UCLA's graduate program and believing that I was a top applicant who could succeed in the program. I was a master's student when you visited CSULA, but I wasn't sure how to network. Therefore, when we met again during UCLA's mitochondria symposium, I stepped outside my comfort zone and made it a goal to introduce myself. That conversation led to my acceptance to UCLA and now to graduation. Thank you, and I acknowledge your support.

To Grasiela Torres, I remind you every now but I don't think words can fully capture how important you have been to my graduate journey. We joined the lab together, and in many ways, we grew through this program side by side. From navigating some of the toughest classes (gene reg) to experiencing the pressure that comes with trying to succeed at this level, you were always there. We have been through all of the unexpected challenges that graduate school seems to bring. Through every high and every low, you remained a meaningful part of the experience. Graduate school felt incredibly isolating at times and there were many moments where the workload felt impossible, experiments failed, and the pressure of expectations became overwhelming. During those moments, having someone who truly understood what I was

experiencing made all the difference. Without you, I genuinely do not know if I would be graduating today. That may sound dramatic, but it is the truth. Your support, encouragement, honesty, and friendship helped carry me through some of the hardest moments of my academic journey. But more importantly, beyond being an incredible lab partner, you became one of my closest friends. You made this graduate program feel less lonely. You brought humor into difficult moments and perspective when things felt overwhelming. Some of my favorite memories from graduate school include the lab outings, the coffee breaks, and the occasional crying lol. You understood the challenges that people like us go through in a way that very few people could, and that made your presence made all the difference for me. I entered graduate school hoping to earn a degree and become a better scientist. What I did not expect was to leave with a friendship that I know will last far beyond the walls of this institution. Thank you for being an incredible scientist, an amazing lab partner, and, most importantly, a true friend. Your impact on my life and graduate journey is permanent, and I will always be grateful that we experienced this chapter together.

To the undergraduate students: Elizabeth Guli, Albert Macias, Daniella Choi, Ronak Hegde, Dhruv Suresh, Cristian Ponce, and Eduardo Enriquez, and lets not forget my amazing colleagues: Anika Dhingra, Lizeth Estrada, Itzetl Avila, Christina Deng, and Utkarsh. Thank you for making this lab such a meaningful place to grow. I truly appreciated every moment we shared, from long experimental days and scientific discussions to the laughter and friendships that made even the hardest days feel lighter. Each of you contributed something special to this environment, and because of that, this lab became more than just a workplace… It's still a workplace but I would not trade my time in this lab, or the people I shared it with, for anything else

Vita

Education

- ❖ M.S. California State University, Los Angeles
- ❖ B.S. California State University, Long Beach
- ❖ A.S. Long Beach City College, Long Beach

Publications

1. **Salladay-Perez, Ivan A**., Itzetl Avila, Lizeth Estrada, et al. 2026. “p21+TREM2 Senescent Macrophages Fuel Inflammaging and Metabolic Dysfunction-Associated Steatotic Liver Disease.” Nature Aging 6 (4): 792–815.
2. **Salladay-Perez, Ivan A**., and Anthony J. Covarrubias. 2026. “Cholesterol-Induced Senescent Macrophages and Evaluation of Cellular Senescence Phenotypes.” Current Protocols 6 (4): e70355.
3. Torres, Grasiela, Utkarsh Tripathi, **Ivan Salladay-Perez**, Itzetl Avila, and Anthony J. Covarrubias. 2026. “An In Vitro Model of Macrophage Senescence.” Current Protocols 6 (4): e70230.
4. Jiang, Yuming, **Ivan Salladay-Perez**, Amanda Momenzadeh, et al. 2026. “Single-Injection Multi-Omics Analysis by Direct Infusion Mass Spectrometry.” Angewandte Chemie (International Ed. in English), March 30, e19836.
5. Torres, Grasiela, **Ivan A. Salladay-Perez**, Anika Dhingra, and Anthony J. Covarrubias. 2024. “Genetic Origins, Regulators, and Biomarkers of Cellular Senescence.” Trends in Genetics : TIG 40 (12): 1018–1031.

Honors and awards

1. Travel Award Geroscience symposium, Nathan shock center for aging research, Oklahoma, USA.
2. Phillip Whitcome, Ph.D. Pre-Doctoral Fellowship.
3. The Suzanne Eaton, Ph.D. Memorial Prize

4. Poster award 2nd Annual Gerontology Los Angeles Meeting (GLAM), University of Southern California.
5. Graduate student oral presentation award, 1st Annual Gerontology Los Angeles Meeting (GLAM), University of Southern California.
6. NIH T32 Cell and Molecular Biology pre-doctoral training program, University of California, Los Angeles.
7. Cota Robles Fellowship, University of California, Los Angeles.

Chapter 1:

An introduction to aging research

1.1 Hallmarks of Cellular Aging and Senescence

Aging is a multifactorial process that, beyond reproductive maturity, becomes increasingly maladaptive, driving progressive physiological decline, heightened susceptibility to various aging-related diseases and systemic chronic inflammation, known as inflammaging (Franceschi & Campisi, 2014). Over the last two decades a collection of hallmarks have been established to the aging process across mammalian systems(López-Otín et al., 2023). Cellular senescence has emerged as an antagonistic aging process that serves as the major source of tissue inflammaging, fueling intense interest in senescence-targeted therapies(Chaib et al., 2022). Indeed, preclinical studies demonstrate that eliminating senescent cells can improve both healthspan and lifespan(Camell et al., 2021). However, a major barrier to this approach is the limited understanding of which cell types undergo senescence during aging and the lack of specific biomarkers to distinguish senescent cells from other proinflammatory populations.

This introduction comprehensively examines the molecular biology of cellular senescence with a particular focus on various cellular stressors and pathways leading to senescence; including recent advancements in the understanding the cellular influences driving cellular senescence, such as telomere attrition, chemotherapy-induced DNA damage, pathogens, oncogene activation, and cellular and metabolic stress. This introduction also highlights the complex interplay of various signaling and metabolic pathways involved in cellular senescence and provides insights into potential therapeutic targets for aging-related diseases. Furthermore, it outlines future research directions to deepen our understanding of senescence biology and develop effective interventions targeting senescent cells.

Senescent cells contribute to aging and aging-related diseases, prompting research into targeted therapies. Senescent cells are damaged cells that have undergone irreversible cell cycle arrest and secrete inflammatory cytokines and other factors, known as the senescence-associated secretory phenotype (SASP) (Coppé et al., 2008). Cellular senescence acts as an anti-tumor program that prevents damaged cells from further proliferation , regulates development (Muñoz-Espín et al., 2013), and can also promote wound healing (Demaria et al., 2014). However, during aging, DNA damage and other cellular stressors lead to an excess burden of senescent cells, which are emerging as a key source of inflammation in aged tissues (Figure 1) (Zhou et al., 2026).

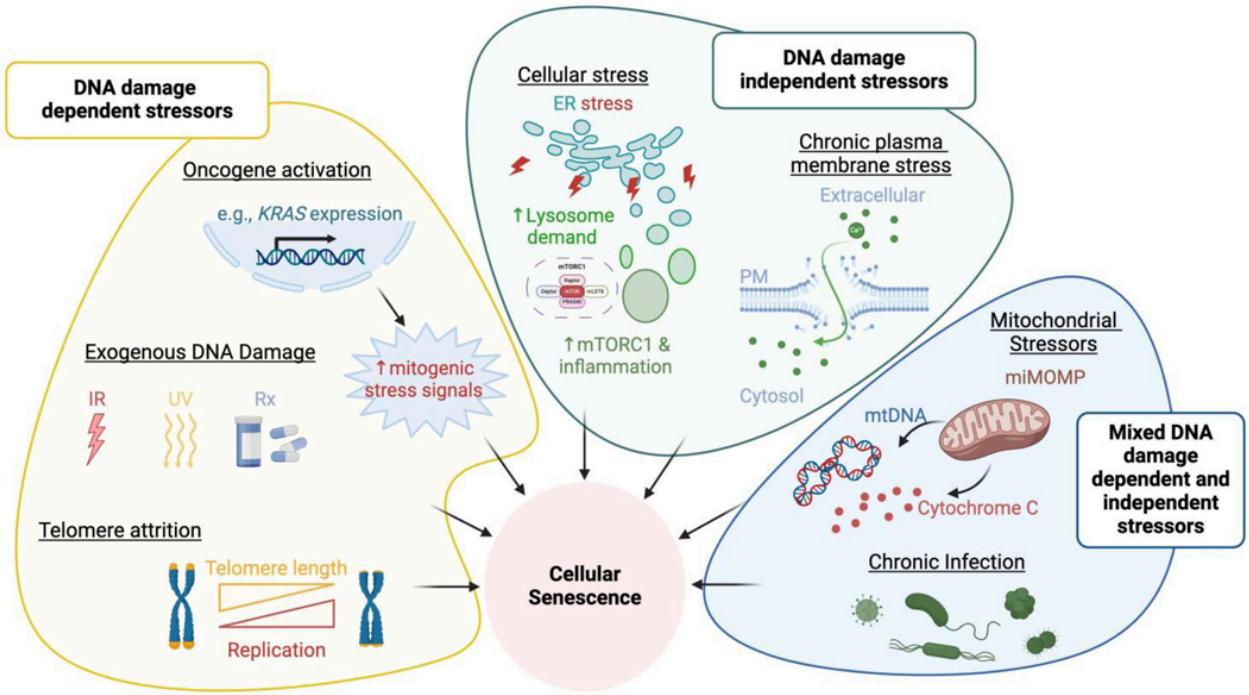


Figure 1. SnCs are damaged or stressed cells that contribute to aging and various aging-related diseases. Multiple mechanisms contribute to the burden of SnCs in tissues, some of which include DNA damage-independent mechanisms. Direct DNA damage or genomic instability are

mechanisms originally discovered to drive a cellular senescence phenotype. These mechanisms include replication-induced telomere attrition, exogenous DNA damage with Irradiation (IR), (UV), and alkylating drugs (Rx) like chemotherapies [yellow bubble]. However, new and emerging mechanisms have revealed cellular stress mechanisms that are DNA damage independent and involve the ER, lysosome, and plasma membrane (PM) stress [green bubble]. Interestingly, senescence can be driven by mitochondrial dysfunction or chronic exposure to infections which have shown mixed mechanisms impacting both DNA integrity and cellular health [blue bubble]. With a growing collection of mechanisms contributing to cellular senescence, it is still unclear what are the leading mechanisms that contribute to the origins of senescent cell burden during human aging.

1.2 Survey of stress induced cellular senescence response

Senescent cells can promote tissue damage, tissue dysfunction, and, paradoxically, cancer itself (Tarumi et al., 2026). Thus, there is a growing interest in the aging field to determine the biology driving cellular senescence, how these cells contribute to the aging process, and methods to selectively target senescent cells to treat aging-related diseases (Gasek et al., 2021). Recent breakthroughs in this area have focused on the development of senolytic drugs, a class of pharmaceuticals designed to selectively target and destroy senescent cells, as well as senomorphs that suppress the SASP. Despite these promising advances, most senolytic drugs are still in the preclinical stages of drug discovery and none have been approved for use in the clinic for therapeutic use. In this review, we aim to shed light on the latest advancements in the last 5 years that have enhanced our understanding of cellular senescence. This includes the genetic influences that are important for driving and regulating senescent cell phenotypes, such as 1) telomere attrition, 2) oncogene activation, 3) exogenous and endogenous sources of DNA damage, 4)

cellular and metabolic stress, and 5) epigenetic influences. Collectively, this information will be helpful in the current understanding of the genetic origins of cellular senescence and provide significant insight into human health and life span.

Telomere attrition – Cellular senescence was first observed in fibroblasts in 1961 and described by Hayflick and Moorhead as a cell cycle arrest in response to serial passaging (Rossiello et al., 2022; Silwal et al., 2023). Telomeres, stable GC-rich regions at the ends of chromatids, consist of repeated 'TTAGGG' sequences. In 1990, Harley, Futcher, and Greider demonstrated that these sequences shorten with each cell division (López-Otín et al., 2023). This gradual loss in telomere length is now an established hallmark of aging (El Maï et al., 2020). As telomeres shrink, they fail to provide sufficient space for DNA replication fork disassembly, leading to genomic instability—a key driver of DNA damage-induced senescence with aging. Recent advancements shed light on how proteins like p53 and p16INK4a modulate cellular fate post-telomere damage. In zebrafish models lacking telomerase (Tert−/−), shortened telomeres trigger apoptotic cell death through p53 in young specimens, whereas in aged counterparts, p53 activity wanes, replaced by enhanced mTORC1/AKT activity, which drives reactive oxygen species (ROS) production and mitochondrial dysfunction leading to a p16-dependent senescence phenotype (Azarm et al., 2020). Telomere shortening can also disrupt the binding of protective proteins and telomere-repeat binding proteins 1 and 2 (TRF1/2), which cap telomere ends, preventing damage and activating a p53-dependent senescence response (Lanna et al., 2022). Additionally, recent research reveals a nuanced role of TRF1/2 levels in this process. Loss of TRF1 exhibits a protective effect against p53-induced senescence in various cell types experiencing telomere shortening. Furthermore, investigations into how rapidly dividing T cells evade telomere shortening-induced senescence unveiled a novel mechanism involving the

horizontal transfer of telomeres from antigen-presenting cells (APCs) (Muñoz-Lorente et al., 2019). Upon immunological synapse, physical contact between APCs and T cells, APCs cleave their own telomeres and share them with activated T cells to protect these rapidly dividing cells from replicative senescence. Interestingly, mice models overexpressing Tert or with hyper-long telomeres have also been shown to be protected from aging phenotypes. Conversely, Tert−/−mice have accelerated aging phenotypes (Karimian et al., 2024). However, telomeric DNA damage and senescence can occur regardless of telomere length, and whether longer telomere length is protective in humans remains uncertain. However, new tools being developed with greater precision to measure telomere length at the single nucleotide level will be helpful in answering these questions (Liu et al., 2018). These studies underscore the need for a deeper understanding of the diverse cell-specific mechanisms that both promote and protect against telomere attrition and replicative senescence.

Oncogene activation – In response to mutagenic oncogenic activation, proliferative cells may undergo cell-cycle arrest to suppress tumor progression, termed oncogene-induced senescence (OIS). Activated oncogenes primarily include those in the Ras/Raf/MAPK pathway, such as H-RASG12V and B-RAFV600E, and drive DNA damage through hyper-replicative stress. OIS can also be activated through oncogenic activation of the PI3K/AKT pathway(Moiseeva et al., 2009). The oncogenic stress response converges with the activation of the p53-p21 axis as well as p16-Rb stability to prevent cell-cycle progression. Alongside DNA damage, OIS induces mitochondrial dysfunction, leading to the accumulation of mitochondrial DNA (mtDNA) and ROS (Martínez-Zamudio et al., 2023). While OIS is ostensibly an anti-cancer mechanism, recent efforts have focused on investigating the paradoxical pro-tumorigenic capacity of oncogene-induced senescence. Oncogene activation in senescence

cells can promote cancer growth via numerous mechanisms, including via heightened pro-inflammatory SASP expression, proliferative reversion, or oncogene-induced escape from senescence, and by helping the cell evade the senescence program (bypass). In a zebrafish model, a gain of function mutation in TP53 drives primary tumorigenesis by secreting the SASP and influencing neighboring cells to become senescent-like (termed secondary senescence) and similarly contributing to the SASP, amplifying the pro-tumorigenic capacity of senescence (Igelmann et al., 2021). Metabolic, epigenetic, transcriptional, and post-transcriptional regulation (Martínez-Zamudio et al., 2023; Zampetidis et al., 2021) may explain senescence bypass and/or escape in response to oncogenic activation. For example, p53 can suppress the hydride transfer complex (HTC) that converts NADH to NADPH; with the loss of functional p53, the HTC is active, and the accumulation of NADPH protects against ROS, leading to senescence bypass (Zampetidis et al., 2021). Another recent study using human cells also showed that Chromosome 3 inversion at the BHLHE40 locus allows for a bypass of CDC6-induced OIS and promotes aggressive tumor development . Moreover, senescence-associated chromatin scars were identified as an epigenetic memory that can identify post-senescent cells that escaped from OIS (Villot et al., 2021; D. Wu et al., 2022). There is emerging evidence that this senescence-associated epigenetic landscape may define the threshold between OIS and tumor progression, including via the regulation of transcription factors such as POU2F2, ZNF768, and MZF1 (Zhang et al., 2020). Post-transcriptional control through miRNA regulation can also influence OIS phenotypes, such as miR-192/215 in human gastric carcinoma cells, and mRNA stabilization through differential expression of mRNA binding proteins such as UNR/CSDE1 in primary mouse keratinocytes and HuR in melanocyte OIS (Avolio et al., 2022; Liebig et al., 2020). In summary, numerous intricate mechanisms control how cells respond to oncogene activation. Thus, there is a need for a greater

understanding of how these molecular mechanisms converge to determine what cells undergo OIS, and those that evade or bypass OIS. This future insight will be key to help advance the discovery of anti-cancer and senolytic therapeutics.

Exogenous DNA damage – Environmental sources of DNA damage are contributors to senescent cell accumulation with age and are a standard method to induce senescence in cell culture (Peng et al., 2020). Exogenous stressors like ultraviolet (UV), ionizing radiation, and alkylating agents used to treat proliferative disorders like cancer are known to cause senescence in a range of cell types via DNA damage (Sriratanasak et al., 2022; Zhao et al., 2020). Due to the global and non-specific effects of most cancer chemotherapies, it is essential to know whether there are any tissue-specific effects on proliferative cells and whether these effects exacerbate tumor lethality or sensitize tumor cells to immune clearance. So far, new research investigating drug therapies in the brain, lungs, kidneys, and ovaries discovered cisplatin to activate p53-mediated senescence (Acklin et al., 2020; S. Li et al., 2023; Paffenholz et al., 2022). Cisplatin is platinum-based chemotherapy that targets DNA annealing via purine residues of DNA (C. Li et al., 2019). Researchers have found long-term cisplatin exposure in the lungs and kidneys to drive mitochondrial-derived ROS-induced DNA damage to stabilize p53 acetylation and maintain *Cdkn1a* (p21WAF/CIP1) expression and senescence (Yousefzadeh et al., 2021). This DNA damage-induced senescence has been shown to mediate sensitivity and resistance to first-line chemotherapy in a mouse model of high-grade serous cervical cancer in a p53-dependent manner. In aging, however, a heterogeneous population of cells will react differently to the same genomic stress insult based on their unique characteristics, such as genetics, functions, and location in the body. Interestingly, accelerated aging in the immune system can be caused by exogenous and even endogenous forms of DNA damage and is a major

contributor to sterile inflammation. In mouse models where immune cells lack the ability to repair DNA, mice experience greater tissue senescence and accelerated inflammation and aging (Ziegler et al., 2021). Together, these studies highlight how cells respond to exogenous DNA damage-inducing agents and the critical role of p53-dependent mechanisms that maintain senescence after drug therapies, as well as emphasize the importance of which cell types are being exposed to DNA damage factors and contribute to the aging process.

Cellular stress – Endoplasmic reticulum (ER), lysosomal, and plasma membrane (PM) stresses have emerged as key drivers of senescence, both in DNA damage-dependent and independent manners. While persistent protein misfolding and lysosomal deregulation originating from the ER are well-recognized phenotypes in senescence, the role of ER stress as a direct driver of senescence, rather than merely an effector, remains largely understudied. Recent research has shed light on this aspect, revealing that inter-organelle contacts, such as mitochondrial-ER contacts (MERCs), induce premature senescence through a p53-dependent, ROS-dependent mechanism in human fibroblasts (McHugh et al., 2023). Of particular interest is the interaction between the ER and the Golgi apparatus mediated by the coatomer complex I signaling pathway, which has emerged as a target for selectively eliminating senescent human fibroblasts in both culture and mouse models of cancer and steatohepatitis (Anerillas et al., 2023). Furthermore, a whole-genome knockout screen has identified the YAP–TEAD (Yes-associated protein–TEA domain family member) protein complex as a critical regulator of cellular senescence and the SASP through ER biogenesis. The interaction of YAP with TEAD enhances ER biogenesis during cellular senescence, fueling this process through the mTORC1 pathway(Roh et al., 2023). Additionally, SASP lysosomes export SASP factors originating from the ER. Excess cholesterol loading and increased synthesis of cholesterol esters modulate the

activity of ABCA1, a lysosomal ATP-binding cassette transporter, at the lysosomes, thereby controlling mTORC1 activity and SASP (Suda et al., 2024) Lastly, cellular stress mechanisms through PM damage can induce senescence in a DNA damage-independent manner. Recent studies have shown that prolonged PM stress accelerates aging phenotypes in yeast via a p53, p21, and p16-dependent pathway, reducing replicative lifespan and similarly inducing senescence in human fibroblasts (Gulen et al., 2023). Collectively, this data underscores the critical importance of cellular stress on essential cell functions, including those of the ER, lysosome, and PM, in both preventing and driving senescence, with potential implications for organismal aging.

Mitochondrial function – Mitochondrial Dysfunction (MiD) contributes to cellular senescence through various mechanisms, some of which may be independent of direct DNA damage. While mitochondria play pivotal roles in maintaining cellular bioenergetics and signaling homeostasis, these regulatory functions become compromised with age and in SnCs. Recent studies shed light on the long-term repercussions of mitochondrial stress in senescence, revealing its involvement in inducing DNA damage and inflammation through Mitochondrial Outer-Membrane Permeabilization (MOMP). Under inflammatory conditions, mtDNA released into the cytosol triggers a cytosolic DNA-sensing inflammatory mechanism known as the cGAS-STING pathway. Emerging evidence, including studies using tamoxifen-induced cGAS expression in murine microglia, suggests that selective activation of the cGAS-STING pathway may drive chronic low-grade inflammation with age and cellular senescence (Correia-Melo et al., 2016). However, the precise mechanism driving cellular senescence remains unclear. Notably, apoptotic stress can lead to sublethal level of MOMP in a minority fraction of mitochondria (miMOMP) in SnCs, disrupting electron transport chain functions, causing electron leakage, and generating superoxide radicals, including ROS, along with double-stranded DNA breaks (Riley

et al., 2018; Victorelli et al., 2023). It's increasingly apparent that miMOMP contributes to apoptotic resistance in SnCs via the BAX/BAK macropore formation and triggers the SASP and organismal inflammation through mtDNA release . Mitochondria are also thought to contribute to the SASP and senescence independent of DNA damage termed as MiD associated with senescence (MiDAS). MiDas is caused by reduced cellular NAD+/NADH ratios involving AMPK signaling to maintain SASP and other hallmarks in senescence. This mechanism is thought to be governed by deacetylase proteins such as mitochondrial SIRT3 and p53. Collectively, accumulating evidence suggests mitochondria can integrate multiple senescence signaling pathways that control various senescent phenotypes, such as anti-apoptotic mechanisms, metabolic reprogramming, and inflammatory signaling. Further research into the role of mitochondria as a central hub of senescence cell biology is essential for a deeper understanding of how this organelle helps facilitate the senescent cell fate and will help guide how the mitochondria can be targeted for therapeutic purposes.

Epigenetic remodeling – Cellular senescence is driven and maintained by a variety of epigenetic mechanisms that actively repress cell-cycle regulatory factors and promote pro-inflammatory signaling molecules and cytokines (Benayoun et al., 2019; Olan et al., 2020). DNA and histone methylation, as well as senescence-associated heterochromatin foci (SAHF), have been found to increase with age and in SnCs, serving as molecular mechanisms how SnCs maintain cell-cycle arrest and serve as a universal predictor of aged phenotypes across mammals (Lu et al., 2023); New evidence demonstrates the loss of epigenetic control of genome-wide activity may serve as a driver of cellular senescence and its effector programs like inflammation (J.-H. Yang et al., 2024). New research has highlighted novel epigenetic mechanisms by which SnCs maintain the SASP as well as reverse its proinflammatory phenotype. In a recent study,

authors used HI-C technologies in RAS-induced senescence in human diploid fibroblasts and discovered extensive enhancer-promoter rewiring at cytokine (e.g. II1β) loci. This repositioning of genome-wide topology was similar to inflammatory macrophage remodeling and distinct from other cell-cycle arrested phenotypes, such as cellular quiescence (Figure 2) (Sen et al., 2023). New research also used precision run-on mapping techniques to understand the fidelity of gene transcription mechanisms in human senescent fibroblasts. It was found that SnCs modulate global transcription activity as a DNA damage response (DDR) that is thought to be the main genetic mechanism contributing to "noisy" transcriptional activation (Rübe et al., 2021). At the nucleosome level, novel mechanisms of H2A.J have been identified to regulate the SASP in models of human fibroblast senescence. H2A.J is a mammalian-specific and widely understudied histone variant that has been observed to accumulate in human-aged skin and in mouse models of ionizing radiation dermatitis (Contrepois et al., 2017; Tewary et al., 2024). H2A.J accumulation has also been shown to accumulate in a variety of human fibroblast senescence models of persistent DNA damage and has also been shown to contribute to the SASP. More recently, the molecular mechanisms of how the H2A.J variant contributes to senescence have been elucidated. Two groups have recently observed that a loss of the H2A.J variant attenuates the interferon and antiviral response in human fibroblasts by reducing STAT and interferon transcription factor binding, which is possibly driven by the loss of H1 linkers attached to histones (Contrepois et al., 2017). Given the importance of the epigenetic landscape of histone abundance and transcription factor activity related to inflammation, another recent study has shown that aging, and potentially senescence, may be driven by the loss of an "epigenetic identity" and many of the pro-senescence cell fate and pro-aging mechanisms can be reversed by Yamanaka factors. Together, these findings demonstrate the importance of the loss of epigenetic identity as a driver

of cellular senescence, and understanding the genetic and molecular mechanisms of epigenetics can reveal new and novel modalities to reverse the pro-inflammatory effects of senescent cell accumulation with age.

Genome-wide association studies in senescence – Somatic mutations accumulate in multiple cells and tissues throughout aging. Whether senescent cells accumulate mutations that contribute to cellular senescence development is little known. In the late 2000s, significant genome-wide association studies (GWAS) studies identified the *CDKN1A/B* locus on chromosome 9p21 to be highly associated with a variety of cardiac diseases such as myocardial infarction, coronary artery disease, and stroke (Contrepois et al., 2017; Hannou et al., 2015; Jiang et al., 2022). The CDKN2A/B is 200 kb in size and encodes for four tumor suppressor genes (ANRIL, p14ARF, p15INK4b, p16INK4a, and follow-up studies identified the perturbed expression of senescent biomarker p16INK4a across a variety of age-related diseases (T. Wu et al., 2023). Recent post-GWAS functional studies have advanced the understanding of what regulates p16INK4a in senescence. A study has recently demonstrated that Cut-Like Homeobox 1 (CUX1) protein physically binds to the *CDKN1A/B* loci at an atherosclerosis-associated position to control for the expression of p16INK4a in human endothelial senescence (López-Domínguez et al., 2021). This research group further characterized the role of a p16INK4a transcriptional repressor known as SATB2, an AT-rich binding protein that competes with CUX1 to control p16INK4a expression in senescence (West et al., 2023). In parallel with p16, *CDKN1A* (p21) transcriptional variant 2 has emerged as a major biomarker for aging and cellular senescence; however, the complete role of p21 is not fully understood in cellular senescence (Martin et al., 1970; West et al., 2023). GWAS has revealed several genetic candidates that serve as major cellular senescence regulators or as novel biomarkers of the

cellular phenotype. Interestingly, a new integrative analysis of multiple GWAS has identified that most low-signal variants in cellular senescence are also associated with multiple diseases (Dimri et al., 1995). The underlying features of metabolic and age-related diseases include cellular senescence and highlight the importance of identifying alternative markers and regulators of cellular senescence through GWAS.

Chapter 2:

A literature review into cellular senescence in macrophages

2.1 Overview of existing research

Macrophages are highly versatile innate immune cells that adopt diverse polarization states in response to their microenvironment. Notably, they share multiple hallmark features of senescent cells, including inflammatory cytokine secretion, metabolic reprogramming, immunomodulatory metabolite production, increased cell size and transient expression of senescence-associated markers such as *Cdkn1a* (p21), *Cdkn2a* (p16), senescence-associated secretory phenotype (SASP) factors and senescence-associated β-galactosidase (SA-β-gal) activity. (Hall et al., 2017).

The association between cellular senescence and cellular aging is based on various in vitro studies dating back to the 1970s, where researchers made several observations, including a higher incidence of senescence in cells cultured from old donors or patients with progeroid syndromes (Martin et al., 1970). Cellular senescence is widely accepted as a hallmark antagonistic hallmark of aging and the same mechanisms that drive aging are also hallmarks of what causes cellular senescence (e.g. telomere shortening and DNA damage). Clearance of senescent cells have been shown to extend lifespan and improve health in mouse progeroid and age-related diseases mouse models . This suggests cellular senescence not only serves as identification of senescent biomarkers *in vivo* and *in vitro* has therefore become a major effort in the field of aging, one that even has therapeutic potential as these markers can be exploited for the generation of senolytics. Senescent-associated beta-galactosidase activity (SA-β-gal), which takes advantage of lysosomal β-gal expression at a pH of 6.0, has been extensively used to identify SnCs in vitro and *in vivo (Dimri et al., 1995)*. However, not all SnCs display SA-β-gal activity, creating a limitation for the application of this biomarker.

Adding to this limitation is the identification of SA-β-gal positive non-SnCs throughout embryonic development, along with the demonstration of cell culture conditions like cell density affecting SA-β-gal staining, suggesting that SA-β-gal is not a specific maker for cellular senescence (de Mera-Rodríguez et al., 2021). Additionally, DNA methylation has been widely used to assess the aging phenotypes displayed by senescent cells; However, SA-β-gal positive fibroblasts epigenetic clocks that assess DNA methylation do not predict senescence suggesting one test to determine senescence is unreliable and may be independent from the mechanisms driving aging . Increased cell cycle expression-regulating genes p21 and p16 have also been regarded as hallmarks of senescence and are most commonly used when determining whether a cell is senescent. Like SA-β-gal, p16 expression should not solely be used for characterizing cellular senescence, as its expression is not specific to SnCs (Hall et al., 2017). Therefore, the lack of selectivity for SA-β-gal and p16 expressions must be considered to avoid excluding true SnCs or even producing false-positive identification of non-SnCs.

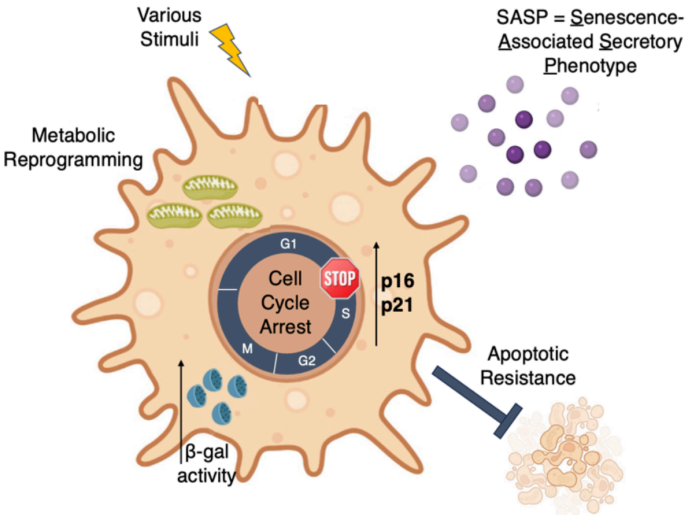


Figure 2. Senescent cells and their similarities to activated macrophages. Cellular senescence is a cell fate in response to various genotoxic and metabolic stress. To avoid the formation of

cancerous cells in tissues cells signal to the body via signaling through the SASP. Senescent cells appear as activated macrophages. Macrophages when triggered by an activating signal will communicate to the body via inflammatory signals and modulate the expression of certain proteins such as the upregulation of p16, p21, metabolic reprogramming, and resistance to cell-death signals.

2.2 Identification of gaps in literature

The phenotypic overlap raises a fundamental unresolved question: can macrophages undergo bona fide cellular senescence, and if so, how can senescent macrophages be distinguished from activated proinflammatory (M1) or anti-inflammatory (M2) states? Although accumulating evidence links macrophage senescence to age-related inflammation and disease, many studies rely on limited, reversible and context-dependent markers, thereby complicating interpretation(Haston et al., 2023; Rabhi et al., 2022; Sadhu et al., 2021; Su et al., 2021; H. Wang et al., 2020). As a result, defining macrophage senescence remains a formidable challenge and a major unmet need in the field. Unlike other immune cells, tissue-resident macrophages are radioresistant, metabolically flexible and often long-lived, particularly in their tissue niche(Covarrubias et al., 2016; Hashimoto et al., 2013). These features enable survival in highly stressful microenvironments but may also predispose macrophages to withstand cumulative DNA damage and metabolic stress, rendering them susceptible to senescence with age. Here we test the hypothesis that macrophages represent a major source of senescent cells in aging tissues and act as key drivers of inflammaging.

2.3 Central Hypothesis

Senescent cells have recently been shown to accumulate in both the liver and adipose tissue under conditions of obesity, and have been linked to the development of insulin resistance,

non-alcoholic fatty liver, and hepatic steatosis. However, it is uncertain whether cellular senescence is only associated or is a casual driver of age-related metabolic dysfunction, and the progression of the disease to metabolic dysfunction associated fatty-liver disease (MASLD), liver fibrosis, and ultimately hepatocellular carcinoma. Moreover, a key limitation and unresolved question in the inflammaging field is identifying the cells that become senescent in aging and metabolic diseases. This is due to the fact that detecting senescent cells *in vivo* is very difficult due to limited techniques and biomarkers to identify them at the single cell level. Interestingly, our lab's preliminary data suggest macrophages can undergo senescence and represent a key source of senescent cells *in vivo*. To further investigate the biology of senescent macrophages our lab has developed a novel in vitro senescent macrophage model system, which we have used to identify novel biomarkers associated with macrophage senescence. Using these senescent macrophage biomarkers, our lab has shown via bulk and single-cell RNA sequencing analysis of aged metabolic tissues and other traditional approaches such as immunofluorescent staining that senescent macrophages, and not other cell types, accumulate in the liver and adipose tissue of aging tissues and during the setting of MASH induced fibrosis.

Therefore, we hypothesize that macrophages are a significant source of senescent cells in metabolic tissues, contributing to aging-related metabolic diseases such as metabolic dysfunction associated with fatty liver disease (MASLD) and playing a pivotal role in the progression of MASH cirrhosis.

Chapter 3:

Approach

3.1 Aim 1: Identify the molecular drivers of macrophage senescence *in vitro*

Based on the literature around cellular senescence and lipid stress we hypothesized excess lipid storage, such that occurs during age-related metabolic disease like MASLD, is a key driver of macrophage senescence and that excess senescent cell burden helps drive MASH, tissue fibrosis, and inflammation in the setting of MASLD and aging. To understand this, we will test this hypothesis in multiple complementary ways including 1) Treating BMDMs and human PBMC derived macrophages with acetylated forms of LDL and investigating senescent features. As described in previous publications, we will treat primary human and mice macrophages with both Ac-LDL, and test whether this treatment promotes cellular senescence using various methods such as SASP measurement, SA-β-Gal assay, and cell cycle arrest. Additionally. We will determine the genetic determinants which contribute to macrophage senescence utilizing mice from the Hybrid Mouse Diversity Panel (HMDP). We will grow primary BMDM macrophages from the varying strains of mice and make them senescent via irradiation or treatment with lipids, then assess if cell intrinsic properties like genetic loci will drive cellular senescence. We will then measure gene expression in control and senescent macrophages via bulk RNA sequencing, as well as measure other features of senescence discussed above to determine the genetic determinants of macrophage senescence and specific gene loci that influence macrophage senescence. Lastly, we will treat control mice and mice fed a pro-MASH Western diet and quantifying macrophage senescence utilizing our novel senescent macrophage transcriptomic score and using validated biomarkers to isolate the via flow cytometry/Immunofluorescence. We will perform *in vivo* studies using a standard MASH fibrosis model, which has been validated by our collaborators in the Lusis Lab. This model relies on feeding mice a Western diet high in fat and cholesterol (HFHC) to drive liver steatosis, MASH,

and fibrosis in 12-16 weeks. In our study male and female young (3 months) and old (18+ months) C57BL/6J mice will be placed on the HFHC diet for up to 16 weeks. The livers and adipose tissue of these mice will be analyzed numerous ways including analyzing senescent markers via single cell RNA sequencing and spatial transcriptomics (UCLA Genomics Core), lipidomics (UCLA Lipidomics core, Bensinger Lab), metabolomics to measure tissue metabolites (UCLA Metabolomics Core), serum/tissue proteomics to measure SASP (Schilling Lab, Buck Institute), and traditional methods (immunofluorescence staining, flow cytometry, Western blot, etc). This will allow us to quantitate the number of senescent macrophages present, measure NAD+ and related metabolites, measure tissue and cellular gene expression, and determine the metabolic and molecular pathways activated in both metabolic tissues and cells during MASLD.

Expected Outcomes – In Aim 1, we expect excessive and chronic lipid storage stress to be a major inducer of macrophage senescence both *in vitro* and in the setting of MASLD and aging. While data already suggest senescent genes are enriched in the livers of MASLD mice, the single-cell analysis will allow us to test whether this senescent gene signature is derived from macrophages and/or another cell type found in the liver. Moreover, we expect that in addition to lipid loading and environmental triggers, the genetics background of the cell of origin can also influence macrophage phenotypes as we observe in our preliminary data.

Potential Pitfalls, and Alternative Approaches – A potential concern in this study is whether our in vitro model of macrophage senescence accurately reflects senescence induced in vivo in both aging and MASLD. This is why we propose to validate key features of macrophage senescence utilizing unbiased omic approaches for both our in vitro and in vivo studies and determine key similarities and differences. We also recognize that other cell types besides

macrophages may also exist, and we hope these can be captured using our sing cell sequencing approach. Lastly, MASLD is a complicated disease and various stressors beyond lipid loading may drive senescence in liver cells. Thus, our lab plans to utilize our macrophage senescence system to study other stressors that can promote macrophage senescence such as mitochondrial and ER stress, oncogene induced senescence, and chronic activation of inflammatory signals/pathways.

3.2 Aim 2: Determine the physiological relevance of senescent macrophages *in vivo*

Our preliminary data suggest macrophages represent a key source of senescent cells in metabolic tissues in aging-related metabolic disease and non-alcoholic fatty liver disease and are a key driver of MASH cirrhosis. Therefore, we hypothesize that targeting these cells with senolytics, drugs that selectively kill senescent macrophages, will help prevent or reduce liver fibrosis and tissue injury in mice fed a pro-MASH diet.

Experimental Design – We will test this hypothesis by 1) utilizing our senescent macrophage system as a platform to screen through known senolytics that selectively kill senescent cells both *in vitro* and *in vivo*. Working with Robert Damoiseaux, Director of the UCLA Molecular Screening Shared Resource Core, we have leveraged our senescent macrophage system as a platform to screen known senolytics and drug libraries. Our preliminary analysis has already revealed the senolytic ABT-263 to be a drug that can selectively kill senescent macrophages, which we have used as a positive control molecule to further validate and optimize our senolytic drug screen. 2) We will treat control mice and mice fed a pro-MASH Western diet the senolytic ABT-263 to determine if targeting or deleting senescent macrophages can be used as a potential therapeutic approach to treat aging-related metabolic disease and MASLD: As described in Aim 1, we will perform in vivo studies using a standard MASH

fibrosis model, mice fed a Western diet high in fat and cholesterol (HFHC) to drive senescence, liver steatosis, MASH, and fibrosis in 12-16 weeks. In our study male and female young (3 months) and old (18+ months) C57BL/6J mice will be placed on the HFHC diet for up to 16 weeks. The drug ABT-263 or vehicle will be fed to mice via oral gavage for 7 days each in 2 cycles in week 12 and week 14. We will perform a similar analysis as described in Aim1. Expected Outcomes. In Aim 2, we expect senescent macrophages are a causal driver of MASLD disease pathology and that targeting these cells will reduce inflammation, SASP expression, and liver tissue damage in MASLD and aging.

Potential Pitfalls – and Alternative Approaches: A major concern of the study is the efficacy and selectivity of ABT-263 and other senolytics *in vivo*.

Chapter 4:

Materials and methods

4.1 Mice housing and mouse derived macrophage culture

Ethical compliance for mouse experiments – All mouse experiments and procedures were approved and performed in accordance with the guidelines set forth by the University of California, Los Angeles (UCLA) Animal Resource Committee and the Institutional Animal Care and Use Committees (IACUC). In addition, PBMCs were isolated at UCLA's Virology Core; because these samples do not contain any identifying information, these experiments are IRB-exempt.

Mice – Male C57BL/6J mice 8–12 weeks old (Jackson Laboratory) served as a source of bone marrow for BMDMs. Aged C57BL/6J mice from the Jackson Laboratory and from the National Institute of Aging were used to harvest aged (21–24 months) tissues. WT and *Cd38* KO mice on a C57BL/6J background were obtained from the Jackson Laboratory and were bred and housed at UCLA's animal facility in the Center for Health Sciences. Bone marrow from these mice were used in experiments comparing WT and *Cd38* KO. To eliminate p16-positive cells, p16-3MR mice (provided by the Campisi Lab) were housed at the Buck Institute, and bone marrow was shipped to UCLA for in vitro BMDM experiments with GCV. The breeding and characterization of APOE*Leiden-CETP transgenic mice have been described previously. To generate the F1 mice for the fibrosis studies, homozygous male mice carrying both CETP and *APOE**-Leiden transgenes were maintained on C57BL/6J background and crossed to C57BL/6J, 129/SvJ and BXD19/TyJ mice, respectively. All mice were housed at UCLA's animal facility in the Center for Health Sciences. Unless used for MASLD studies described below, all mice were maintained at UCLA on a standard chow diet.

Mouse macrophage culture – BMDMs used in experiments were derived from bone marrow extracted from the femurs of euthanized mice (6–12 weeks old, male C57BL/6J) by mortar and pestle. Femurs were placed in the mortar and were washed with 70% ethanol to sterilize followed by two washes with complete RPMI (cRPMI; standard RPMI (Corning) supplemented with 10% fetal calf serum, penicillin–streptomycin solution (Corning), 1 mM sodium pyruvate solution (Corning), 2 mM L-glutamine solution (Corning), 10 nM HEPES buffer (Corning) and 50 µM 2-mercaptoethanol). After washing, 10 ml of cRPMI was added to the mortar and the femur bones were gently crushed. The resulting media was collected, filtered through a 70-µm filter and placed in a conical tube. The filtered supernatant was centrifuged at 100 g (150 relative centrifugal force) for 5 min. Cells were resuspended, counted and plated at a density of 3×10^6 cells per 10-cm dish in 10 ml of macrophage growth media (cRPMI containing 25% macrophage-colony stimulating factor (M-CSF) containing L929 conditioned media (made in-house)). Cells were left to grow for 7 days to differentiate and were supplemented with 5 ml of macrophage growth media on day 5. On day 7, BMDMs (yielding $10–12 \times 10^6$ cells per 10-cm dish) were lifted off the plate using cold phosphate-buffered saline (PBS) containing 5 mM EDTA. BMDMs were counted and replated in macrophage growth media overnight before experiments. On the day of experiments, macrophage growth media was replaced with cRPMI 6 h before stimulation to remove M-CSF. M2 polarization was performed by stimulating macrophages with 10 ng ml−1 recombinant mouse IL-4 (PeproTech). For M1 polarization macrophages were stimulated with 100 ng ml−1 LPS (LPS EK-Ultrapure, InvivoGen). To induce senescence, day 7 BMDMs were either irradiated (10 Gy) or treated with Doxo (Fisher) for 24 h at 500 nM in 60% cRPMI/40% macrophage growth media. DNA-damaged cells were left in culture for 10 days and media components were replaced every 2–3 days. As a negative control, a

mock irradiated or drug-treated condition was cultured in parallel and required passing every 2–3 days. All senescent macrophage experiments were performed 10–13 days post DNA damage.

4.2 Reverse transcription-quantitative PCR and primers

For all human PBMC and mouse BMDM cell-culture experiments, RNA was isolated using RNA STAT 60 (Amsbio) as per the manufacturer's protocol. Approximately 2,000 ng of RNA was converted to complementary DNA using a High-Capacity cDNA Reverse Transcription Kit (Applied Biosystems). Gene expression was measured using a CFX384 Real Time System (Bio-Rad) and Thermo Scientific Maxima 2× SYBR Green. Data were analyzed using Bio-Rad CFX Maestro 3.1 software and normalized using the $2^{-\Delta\Delta Ct}$ method. Mouse BMDM genes were normalized to hypoxanthine phosphoribosyltransferase (Hprt). For in vivo experiments, RNA was extracted from flash-frozen liver, VAT, kidney and heart using RNA STAT 60 in a TissueLyser system (Qiagen). cDNA was generated as described above, and gene expression was measured using iCFX384 Real Time System (Bio-Rad) and Thermo Scientific Maxima 2× SYBR Green. Expression was normalized to Hprt by the $2^{-\Delta\Delta Ct}$ method automatically using Bio-Rad CFX Maestro (v.0.3.1) with the gene-specific primer pairs listed below. All primers are written in the $5' \rightarrow 3'$ direction.

For mouse genes, the following primer pairs were used: *Cdkn1a* (forward: TTGCCAGCAGAATAAAAGGTG; reverse: TTTGCTCCTGTGCGGAAC), Cdkn2a (forward: AACTCTTTCGGTCGTACCCC; reverse: TCCTCGCAGTTCGAATCTG), Cd38 (forward: GTATGGCCTTGCTGGAATAG; reverse: TTGAAGGCTGTTAGTGGAATAG), Gdf15 (forward: CCGAGAGGAACTCGAACTCAG; reverse: GGTTGACGCGGAGTAG), Hprt (forward: TTTCCCTGGTTAAGCAGTACAGCCC; reverse: TGGCCTGTATCCAACACTTCGAGA), Cd38 (Exon 2; forward:

GGAGCATTTGTTTCCAAGAAC; reverse: GAGAGTCTTGTTACATGGTATGG), Ifnβ (forward: GCACTGGGTGGAATGAGACTATTG; reverse: CTCCCACGTCAATCTTTCCTCTTG), Ifnα (forward: GGATGTGACCTTCCTCAGACTCATA; reverse: GAATCCAAAGTCCTTCCTGTCCTTC), Abca1 (forward: GCCAAGCATCTTCAGTCCATCAG; reverse: CAGTGTAGCAGGGACCACATAA), Plin2 (forward: TCTGAGGTCAAAGCTCAGTAAAC; reverse: AGCCATCTACCAAGTTAATTTCAATAC), Il6 (forward: ACAAAGCCAGAGTCCTTCAGAGAG; reverse: AGAACTGATGAGAGGGAGGCCATT), Il10 (forward: GCTCTTACTGACTGGCATGAG; reverse: CGCAGCTCTAGGAGCATGTG), Fizz1 (forward: TCCAGCTGATGGTCCCAGTGAATA; reverse: ACAAGCACACCCAGTAGCAGTCAT), Mgl1 (forward: TGCAACAGCTGAGGAAGGACTTGA; reverse: AACCAATAGCAGCTGCCTTCATGC), Mrc1 (forward: TGGGCTACAGGAGAACCCAACTTT; reverse: GCAGTGGCATTGATGCTGCTGTTA), Arg1 (forward: ACCTGGCCTTTGTTGATGTCCCTA; reverse: AGAGATGCTTCCAACTGCCAGACT), Ym1 (forward: AGAAGGGAGTTTCAAACCT; reverse: GTCTTGCTCATGTGTGTAAGTGA), Cd36 (forward: TCATGCCAGTCGGAGACATGCTTA; reverse: AACTGTCTGTACACAGTGGTGCCT), Mgl2 (forward: GCATGAAGGCAGCTGCTATTGGTT; reverse: TAGGCCCATCCAGCTAAGCACATT), Il12b (forward: TGCCCTCCTAAACCACCTCAGTTT; reverse: TTTCTCTGGCCGTCTTCACCATGT), Mmp12 (forward: CTGGACAACTCAACTCTGGCAATAA; reverse: TGAGGTACCGCTTCATCCATCT), Bcl2l11 (forward: GACCACCCTCAAATGGTTATCT; reverse:

GTTCTCCCAGTCTGAACAAGAG), Bbc3 (forward: CCTGGAGGGTCATGTACAATCT; reverse: CACCTAGTTGGGCTCCATTTCT), Bid (forward: GCTCCTTCAACCAAGGAAGAATA; reverse: GGTCCATCTCATCGCCTATTTG), Bcl2l1 (forward: TGGTCGACTTTCTCTCCTACAA; reverse: CCCTCTCTGCTTCAGTTTCTTC), Mcl1 (forward: CTAGAAGGCGGCATCAGAAATG; reverse: CCTATTGCACTCACAAGGCTATC), Bcl2l2 (forward: GTGGGTAGAAGCTTTGGTAGTT; reverse: AGACTCAGCTGGATAGAGAGAC), Ccl4 (forward: AGCTCTGTGCAAACCTAACC; reverse: GGTGTAAGAGAAACAGCAGGAA), Il18 (forward: GCCAGAAGCAGACTCCTTAAT; reverse: ACACCAGGAAATCGTTACCC), Oas1a (forward: GACGCTGGACAAGTTCATAGAG; reverse: CTTGGAAGCATCTCTCCTTCAG), and Cmpk2 (forward: GTTCCTCATTACACCGGAGAAG; reverse: GCTCAGTCAGTCAGAAGGAAAG). For human genes, the following primer pairs were used: TREM2 (forward: GAGCCTCTTGGAAGGAGAAATC; reverse: TGGCTGCTAGAATCTTGATGAG), IFNA (forward: CCAGCAGATCTTCAACCTCTTT; reverse: GGTAGAGTTCGGTGCAGAATTT), IFNB1 (forward: GCTTCTCCACTACAGCTCTTTC; reverse: CAGTATTCAAGCCTCCCATTCA), GDF15 (forward: GGAATCTGGAGTCTTCGGAGTG; reverse: CACGTATGTCATCAGCAGAGAG), MMP9 (forward: TCACTTTCCTGGGTAAGGAGTA; reverse: CTGTCAAAGTTCGAGGTGGTAG), MMP12 (forward: CTAGTGATCCAAAGGCCGTAAT; reverse: CACGTATGTCATCAGCAGAGAG), P16 (forward: GAGCAGCATGGAGCCTTC; reverse: CGTAACTATTCGGTGCGTTG), and P21 (forward: TCACTGTCTTGTACCCTTGTGC; reverse: GGCGTTTGGAGTGGTAG).

4.3 Multi-omic analysis

Transcriptomics – Mouse BMDM-derived and human PBMC-derived macrophage cultures were lysed with RNA STAT 60 (Amsbio) and ~50 ng per µl of RNA was submitted to the UCLA's Technology Center for Genomics and Bioinformatics (TCGB) core for library preparation and 2 × 100 paired-end sequencing. Roughly 100 million high-quality reads were sequenced per sample using NovaSeq X Plus (Illumina). Raw data in FASTAq format were filtered for adapter sequences or low-quality sequences using SOAPnuke. Reads were aligned to the mm10 reference genome using STAR. Aligned reads were processed using TopHat and a counts matrix was generated using FeatureCounts. Raw reads were processed using R (v.4.5.0) and DESeq2 (v.1.48.2) where the raw reads were normalized to gene length then transformed into transcripts per million (TPM). Genes with a TPM value of 10 or greater were kept for normalization using $\log_2$ and quantification. Differentially expressed genes (DEGs) were determined using parametric tests (ANOVA) and P values were corrected for false positives using false discovery rate (FDR) tests for q values. Gene interactions with a q value <0.05 were assessed for net effect size and genes with $\log_{10}$(fold change) ($\log_2$(FC)) >0.32 were considered a DEG. All heatmaps were made using the latest version of pheatmap (v.1.0.12) and all statistics were performed using base R commands.

Proteomics – Liquid chromatography–mass spectrometry (LC–MS) proteome analysis was performed on an Orbitrap Ascend Tribrid Mass Spectrometer using data-independent acquisition (DIA). The tuning method details were as follows: positive ionization (2,500 V), ion injection time (100 ms), DIA window (12 Da), MS2 range (400–1,000), AGC (100%) and HCD energy (30%). For liquid chromatography, peptides were trapped on an EXP2 Stem Trap column and separated using a 200-cm µPAC column from PharmaFluidics. The entire setup was connected with 20 µm internal diameter Viper capillaries (Thermo Fisher Scientific) and

maintained at 55 °C in a column oven. The reversed-phase analytical gradient was delivered as follows. Mobile phase A: 0.1% formic acid (FA) in water; mobile phase B: 0.1% FA in acetonitrile (ACN). Start at 8% B, linear ramp to 25% B at 70 min, linear ramp to 37% B at 95 min, jump to 98% B at 96 min and hold for 9 min, drop back to 8% B at 105 min and hold for 5 min (110 min total). The loading pump was connected to three solvents: 0.1% FA in water (loading buffer A), 0.2% FA in 70% ACN and 30% water with 5 mM ammonium formate (loading buffer B) and 0.2% FA in 50% isopropanol, 30% ACN, 20% water and 5 mM ammonium formate (loading buffer C). At the start of the method, the loading pump delivered 50% B and 50% C at 50 µl min−1 to 5 min. The solvent was switched to 100% A at 6 min and ended at 62 min. The loading pump flow rate was reduced to 10 µl min−1 at 70 min and held to the end of the gradient. Proteomic raw files were analyzed with DIA-NN v.1.9 and Python v.3.9.7 was used for proteomic data analysis. Proteins with missing values were removed and z-score normalization was applied to the dataset before one-way ANOVA analysis. Uniform Manifold Approximation and Projection (UMAP) analysis was performed with the Python packages 'UMAP'.

Metabolomics – Metabolome analysis was performed on an Orbitrap Ascend Tribrid Mass Spectrometer using a direct injection method. Thermo (.RAW) files were converted to mzML files using ms convert. The produced mzML files were analyzed with MZmine3 software for mass detection, feature detection, alignment, gap filling and feature filter. The output files contain m/z and quantification by field asymmetric ion mobility spectrometry compensation voltage peak area. For metabolite annotation, we applied a direct infusion-based data-dependent acquisition tandem mass spectrometry analysis with the same sample and the same compensation

voltages applied in direct injection metabolomic analysis. The MS2 spectrum of metabolites was then compared with the library and analyzed through the GNPS website. Python (v.3.9.7) was used for metabolomic data analysis. Z-score normalization was applied to the dataset before one-way ANOVA. PCA analysis was performed with the Python package 'sklearn'.

SASPomics – The conditioned media from the cell cultures under different tensions and senescence induction were concentrated to ~30 µl using 3 kDa molecular cut-off filters (Millipore Sigma) and protein content was quantified using the bicinchoninic acid assay. Aliquots of concentrated secretome (50 µg) from each sample were reduced using 20 mM dithiothreitol in 50 mM triethylammonium bicarbonate buffer (TEAB) at 50 °C for 10 min, cooled to room temperature, held at room temperature for 10 min, and alkylated using 40 mM iodoacetamide in 50 mM TEAB at room temperature in the dark for 30 min. Samples were acidified with 12% phosphoric acid to obtain a final concentration of 1.2% phosphoric acid. S-Trap buffer consisting of 90% methanol in 100 mM TEAB at pH ~7.1, was added and samples were loaded onto S-Trap micro spin columns. The entire sample volume was spun through S-Trap micro spin columns at 4,000g and room temperature, binding the proteins to the micro spin columns. Subsequently, S-Trap micro spin columns were washed twice with S-Trap buffer at 4,000g at room temperature and placed in clean elution tubes. Samples were incubated for 1 h at 47 °C with 2 µg of sequencing grade trypsin (Promega) dissolved in 50 mM TEAB. Afterwards, trypsin solution was added again in the same amount, and proteins were digested overnight at 37 °C. Peptides were sequentially eluted from S-Trap micro spin columns with 50 mM TEAB, 0.5% FA in water and 50% ACN in 0.5% FA. After centrifugal evaporation, samples were resuspended in 0.2% FA in water and desalted with Oasis 10 mg Sorbent Cartridges (Waters). The desalted elutions were then subjected to an additional round of centrifugal evaporation and resuspended in 30 µl of 0.2%

FA in water. Finally, indexed Retention Time standard peptides (iRT; Biognosys) were spiked in the samples according to manufacturer's instructions.

LC–MS/MS was performed on an Eksigent Ultra Plus nano-LC two-dimensional HPLC system (Dublin) combined with a cHiPLC system directly connected to an orthogonal quadrupole time-of-flight Sciex TripleTOF 6600 mass spectrometer). The solvent system consisted of 2% ACN, 0.1% FA in H2O (solvent A) and 98% ACN, 0.1% FA in H2O (solvent B). Proteolytic peptides were loaded onto a C18 pre-column chip (200 µm × 6 mm ChromXP C18-CL chip, 3 µm, 300 Å; Sciex) and washed at 2 µl min−1 for 10 min with the loading solvent (0.1% FA in H2O) for desalting. Peptides were transferred to the 75 µm × 15 cm ChromXP C18-CL chip, 3 µm, 300 Å (Sciex) and eluted at 300 nl min−1 with the following gradient of solvent B: 5% for 5 min, linear from 5% to 8% in 15 min, linear from 8% to 35% in 97 min, and up to 80% in 20 min, with a total gradient length of 180 min. Samples were analyzed by DIA using 64 variable-sized windows covering the m/z 400–1,250 range. Mass spectrometry scans were collected with 250-ms accumulation time, and tandem mass spectrometry (MS/MS) scans with 45-ms accumulation time in 'high-sensitivity' mode. The collision energy for each segment was based on the z = 2+ precursor ion centered in the window with a collision energy spread of 10 or 15 eV.

DIA–MS data were processed using Spectronaut, in-house customized spectral libraries (Buck Institute) and queries were performed against human databases (UniProt–SwissProt). Data extraction parameters were selected as dynamic using nonlinear iRT calibration. Identification was performed using 1% precursor and protein q values. Quantification was based on the MS/MS peak areas of three to six best fragment ions per precursor ion, iRT profiling was selected, interference correction was selected and no normalization was applied. Differential protein

abundance analysis was performed using an unpaired t-test, and P values were corrected for multiple testing, using the Storey method. Protein groups with at least two unique peptides, $q \leq 0.001$ and absolute $\log_2(FC) \geq 0.58$ were considered to be significantly altered.

4.4 Immunofluorescence and tissue staining

Cells were transferred to six-well plates including coverslips. After 24 h, attached cells were fixed in 4% formaldehyde, then permeabilized in 0.25% Triton X-100. Subsequently, cells were blocked in 0.1% PBS with 3% bovine serum albumin (BSA) and 0.1% Tween-20, followed by incubation with the primary antibodies overnight. Cells were washed and incubated with the appropriate secondary antibodies for 1 h. The cells were washed and transferred to mounting media (Antifade GOLD reagent with DAPI; Thermo Fisher Scientific). A 3i Spinning Disk Confocal microscope (Marianas) consisting of a CSU-X1 A1 Spinning Disk (Yokogawa) attached to a Zeiss Axio Observer 7 microscope was used. Standard filter sets were used for imaging. Pearson's correlation coefficients were calculated using the JACoP plugin on ImageJ. Mouse livers were collected and either fixed in formalin or mounted into Optimal Cutting Temperature Compound Freezing Medium (OCT) and frozen at −80 °C. Tissue samples were sectioned at 5-µm thick and mounted onto slides for immunofluorescence. For in vivo tests, paraffin slides were dewaxed in SafeClear (Fisher Scientific) and ethanol, then antigens were unmasked at 95 °C in 10 mM sodium citrate with 0.05% Tween-20. OCT slides were allowed to acclimate to room temperature, then fixed in cold acetone and permeabilized with PBS with 0.1% Triton X-100 and 1% BSA. All slides were blocked in PBS with 5% BSA and 0.1% Triton X-100 and incubated overnight with primary antibodies at a 1:200 dilution. Slides were washed and incubated with secondary antibodies at a 1:500 dilution for 1 h. After washing, slides were mounted in VECTASHIELD antifade mounting medium with DAPI (Vector Laboratories) and

imaged with an Axioplan 2 fluorescent microscope (Zeiss) equipped with ×10–20 differential interference contrast objectives and Axiovision Rel 3.0 software (Zeiss). Cell counts from tiled whole-tissue images of slides were generated on QuPath (v.0.6.0) cell counter. F4/80+ macrophage counts and p21+ cells were quantified using QuPath's object classification tools. For immunofluorescence staining, the following primary antibodies were used: anti-TOM20 (rabbit; Proteintech, cat. no. 11802-1-AP; 1:1,000), anti-dsDNA (Abcam, cat. no. ab27156-1002; 1:1,000), anti-F4/80 (rat; Abcam, cat. no. ab6640; 1:200) and anti-p21 (rabbit; Abcam, cat. no. ab188224; 1:200).

4.5 Western blot analysis and antibodies

Cell-culture lysates from both mouse and human macrophages were prepared by lysing cells in RIPA Buffer containing Halt protease and phosphatase inhibitor cocktail 1:100 (Thermo Fisher). Protein concentrations were determined using the BCA Assay kit (Thermo Fisher). Approximately 10–20 μg of delineated protein in sodium dodecyl sulfate (SDS) was loaded onto 4%–20% polyacrylamide gels to separate by molecular weight via gel electrophoresis. Proteins were then transferred to polyvinylidene difluoride membranes. Polyvinylidene difluoride blots were placed in 5% milk for unspecific binding for 1 h, then exposed to primary and secondary antibodies. Western quantification was performed using ImageJ (v.150i). For immunoblotting, primary antibodies were used at a dilution of 1:1,000 unless otherwise specified. The following antibodies were used: anti-β-Tubulin (rabbit; Cell Signaling Technology, cat. no. 2146S), anti-Lamin B1 (rabbit; Cell Signaling Technology, cat. no. 13435 T), anti-phospho-Histone H2AX (γH2AX) (rabbit; Cell Signaling Technology, cat. no. 9718T), anti-phospho-NF-κB p65 (rabbit; Cell Signaling Technology, cat. no. 3033T), anti-NF-κB p65 (rabbit; Cell Signaling Technology, cat. no. 8242T), anti-p21 (rabbit; Abcam, cat. no. ab188224), anti-TREM2 (rat;

Invitrogen, cat. no. MA5-28223), anti-CMPK2 (rabbit; Abcam, cat. no. ab139720) and anti-p16 (Abcam, cat. no. 211542).

4.6 Shotgun lipidomics

Senescent macrophages and passage control macrophages were subjected to shotgun lipidomics using publicly accessible methods58. Briefly, media was removed and replaced with 1 ml of ice-cold PBS, then cells were scraped with cell lifters and spun down in glass tubes at 365g for 5 min at 4 °C. A modified Bligh and Dyer extraction was carried out on lifted cells, then 13-lipid class Lipidyzer Internal Standard Mix (AB Sciex, cat. no. 5040156) was added to each sample, before biphasic extraction. Following two successive extractions, pooled organic layers were dried down in a Genevac EZ-2 Elite. Lipid samples were resuspended in 1:1 methanol/dichloromethane with 10 mM ammonium acetate then transferred to robovials (Thermo Scientific, cat. no. 10800107) for analysis. Samples were analyzed for targeted quantitative measurement of 1,100 lipid species across 13 classes. Quantitative values were normalized to cell counts and average cell volume.

4.7 *In vivo* experiments

Generation of MASLD mouse model – CETP-APOE*Leiden mice (homozygous for transgene) were maintained on a C57BL/6J background then crossed with three distinct strains of mice with known response to liver fibrosis51. These strains were: 129/SvJ (fibrosis-resistant), C57BL/6J (medium-fibrosis) and BXD19/TyJ (fibrosis-prone), and male F1 progeny were used for experiments. Animals were maintained on a 12-h light–dark cycle with ad libitum access to water. Twenty-five male mice per strain (8–10 weeks old) were fed HFHCD (33% kcal from cocoa butter and 1% cholesterol; Research Diets, cat. no. D10042101) for 16 weeks. At the end of the study, mice were fasted for 4 h, beginning at 10:00 am and were killed at 2:00 pm.

Quantitative assessment of serum lipids and fibrosis in the liver – Liver lipids were extracted as previously described59 and 100 mg of liver was used for lipid extraction; the dried organic extract was dissolved in 1.8% (w/v) Triton X-100. The amount of lipids in each extract was determined using a colorimetric assay from Sigma (triglyceride, total cholesterol and unesterified cholesterol) and Wako (phospholipids) according to the manufacturers' instructions. For histological examination and fibrosis quantitation, livers were fixed in 10% formalin, embedded in paraffin, sectioned at 5 μm and stained with picrosirius red. The fibrosis score was assessed by a pathologist blinded to the study, according to the MASLD Clinical Research Network60.

Oil Red O staining – Oil Red O staining was performed as described previously61. Sections were imaged using a Zeiss Axiolab microscope and Axiocam 305 color camera (Carl Zeiss Microscopy) with a ×10 objective. An average of eight images was taken across the liver sections for each experimental condition as described61. Similarly, for lipid droplet size, eight images per field per liver section were analyzed using the Analyze Particle function in ImageJ with Feret's diameter to determine the average size (μm2).

4.8 Human macrophage culture

Although sex and gender information was not recorded, blood from biological male or female human donors was collected and PBMCs were isolated at UCLA's Virology Core. Some 100 × 106 blood cells were collected from three to five donors with no clinical information. PBMCs were centrifuged at 100g for 5 min then 25 × 107 single cells were seeded onto 10-cm polystyrene-treated culture plates (VWR) with 10% adherence and allowed to differentiate into macrophages in the presence of 50 ng ml−1 human M-CSF recombinant protein (PeproTech, cat. no. 300-25-100) in the same RPMI composition above. Cells were provided with an additional

5 ml of M-CSF-containing medium 5 days into differentiation. Seven days after seeding, confluent macrophage cultures were placed under similar senescence-inducing conditions using irradiation and Doxo (Thermo Fisher)**.**

4.9 Synthetic guide RNA design and CRISPR

Synthetic guide RNA design – Synthego Knockout Guide design was utilized to generate synthetic guide sequences targeting exon 1 of the Cmpk2 gene. The top two synthetic guide sequences generated by the software were purchased from Synthego and targeting efficiency was assessed via Synthego's Inference of CRISPR Edits analysis platform and immunoblotting. Guides that produced indel scores of 50 or above were used for experimentation. Negative control guides targeting the Rosa26 allele were also purchased from Synthego. The guide sequences were as follows: guide 1, ATGGCCCTAATAAGCCGCCC; guide 2, CCCTCGAGCCCCACTGTGGC.

CRISPR – CRISPR-Cas9 ribonucleoprotein editing of macrophage precursors isolated from murine bone marrow was performed as previously reported62. CRISPR-Cas9 ribonucleoprotein complexes were created by combining nuclease-free water, synthetic single guide RNA (Synthego, 1.5 nmol) and Alt-R Cas9 electroporation enhancer (IDT, 10 nmol) in a 1.5-ml tube. In a separate 1.5-ml tube, SpCas9-NLS (Macrolab, 40 pmol) was diluted 1:5 in nuclease-free water. The diluted SpCas9-NLS was then added to the sgRNA/IDT enhancer mixture in a 1:1 ratio and incubated at room temperature for 10 min. Macrophage precursors were then electroporated using a Neon NxT Electroporation System (Invitrogen) with the following parameters: 1,900 V, 20 ms, 1 pulse. Electroporated cells were then transferred to 1.5-ml tubes containing pre-warmed macrophage growth medium, and incubated for 1 h at 37 °C, 5% CO2 before collection.

4.10 Statistics

Sample size and statistical analyses were determined before data collection. Sample sizes were chosen based on mouse availability and experimental feasibility. No statistical methods were used to pre-determine sample sizes for in vitro and in vivo studies. No data were excluded from the analyses. All in vitro experiments used at least three biological replicates to meet the minimum requirements for parametric statistical testing. The number of mice for each in vivo experiment was determined by mouse availability. Aged mice or and MASLD mice were pre-determined for in vivo experiments and removed from studies if mice contained tumors or became ill. All in vitro experiments used at least three biological replicates to meet the minimum requirement for parametric statistical testing. Data distribution was assumed to be normal, but this was not formally tested. *In vitro* experiments for transcriptomics, proteomics, metabolomics and SASP-proteomics required at least four to six biological replicates, which were determined by sample availability and sequencing efficiency. The number of mice for each in vivo experiment was determined by mouse availability and by prior similar studies with expected similar effect sizes. Power analysis was not performed to determine cohort size, as discussed above, instead the size was determined by animal availability and mouse number used in prior similar studies with expected similar effect size. In Fig. 3a, eight aged C57BL/6J male mice (22–24 months) and eight young mice were used to match the aged mice cohort size. In Fig. 3b, two aged (19 months) male livers were used based on liver tissue availability and two young (3 months) male livers were used to match the aged mice cohort. In Fig. 3c, representative images of one mouse per age, aged male (24 months) and young male (3 months) was used based on tissue availability for this qualitative study. For in vivo experiments in Fig. 6f–k a sample of n = 12 C57BL/6J male mice (24 months) was determined by animal availability. Six aged mice

were allocated per experimental condition (vehicle versus ABT). One vehicle control mouse died, therefore the final vehicle control in n = 5. A sample of n = 6 young male mice was determined to match the aged mice cohort size. In Fig. 7a–e in vivo experiments that involved HFHCD with the CTEP APOE mutant mice, 25 male mice per strain (8–10 weeks old) were used. In Fig. 7g–s 20 CTEP APOE mutant male mice crossed to C57BL/6J mice were generated across three cohorts. An even number of mice was allocated per condition as a vehicle control or treated with ABT-263. In Extended Data Fig. 1i–m, between six and ten male young (3 months) and aged (26 months) CD38 KO mice were used for in vivo gene expression experiments. The experiments were not randomized. Investigators were not blinded to allocation during experiments and outcome assessment. Statistical analyses were performed using the latest Prism (v.10.6.1) and R (v.4.5.2). The specific statistical tests used for each experiment are described in the figure legends. All tests were two-sided unless otherwise stated, and $P < 0.05$ was considered statistically significant. Individual data points are shown where appropriate to illustrate the distribution and variability of the data. All experiments were repeated independently three times with similar results. Detailed protocols and analysis methods are provided to ensure reproducibility.

Chapter 5:

Results

5.1 Exogenous DNA damage drives *Cdkn1a* (p21)+ senescence in macrophages in vitro

To test whether macrophages can undergo an irreversible and stable form of cellular senescence, mouse bone marrow-derived macrophages (BMDMs) were subjected to ionizing irradiation (IR) or doxorubicin (Doxo) (Fig. 1a). Ten days after DNA damage, we observed a decrease in the proliferation marker Ki-67 and Lamin B1, a nuclear protein whose expression decreases with senescence (Fig. 1b). We also observed increased pNF-κB, which likely results from the acquisition of cellular senescence and not activation of the acute DNA damage response, because it occurs post gain and loss of pH2A.X24. In support, we found that both IR and Doxo increased cell size and elevated SA-β-gal activity, leaving cells arrested in the G2–M phase, accompanied by >4 N genomes (Fig. 1c–e). DAPI imaging showed that control macrophages had a uniform nuclear size and shape, whereas IR- and Doxo-treated macrophages were larger and irregularly shaped (Fig. 1f). Machine learning and neural network tools have been deployed to identify senescent cells from nonsenescent cells using nuclear imaging derived from DAPI-stained cells25. Using this approach, we found that the probability of IR-treated macrophages being senescent is greater than that for control cells (Fig. 1g). To further examine this, macrophages were stained with a CellTrace Violet (CTV) dye before IR. Interestingly, ~20% of labeled cells divided 1 day post IR, but all cells stopped dividing between 5 and 10 days, suggesting a stable cell-cycle arrest phenotype (Fig. 1h). Collectively, our data show senescent macrophages acquire multiple hallmarks of senescence, including permanent cell-cycle arrest, 10 days post IR or Doxo, and they are referred to here as Sen(IR) or Sen(Doxo), respectively.

Senescent cells are characterized by increased expression of cell-cycle inhibitor genes, such as *Cdkn1a* (p21) and *Cdkn2a* (p16), as well as SASP genes. Accordingly, we measured the

expression levels of these genes in Sen(IR) and Sen(Doxo) macrophages. We found that *Gdf15*, *Mmp9* and *Cdkn1a*, but not *Cdkn2a*, were upregulated in senescent macrophages relative to control (Fig. 1i). Of note, most studies investigating senescent macrophages have used expression of *Cdkn2a* (p16) as a positive indicator of macrophage senescence or p16 reporter mice to identify and target these cells for clearance. To investigate whether p16 expression can be used to target senescent macrophages, we obtained BMDMs from a transgenic mouse model that contains a tri-modality reporter (3MR) on the p16 locus (p16-3MR). One of the three reporters drives apoptosis via ganciclovir (GCV) treatment. Interestingly, we found that p16-3MR senescent macrophages were resistant to cell death and apoptosis, while control macrophages were more sensitive to GCV (Extended Data Fig. 1a–c). These data suggest that senescent macrophages downregulate p16, relative to control cells, sparing them from apoptosis. In fact, in a previous study, we found that in Doxo-treated p16-3MR mice, GCV reduced Cdkn2a mitochondrial RNA expression in the liver but not *Cdkn1a*. Therefore, p16+ and p21+ senescent cells can be distinct populations in aging tissues, as supported by recent studies showing divergent SASP programs and trajectories for $p16^{+}$ versus $p21^{+}$ senescent cells across tissues. In addition to p21, we also discovered that senescent macrophages express canonical markers of M1 and M2 macrophages, which highlights the challenge of distinguishing senescent and nonsenescent macrophages (Fig. 1i). However, using transcriptomics, proteomics and metabolomics, we found senescent macrophages formed unique clusters from M0 (a naive state), M1 and M2 conditions suggesting that senescent macrophages are distinct from the classic M1 and M2 paradigm (Fig. 1j–l).

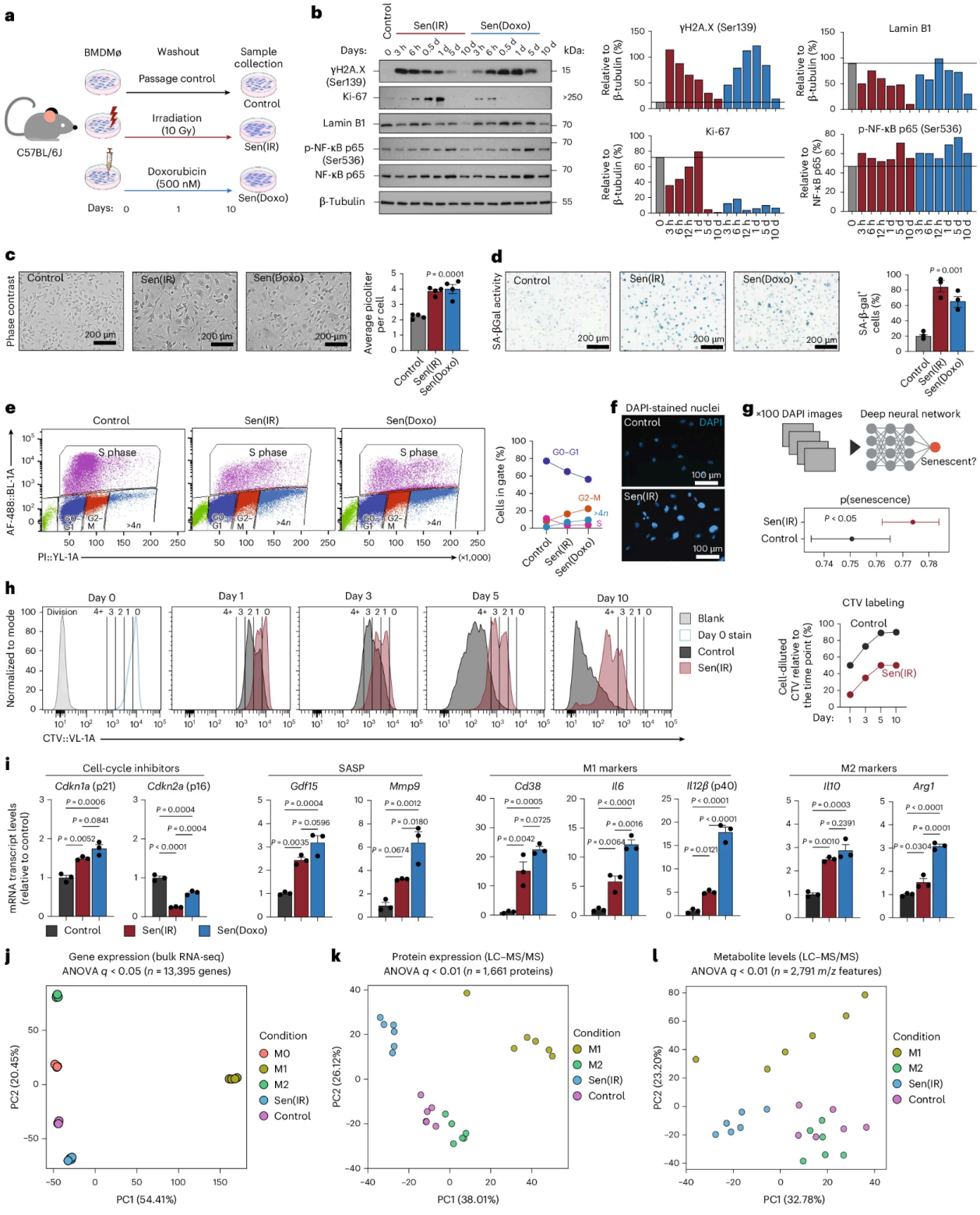
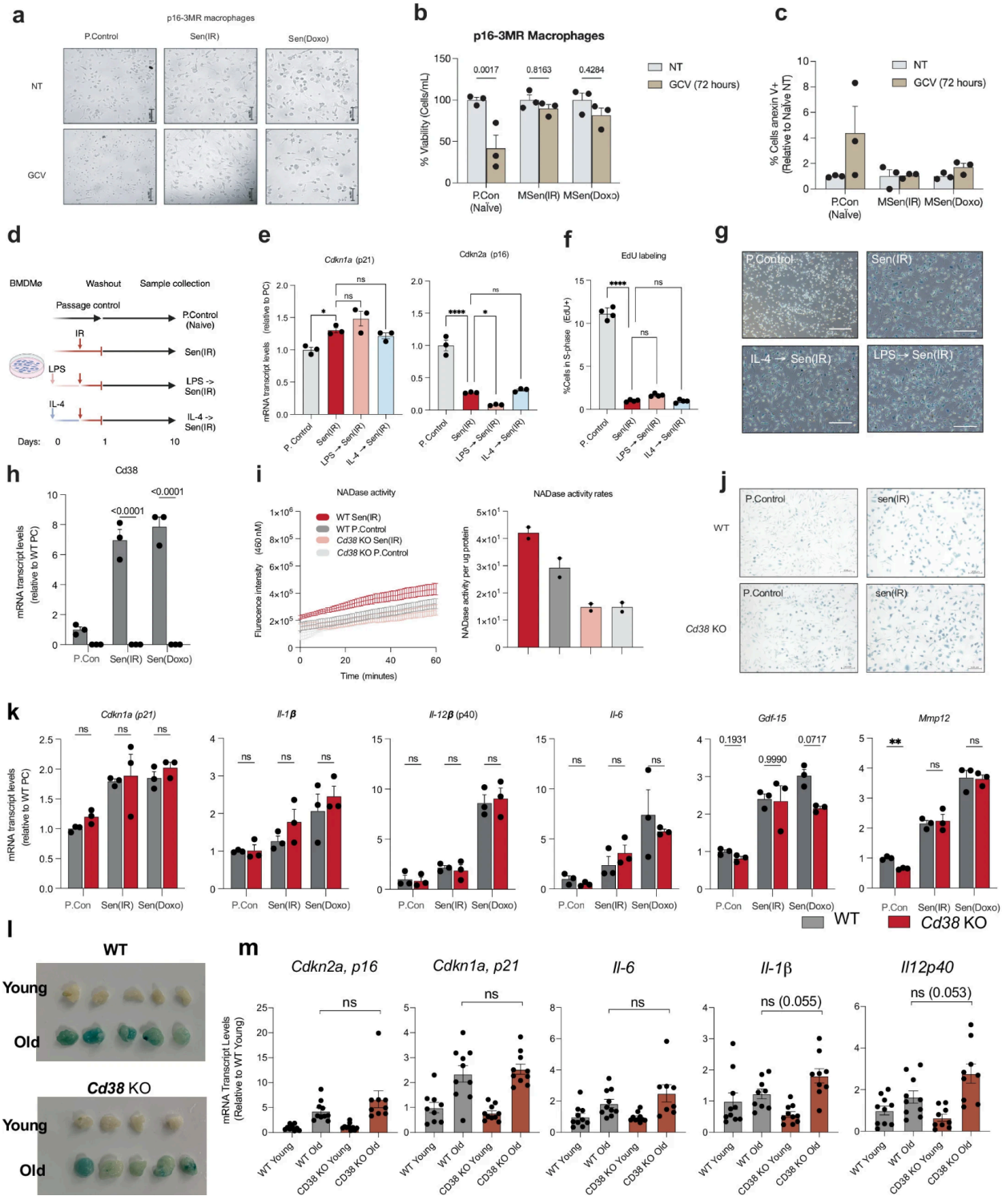


Figure 1. a, The in vitro model system using exogenous DNA damage with irradiation and Doxo from male C57BL/6J mice. **b**, SDS–PAGE gels and immunoblotting (western blot) with ImageJ

quantification relative to loading control. **c**, Representative phase contrast images as well as cell volume quantification via flow cytometry. Average ± s.e.m. cell volume (pl) of n = 4 biological replicates. P value derived from ANOVA. **d**, SA-β-Gal images and average ± s.e.m. percent positive cell quantification by microscopy at ×20 magnification. n = 3 biological replicates. P value from ANOVA. **e**, Click-iT EdU labeling with propidium iodide (PI) labeling of cells to assess cell-cycle dynamics. Axes represent the percentage of cells positive for the stain, compared to the parental gate, as detected by flow cytometry. **f**, Representative images of control and senescent macrophages, DAPI-stained nuclei at ×20 magnification. **g**, Probabilistic deep-learning algorithm to generate a predicted senescence score. Average score ± 95% confidence interval, of 100 biologically independent DAPI images. P value derived from a two-sided t-test. **h**, CTV staining 24 h post IR. Dilution of CTV was performed at the represented time points via flow cytometry. Percent cells that diluted CTV from the previous day were quantified and trendlines are shown (right). **i**, Mean ± s.e. mRNA transcript levels (reverse transcription-quantitative polymerase chain reaction (RT–qPCR)) normalized to control. n = 3 biological replicates. P value derived from Tukey's test post-ANOVA analysis. **j**, PCA on bulk RNA-seq samples from day 7 BMDMs either unactivated (M0), or treated with 12 h of 100 ng ml−1 LPS (M1) or 18 h of 10 ng ml−1 IL-4 (M2), compared to senescent macrophages (Sen(IR), 10 days post irradiation) and (control) unactivated macrophages cultured for 10 days alongside senescent macrophages. **k**, PCA projections from senescent macrophages (Sen(IR), 10 days post irradiation), passage control condition (control) and passage control plus LPS (M1) or IL-4 (M2). **l**, PCA analysis from senescent macrophages (Sen(IR), 10 days post irradiation), passage control condition (control) and passage control plus LPS (M1) or IL-4 (M2). BMDMø, bone marrow-derived macrophage; p(senecence), predicted senescence.

Using this model, we interrogated proposed mechanisms regulating senescence in macrophages. To start, interleukin-4 (IL-4), a type 2 (T helper 2) cytokine, is proposed to be protective against macrophage senescence through a DNA damage repair mechanism17 similar to the effects of lipopolysaccharide (LPS), which can protect against DNA damage27. To test whether LPS or IL-4 can protect against DNA damage-induced senescence, BMDMs were activated with LPS or IL-4 before IR (Extended Data Fig. 1d). Ten days post IR, IL-4 or LPS pretreatment did not significantly prevent Cdkn1a and Cdkn2a expression, prevent cell-cycle arrest or decrease SA-β-gal activity (Extended Data Fig. 1e–g). Next, CD38 has been reported to drive macrophage senescence through heightened NAD+ consumption18. Interestingly, we also observed heightened Cd38 mRNA expression and CD38-mediated NADase activity in senescent macrophages (Extended Data Fig. 1h,i). Therefore, we hypothesized that elevated CD38 activity may drive senescence as recently proposed18. To test this, Cd38 knockout (KO) BMDMs were subjected to the Sen(IR) and Sen(Doxo) models. However, we found no difference in SA-β-gal activity or SASP gene expression in Cd38 KO senescent macrophages compared to wild type

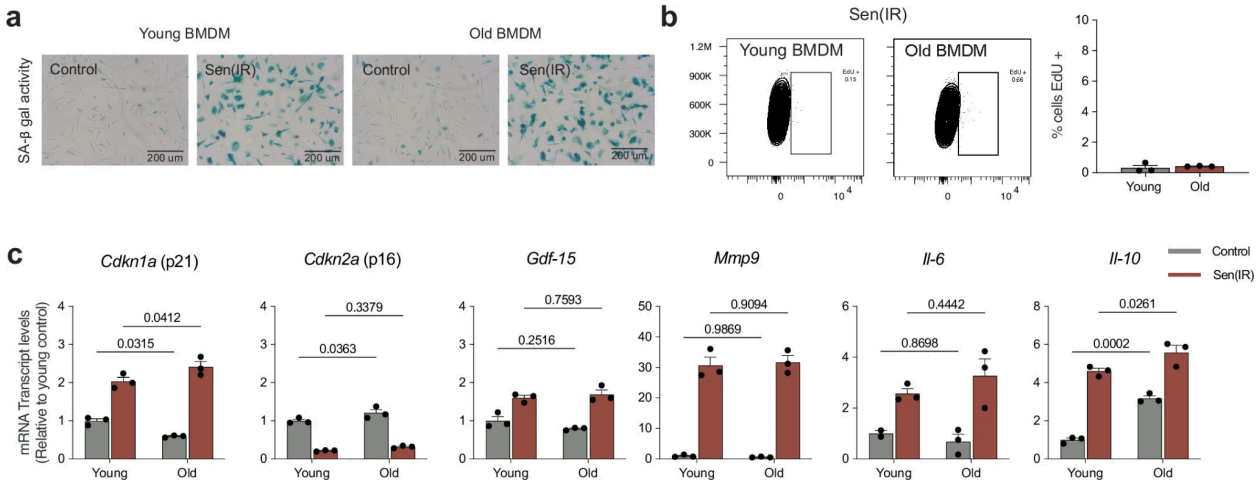


Extended data figure 1. (a) Phase contrast images from BMDM macrophages from p16-3MR mouse models. Control and senescent macrophages treated with ganciclovir (GCV) for 72 hours.

P values represent post-hoc tests from a 2-way ANOVA. **(b)** Percent cells (live cells / dead cell gate) in liquid suspension after removal from tissue culture plates. **(c)** Percent cells stained for Annexin V (a known marker of apoptosis) relative to non-treated control macrophages. **(d)** Model of pre-polarization with LPS (100 ng/mL) and IL-4 (10 ng/mL) followed by Irradiation on macrophages. Analysis was performed 10 days post 10 Gy irradiation. **(e)** Mean, +/− SE, gene expression (RT-qPCR) normalized to control. N = 3 biological replicates, p-value from Tukey-test post-ANOVA analysis. **(f)** Click-it EdU labeling with propidium iodide (PI) labeling of cells to assess cell-cycle dynamics. Axes represent percent cells positive for stain compared to the parental gate detected by flow cytometry. **(g)** Senescence-associated beta-galactosidase images at 20x magnification. **(h)** Cd38 mRNA transcript levels in response to senescent macrophage conditions in wild-type and Cd38 KO macrophages. (i) NADase assay from whole cell lysates. NADase activity was measured by epsilon-NAD cleavage, with fluorescence intensity monitored over 1 hour. Traces reflect the average of N = 2 biological replicates. Average NADase activity was determined from the slope of the trace from 15 to 30 min. **(j)** Senescence-associated beta-galactosidase images at 20x magnification for WT and Cd38 ko senescent macrophages. **(k)** Mean, +/− SE, gene expression (RT-qPCR) normalized to control. N = 3 biological replicates, p-value from Tukey-test post-ANOVA analysis. Control means passage control. (l) Whole tissue staining of Senescence-associated beta-galactosidase images for young (3 m) and old (24 m) VAT tissue against wild-type and Cd38 KO backgrounds. **(m)** Mean, +/− SE, gene expression (RT-qPCR) normalized to control. N = 10 biological replicates, p-value from Tukey-test post-ANOVA analysis. Control means passage control.

(WT) (Extended Data Fig. 1j,k). Moreover, we did not observe any difference in SA-β-gal activity, senescent cell burden or inflammatory cytokine expression in visceral adipose tissue (VAT) from aged (24 months) WT versus *Cd38* KO mice, suggesting that targeting CD38 does not protect against the induction of senescence or the natural aging senescent cell burden (Extended Data Fig. 1l,m).

Aging bone marrow has been shown to acquire cell-intrinsic epigenetic modifications that affect macrophage polarization. Therefore, we next examined whether bone marrow age influences BMDM senescence. To test this, BMDMs from young and aged male mice were used in our Sen(IR) model. It was observed that the age of the bone marrow had no major influence in modulating the hallmark features of senescence (Extended Data Fig. 2a–c). Collectively, these data suggest that our macrophage senescence model is stable and reproducible, and that macrophage senescence cannot be prevented or reversed by T helper 2 cell signaling, LPS activation, CD38 NADase activity and the age of the bone marrow.



Extended data figure 2. (**a**) Senescence-associated β-galactosidase assay images of young and old BMDM senescent macrophages at 20x magnification. (**b**) Click-it EdU labeling of cells to assess the percentage of cells in S-phase. Bar graph quantification is an average of three

independent biological replicates. (**c**) Mean, +/− SE, gene expression (RT-qPCR) normalized to young control. N = 3 biological replicates, p-value from Tukey-test post-ANOVA analysis. P.Control means passage control.

5.2 Senescent macrophages upregulate the SASP and sterile type 1 interferon signaling

To identify the specific transcriptomic signature of senescent macrophages, we performed bulk RNA sequencing (RNA-seq). We found that both Sen(IR) and Sen(Doxo) macrophages share most of their transcriptomic phenotype (50%, 747 genes) (Fig. 2a,b and Extended Data Fig. 3a). Interestingly, the top upregulated genes are related to senescence, SASP and inflammation (Cdkn1a, Ccnd2, Ccr5, Cmpk2, Fn1, Mmp9, Mmp12, Mmp13, Pla2g7, Timp3, as well as interferon (IFN)-induced (Ifi) genes like Ifi44, Ifi209 and Ifi213) (Fig. 2c and Extended Data Fig. 3b). A set of downregulated genes was also identified that included Mki-67 and Cdkn2a (Fig. 2c and Extended Data Fig. 3b). Kyoto Encyclopedia of Genes and Genomes (KEGG) analysis revealed that senescence-related genes are associated with inflammation, whereas genes downregulated in senescence are linked to the cell cycle (Fig. 2d and Extended Data Fig. 3c). The occurrence of inflammation and IFN-signaling pathways led us to hypothesize that senescent macrophages also acquire a SASP. To test this, conditioned media were subjected to proteomics. Few secreted proteins differed between Sen(IR) and Sen(Doxo); however, both senescent conditions secreted markedly more SASP proteins than controls, with MMP12, APOE, LGALS3 and CMPK2 among the most abundant (Fig. 2e,f and Extended Data Fig. 3d). KEGG pathway enrichment also highlighted a signature related to inflammation and metabolism (Fig. 2g and Extended Data Fig. 3e) with 80% (293 proteins) of the total SASP proteome in common (Extended Data Fig. 3f). Both the transcriptome and SASP proteome analysis suggest senescent macrophages upregulate inflammatory pathways related to a type I IFN (Ifnα or Ifnβ) response

and undergo metabolic reprogramming suggesting an active response toward pathogens despite being in sterile conditions.

Sterile chronic inflammation related to macrophage-specific IFN responses has been observed in aging tissues and liver failure. The mechanisms underlying age-related type I IFN activation involve the cytosolic DNA-sensing pathway, cyclic GMP–AMP synthase-stimulator of interferon genes (cGAS-STING). To assess cGAS-STING signaling in senescent macrophages, cells were treated with the STING inhibitor (H-151). H-151 significantly reduced Ifnα and Ifnβ expression compared to DMSO controls (Fig. 2h). In addition, during senescence double-stranded DNA (dsDNA) re-localized from the mitochondria into the cytosol, suggesting mitochondrial DNA release as the source of cGAS-STING activation (Fig. 2i). To understand the mechanism, we interrogated the activity of CMPK2, a cytidine/uridine monophosphate kinase, that is upregulated in our omics datasets and a known regulator of inflammation via newly synthesized mtDNA (Fig. 2c,f). We found that *Cmpk2* gene and protein expression was associated with senescence and not an acute DNA damage response (Fig. 2j and Extended Data Fig. 3g). Therefore, we hypothesized that elevated CMPK2 activity in senescent macrophages may help drive activation of the type I IFN response. To test this, CRISPR–Cas9-based genome editing was used to disrupt the *Cmpk2* or *Rosa26* locus as a control (Fig. 2k). Sanger sequencing confirmed disruption leading to loss of CMPK2 protein expression, as validated by western blot (Fig. 2l,m). *Cmpk2*- and *Rosa26*-edited macrophages were subjected to senescence, which resulted in reduced total mitochondrial and cytosolic dsDNA as well as downregulated Ifnα and Ifnβ mRNA expression in the *Cmpk2*-edited senescent macrophages (Fig. 2n,o). Next, we performed RNA-seq on *Cmpk2*- and Rosa26-edited senescent macrophages. In senescent macrophages, *Cmpk2* loss reduced type I IFN-related genes (*Irf7*, *Acod1*, *Ifit206*) and decreased

enrichment of KEGG pathways such as Influenza A, NOD-like receptor signaling and Epstein–Barr virus infection (Fig. 2p,q). By contrast, genes involved in lipid metabolism were upregulated (Fig. 2p,r).

Based on the elevated IFN signaling observed in senescent macrophages, we hypothesized that they are primed toward a proinflammatory phenotype. To test this, we exposed senescent macrophages to LPS and observed a heightened gene expression response as well as an increased capacity for phagocytosis (Extended Data Fig. 3h,i). Conversely, the ability to clear apoptotic cells via efferocytosis was significantly reduced compared to control macrophages (Extended Data Fig. 3j). Upon IL-4 treatment, senescent macrophages increased expression of Cd36 and Ym1, but reduced expression of other hallmark M2 genes, along with diminished arginase-1 (Arg1) expression and enzymatic activity (Extended Data Fig. 3k,l). Therefore, our data demonstrated that senescent macrophages exhibit elevated IFN signaling, via activation of a CMPK2–mtDNA–cGAS-STING-dependent mechanism, and although they can still integrate both M1 and M2 polarization signals, they are biased toward a proinflammatory activation state.

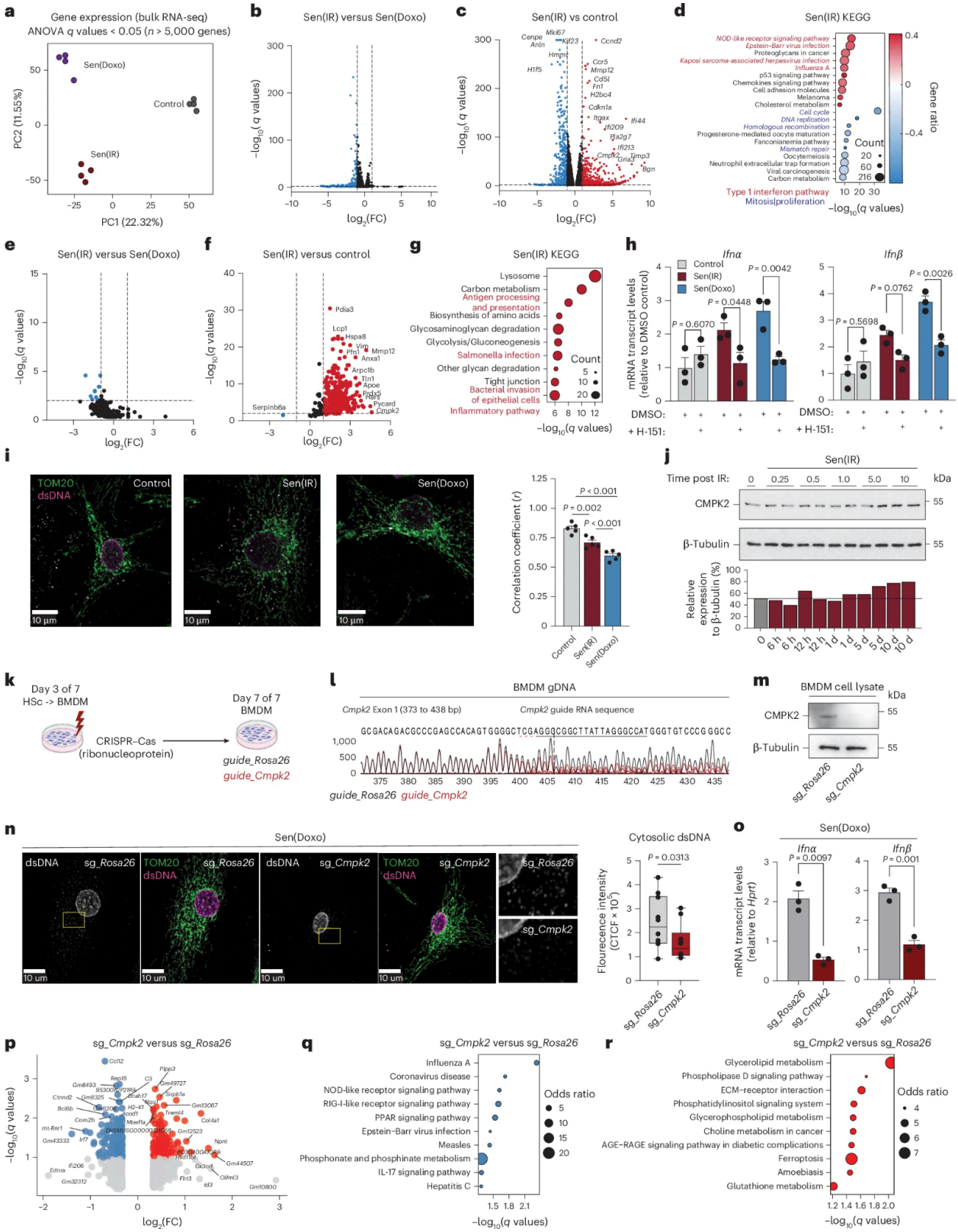
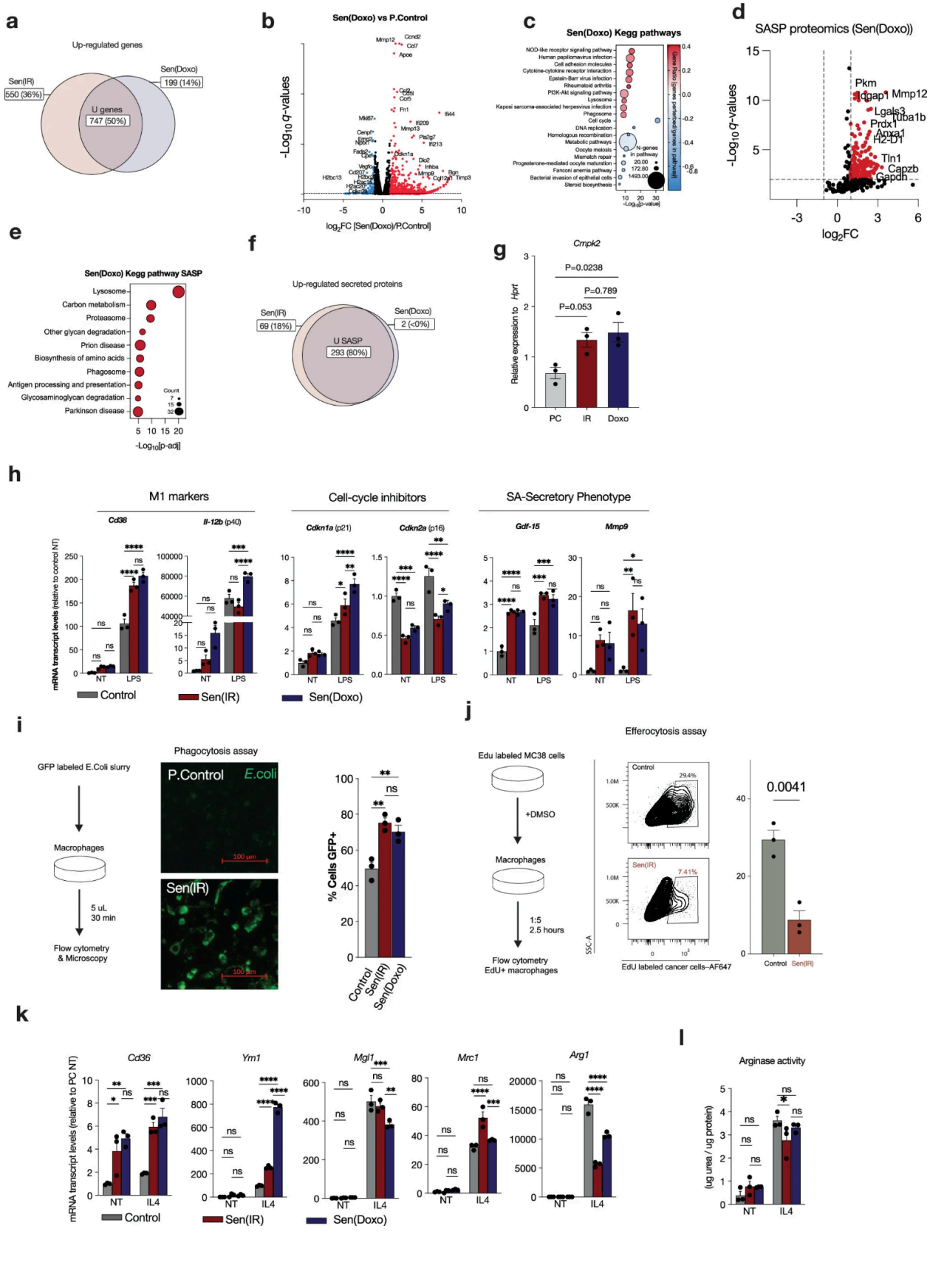

a
Gene expression (bulk RNA-seq)
ANOVA q values < 0.05 (n > 5,000 genes)
Sen(Doxo)
Control
Sen(IR)
PC2 (11.55%)
PC1 (22.32%)
b
Sen(IR) versus Sen(Doxo)
−log10(q values)
log2(FC)
c
Sen(IR) vs control
Cenpe
Mki67
Kif23
Ccnd2
Anln
Hmmr
H1f5
Ccr5
Mmp12
Cd5l
Fn1
H2bc4
Cdkn1a
Itgax
Ifi44
Ifi209
Rla2g7
Ifi213
Cmpk2
Gna3
Timp3
Bgn
d
Sen(IR) KEGG
NOD-like receptor signaling pathway
Epstein-Barr virus infection
Proteoglycans in cancer
Kaposi sarcoma-associated herpesvirus infection
Influenza A
p53 signaling pathway
Chemokines signaling pathway
Cell adhesion molecules
Melanoma
Cholesterol metabolism
Cell cycle
DNA replication
Homologous recombination
Progesterone-mediated oocyte maturation
Fanconianemia pathway
Mismatch repair
Oocytemeiosis
Neutrophil extracellular trap formation
Viral carcinogenesis
Carbon metabolism
Type 1 interferon pathway
Mitosis|proliferation
Count
Gene ratio
−log10(q values)
e
Sen(IR) versus Sen(Doxo)
f
Sen(IR) versus control
Pdia3
Lcp1
Hspa8
Vim
Ifitm1
Mmp12
Anxa1
Arpc1b
Tln1
Apoe
Rnf5
Pycard
Cmpk2
Serpinb6a
g
Sen(IR) KEGG
Lysosome
Carbon metabolism
Antigen processing and presentation
Biosynthesis of amino acids
Glycosaminoglycan degradation
Glycolysis/Gluconeogenesis
Salmonella infection
Other glycan degradation
Tight junction
Bacterial invasion of epithelial cells
Inflammatory pathway
Count
−log10(q values)
h
Ifnα
Ifnβ
Control
Sen(IR)
Sen(Doxo)
mRNA transcript levels (relative to DMSO control)
P = 0.6070
P = 0.0448
P = 0.0042
P = 0.5698
P = 0.0762
P = 0.0026
DMSO:
+ H-151:
i
TOM20
dsDNA
Control
Sen(IR)
Sen(Doxo)
10 μm
Correlation coefficient (r)
P < 0.001
P = 0.002
P < 0.001
j
Sen(IR)
Time post IR:
0
0.25
0.5
1.0
5.0
10
kDa
CMPK2
β-Tubulin
55
Relative expression to β-tubulin (%)
0 6 h 6 h 12 h 12 h 1 d 1 d 5 d 5 d 10 d 10 d
k
Day 3 of 7 HSc -> BMDM
Day 7 of 7 BMDM
CRISPR–Cas (ribonucleoprotein)
guide_Rosa26
guide_Cmpk2
l
BMDM gDNA
Cmpk2 Exon 1 (373 to 438 bp)
Cmpk2 guide RNA sequence
GCGACAGACGCCCGAGCCACAGTGGGGCTCGAGGGCGGCTTATTAGGGCCATGGGTGTCCCGGGCC
guide_Rosa26
guide_Cmpk2
m
BMDM cell lysate
kDa
CMPK2
β-Tubulin
55
sg_Rosa26
sg_Cmpk2
n
Sen(Doxo)
dsDNA
sg_Rosa26
TOM20
dsDNA
sg_Rosa26
dsDNA
sg_Cmpk2
TOM20
dsDNA
sg_Cmpk2
10 um
Cytosolic dsDNA
P = 0.0313
Flourecence intensity (CTCF × 10³)
o
Sen(Doxo)
Ifnα
Ifnβ
P = 0.0097
P = 0.001
mRNA transcript levels (relative to Hprt)
sg_Rosa26
sg_Cmpk2
p
sg_Cmpk2 versus sg_Rosa26
−log10(q values)
log2(FC)
q
sg_Cmpk2 versus sg_Rosa26
Influenza A
Coronavirus disease
NOD-like receptor signaling pathway
RIG-I-like receptor signaling pathway
PPAR signaling pathway
Epstein–Barr virus infection
Measles
Phosphonate and phosphinate metabolism
IL-17 signaling pathway
Hepatitis C
Odds ratio
−log10(q values)
r
sg_Cmpk2 versus sg_Rosa26
Glycerolipid metabolism
Phospholipase D signaling pathway
ECM–receptor interaction
Phosphatidylinositol signaling system
Glycerophospholipid metabolism
Choline metabolism in cancer
AGE–RAGE signaling pathway in diabetic complications
Ferroptosis
Amoebiasis
Glutathione metabolism
Odds ratio
−log10(q values)

Figure 2. **a**, PCA on bulk RNA-seq samples. **b**,**c**, Volcano plots of differentially expressed genes ($\log_2(\text{FC}) > 1.3$ and $\text{FDR} < 0.05$) between Sen(IR) versus Sen(Doxo) (**b**) and Sen(IR) versus control (**c**). Adjusted *P* values are derived from Fisher's exact test followed by FDR adjustment. **d**, KEGG terms associated with proteins upregulated or downregulated by both treatments. The red font highlights pathways related to a type I IFN signal. The blue font highlights terms related to the cell cycle. **e**,**f**, Volcano plot of upregulated (red) and downregulated (blue) proteins by FDR-adjusted *P* value and FC from SASP-proteomics mass spectrometry between Sen(IR) versus Sen(Doxo) (**e**) and between control and senescent macrophages (**f**). **g**, KEGG terms associated with the proteins upregulated or downregulated by both treatments. The red font highlights terms related to an inflammatory pathway. Adjusted *P* values are derived from Fisher's exact test followed by FDR adjustment. **h**, Mean ± s.e.m. mRNA transcript levels, relative to control, for type I IFN response genes in response to STING inhibitor (H-151). *P* value of ANOVA test of $n = 3$ biological replicates. **i**, Immunostaining for mitochondria (TOM20) and co-localized dsDNA (red). Average Pearson's correlation coefficients ± s.e.m. were calculated for $n = 5$ biological replicates. **j**, SDS–PAGE gel immunoblotting (western blot) of macrophages in response to days post IR. ImageJ quantification relative to loading controls are shown to the right. **k**, Illustration of CRISPR–Cas9 gene editing of differentiating hematopoietic stem cells into macrophages. **l**, Sanger sequencing base calling results from CRISPR–Cas9 editing of *CMPK2* locus exon 1. **m**, SDS–PAGE gels and immunostaining (western blot) for CMPK2 protein in response to edits sg_*Rosa*26 and sg_*Cmpk2* edits via CRISPR–Cas9. **n**, Immunostaining for mitochondria (TOM20) and co-localized dsDNA (red). To the right is the quantification of cytosolic dsDNA corrected total cell fluorescence (CTCF) intensity. Box-and-whisker plots show the median (center line), interquartile range (25th to 75th

percentiles; box), and minimum and maximum values (whiskers). $n = 10$ biological replicates, P values were calculated using a one-tailed t-test. **o**, Mean mRNA transcript levels ± s.e.m. relative to control of *Ifnα* and *Ifnβ* in Sen(Doxo) macrophages with edits on the *Rosa* or *Cmpk2* locus. $n = 3$ biological replicates were used to derive the P value of the t-test. **p**, Volcano plots of differentially expressed genes ($\log_2(FC) > 1.3$ and $FDR < 0.1$) between sg_*Rosa*26 and sg_*Cmpk2* edited Sen(Doxo) macrophages. Adjusted P values are derived from a two-sided t-test followed by FDR adjustment. **q**, KEGG pathway analysis on downregulated DEGs. Blue indicates downregulation. The size of the circles represents the odds ratio. Adjusted P values are derived from Fisher's exact test followed by FDR adjustment. **r**, KEGG pathway analysis on upregulated DEGs. Red indicates upregulation. The size of the circles represents the odds ratio. Adjusted P values are derived from Fisher's exact test followed by FDR adjustment.


a
Up-regulated genes
Sen(IR)
550 (36%)
Sen(Doxo)
199 (14%)
U genes
747 (50%)
b
Sen(Doxo) vs P.Control
-Log10 q-values
log2FC [Sen(Doxo)/P.Control]
c
Sen(Doxo) Kegg pathways
d
SASP proteomics (Sen(Doxo))
-Log10 q-values
log2FC
Pkm
Mmp12
Lgals3
Tuba1b
Prdx1
Anxa1
H2-D1
Tln1
Capzb
Gapdh
e
Sen(Doxo) Kegg pathway SASP
Lysosome
Carbon metabolism
Proteasome
Other glycan degradation
Prion disease
Biosynthesis of amino acids
Phagosome
Antigen processing and presentation
Glycosaminoglycan degradation
Parkinson disease
-Log10[p-adj]
f
Up-regulated secreted proteins
Sen(IR)
69 (18%)
Sen(Doxo)
2 (<0%)
U SASP
293 (80%)
g
Cmpk2
P=0.0238
P=0.789
P=0.053
Relative expression to Hprt
PC
IR
Doxo
h
M1 markers
Cell-cycle inhibitors
SA-Secretory Phenotype
Cd38
Il-12b (p40)
Cdkn1a (p21)
Cdkn2a (p16)
Gdf-15
Mmp9
mRNA transcript levels (relative to control NT)
NT
LPS
Control
Sen(IR)
Sen(Doxo)
i
Phagocytosis assay
GFP labeled E.Coli slurry
Macrophages
5 uL
30 min
Flow cytometry
& Microscopy
P.Control
E.coli
Sen(IR)
% Cells GFP+
Control
Sen(IR)
Sen(Doxo)
j
Efferocytosis assay
Edu labeled MC38 cells
+DMSO
Macrophages
1:5
2.5 hours
Flow cytometry
EdU+ macrophages
Control
29.4%
Sen(IR)
7.41%
SSC-A
EdU labeled cancer cells–AF647
0.0041
Control
Sen(IR)
k
Cd36
Ym1
Mgl1
Mrc1
Arg1
mRNA transcript levels (relative to PC NT)
NT
IL4
Control
Sen(IR)
Sen(Doxo)
l
Arginase activity
(ug urea / ug protein)
NT
IL4

Extended data figure 3. (**a**) Venn-diagram analysis of all upregulated genes across irradiation and doxorubicin-induced senescence models. (**b**)Volcano plots are differentially expressed ($log2FC > 1.3$ and $FDR < 0.05$) between control and senescent Sen(Doxo) macrophages. (**c**) Kegg terms associated with the genes up/down-regulated by both Sen(Doxo) macrophages compared to control macrophages. (**d**) Volcano plot of upregulated (red) and downregulated (blue) proteins by FDR adj p-value and fold change from SASP-proteomics (SASPomics) mass-spectrometry between control and Sen(Doxo) macrophages. (**e**) Kegg terms associated with the proteins up-regulated by Sen(Doxo) over control macrophages. (**f**) Venn-diagram analysis of all upregulated SASP proteins across irradiation and doxorubicin-induced senescence models. (**g**) Relative mRNA transcript levels of Cmpk2 across passage control, Sen(IR) and Sen(Doxo) macrophages. Asterisks represent the p-value of ANOVA ≥ 0.05 (ns), <0.05 (✱), <0.01 (✱✱), <0.001 (✱✱✱), <0.0001 (✱✱✱✱). (**h**) Relative mRNA transcript levels of M1 and senescent genes in response to LPS (24 hr 100 ng per mL) across P.Control, Sen(IR) and Sen(Doxo) macrophages. Asterisks represent the p-value of ANOVA ≥ 0.05 (ns), <0.05 (✱), <0.01 (✱✱), <0.001 (✱✱✱), <0.0001 (✱✱✱✱). (**i**) Phagocytosis assay using GFP-labeled E.Coli slurry. Images were taken at 40x magnification. Quantification of percent cells was performed using Image J software using 16-bit images. (**j**) Efferocytosis assay using apoptotic bodies derived from EdU-labeled MC38 cancer cells. Mean, +/− SE, EdU+ macrophages. N = 3 biological replicates, p-value from students t-test. (**k**) Relative mRNA transcript levels of M2 genes in response to IL-4 (24 hr 10 ng per mL) markers across P.Control, Sen(IR) and Sen(Doxo) macrophages. Asterisks represent the p-value of ANOVA ≥ 0.05 (ns), <0.05 (✱), <0.01 (✱✱), <0.001 (✱✱✱), <0.0001 (✱✱✱✱). (**l**) Arginase activity in cellular lysates as assessed by

urea production. Asterisks represent the p-value of post-hoc 2-way ANOVA ≥ 0.05 (ns), <0.05 (✱), <0.01 (✱✱), <0.001 (✱✱✱), <0.0001 (✱✱✱✱).

5.3 p21+ senescent macrophages accumulate in the aged liver

Next, we wanted to investigate whether macrophages naturally undergo senescence *in vivo* during the aging process. We focused on metabolic tissues, because these tissues acquired a high senescent cell burden during aging. In fact, our analysis showed that among visceral tissues, the liver showed the largest increase in *Cdkn1a* (p21) expression, while the heart and VAT showed smaller but significant increases (Fig. 3a). The aged liver and VAT also displayed elevated SA-β-gal activity and an increase in the amount of $p21^+$ F4/80+ macrophages relative to young liver and VAT (Extended Data Fig. 1l and Fig. 3b,c). Notably, *Cdkn2a* (p16) mRNA expression also increased across tissues tested, potentially reflecting inflammation or senescence in non-macrophage cell types (Extended Data Fig. 4a). To further investigate the relationship between p21 expression and increased SA-β-gal activity, we analyzed the Tabula Muris Senis dataset, which includes single-cell RNA-seq data from 23 tissues across the murine lifespan38. Interestingly, the liver also exhibited the greatest increase and highest proportion of $Cdkn1a^+$ cells with age (Fig. 3d,e). Based on these findings, we focused our analysis on the liver.

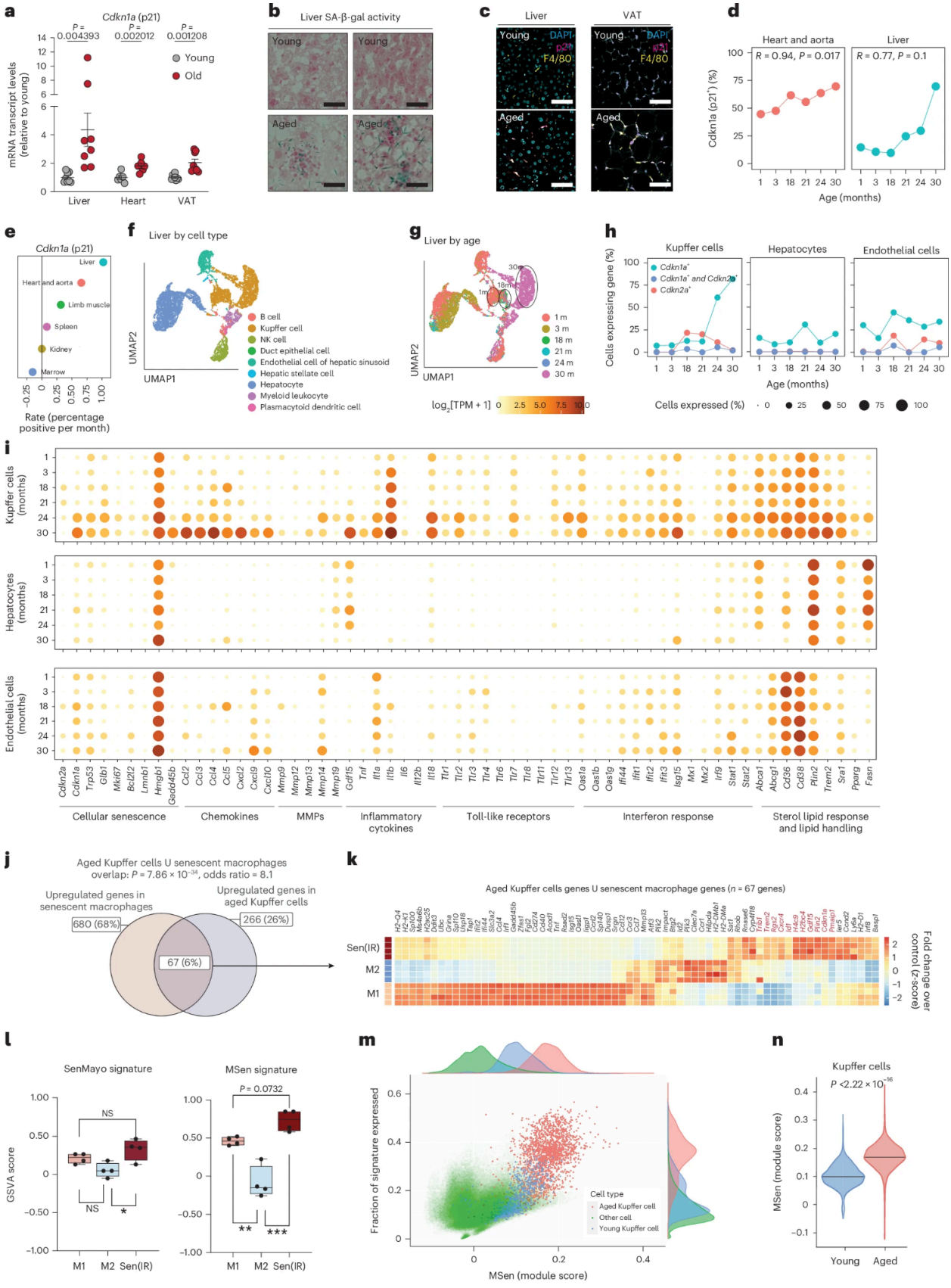

a
Cdkn1a (p21)
P = 0.004393
P = 0.002012
P = 0.001208
Young
Old
mRNA transcript levels (relative to young)
Liver
Heart
VAT
b
Liver SA-β-gal activity
Young
Aged
c
Liver
VAT
DAPI
p21
F4/80
d
Heart and aorta
Liver
R = 0.94, P = 0.017
R = 0.77, P = 0.1
Cdkn1a (p21+) (%)
Age (months)
e
Cdkn1a (p21)
Liver
Heart and aorta
Limb muscle
Spleen
Kidney
Marrow
Rate (percentage positive per month)
f
Liver by cell type
UMAP1
UMAP2
B cell
Kupffer cell
NK cell
Duct epithelial cell
Endothelial cell of hepatic sinusoid
Hepatic stellate cell
Hepatocyte
Myeloid leukocyte
Plasmacytoid dendritic cell
g
Liver by age
1 m
3 m
18 m
21 m
24 m
30 m
log2[TPM + 1]
h
Kupffer cells
Hepatocytes
Endothelial cells
Cdkn1a+
Cdkn1a+ and Cdkn2a+
Cdkn2a+
Cells expressing gene (%)
Age (months)
Cells expressed (%)
i
Kupffer cells (months)
Hepatocytes (months)
Endothelial cells (months)
Cdkn2a
Cdkn1a
Trp53
Glb1
Mki67
Bcl2l2
Lmnb1
Hmgb1
Gadd45b
Ccl2
Ccl3
Ccl4
Ccl5
Cxcl2
Cxcl9
Cxcl10
Mmp9
Mmp12
Mmp13
Mmp14
Mmp19
Gdf15
Tnf
Il1a
Il1b
Il6
Il12b
Il18
Tlr1
Tlr2
Tlr3
Tlr4
Tlr6
Tlr7
Tlr8
Tlr11
Tlr12
Tlr13
Oas1a
Oas1b
Oas1g
Ifi44
Ifit1
Ifit2
Ifit3
Isg15
Mx1
Mx2
Irf9
Stat1
Stat2
Abca1
Abcg1
Cd36
Cd38
Plin2
Trem2
Sra1
Pparg
Fasn
Cellular senescence
Chemokines
MMPs
Inflammatory cytokines
Toll-like receptors
Interferon response
Sterol lipid response and lipid handling
j
Aged Kupffer cells U senescent macrophages overlap: P = 7.86 × 10−34, odds ratio = 8.1
Upregulated genes in senescent macrophages
Upregulated genes in aged Kupffer cells
680 (68%)
266 (26%)
67 (6%)
k
Aged Kupffer cells genes U senescent macrophage genes (n = 67 genes)
Sen(IR)
M2
M1
Fold change over control (z-score)
l
SenMayo signature
MSen signature
P = 0.0732
GSVA score
NS
*
**
***
M1
M2
Sen(IR)
m
Fraction of signature expressed
MSen (module score)
Cell type
Aged Kupffer cell
Other cell
Young Kupffer cell
n
Kupffer cells
P <2.22 × 10−16
MSen (module score)
Young
Aged

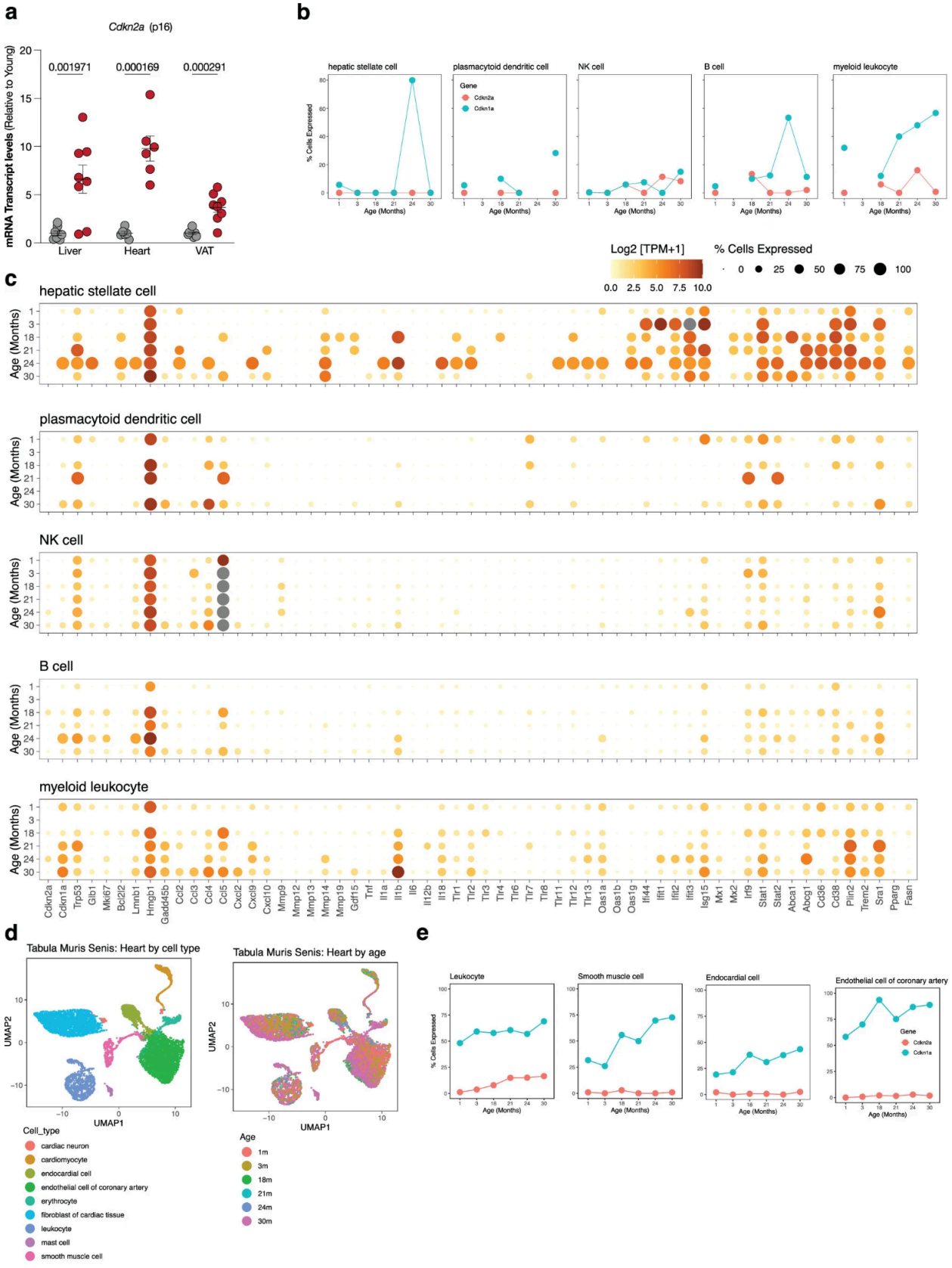
Figure 3. **a**, Mean ± s.e. mRNA transcript levels (RT–qPCR) of *Cdkn1a* from $n = 8$, 2–4-month-old (Y) versus $n = 8$ 21–24-month-old (O) male mice. *P* value derived from a two-sided *t*-test. **b**, SA-β-gal histology of Y and O liver sections. $n = 2$ male mice. Scale bars represent a 20 μm distance. **c**, Immunostaining for macrophages (F4/80) and p21 expression in Y and O male sections. Scale bar represents a 20 μm distance. **d**, Quantification of *Cdkn1a*$^+$ cell accumulation with age in heart and liver datasets. *P* values represent significance from Pearson's correlation test. **e**, Linear regression rates of tissue-specific *Cdkn1a*$^+$ cell accumulation with age across six tissues in the TMS database. **f**, UMAP analysis of the Tabula Muris Senis dataset representing all cells in the liver annotated by cell type. **g**, UMAP analysis of the Tabula Muris Senis dataset representing all cells in the liver annotated by age. **h**, Percentage of cells positive for *Cdkn1a* (green), *Cdkn2a* (red) and double positive (blue) across liver Kupffer cells, hepatocytes and endothelial cells. **i**, Bubble map of genes grouped by hallmarks or macrophage senescence. Size represents the fraction of cells expressing each gene, and color reflects average expression for endothelial cells, hepatocytes and Kupffer cells. **j**, Venn diagram analysis using Fisher's test with aged Kupffer cells and senescent IR macrophages. **k**, Bulk RNA-seq of 67 genes found enriched in senescence and aging. Conditions reflect different polarized states. Box outlines are manually placed, and highlighted clusters are generally downregulated compared to other conditions. The *z*-score reflects the FC of the condition over the control group. **l**, GSVA scoring of M1, M2 and Sen(IR) conditions using the SenMayo gene signature and the 67 genes identified in **j** as the MSen signature. Box-and-whisker plots display the median (center line), interquartile range (25th to 75th percentiles; box), and minimum and maximum values (whiskers). $n = 4$ biological replicates were analyzed. *P* values reflect post-hoc comparisons following one-way ANOVA. NS, not significant ($P \geq 0.05$); *$P < 0.05$; **$P < 0.001$;

***$P < 0.001$. **m**, Distribution of cells expressing the MSen signature across all cell types in the Tabula Muris Senis dataset via a Seurat score. **n**, Distribution of MSen Seurat score across young and old Kupffer cells. *P* value represents results of a Student's *t*-test. m, month; NK, natural killer.

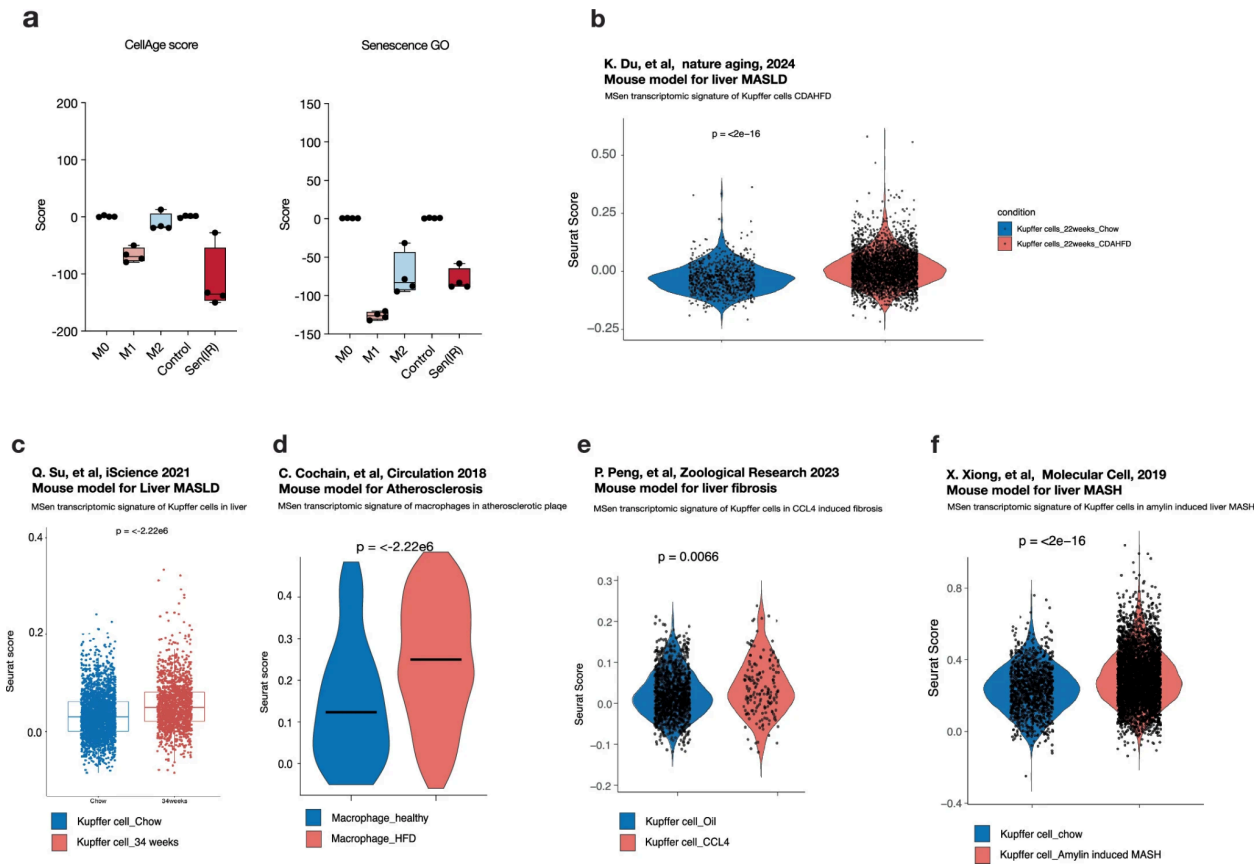
Kupffer cells, resident macrophages in the liver, are the most abundant hepatic immune cell population and our analysis revealed that the transcriptomic profile of Kupffer cells undergoes profound aging-dependent changes (Fig. 3f,g). Unlike other liver cell types, such as hepatocytes, endothelial cells and other immune cell populations, Kupffer cells exhibited marked age-dependent upregulation of Cdkn1a expression (Fig. 3h and Extended Data Fig. 4b). We next explored the expression of key senescence-associated genes, including chemokines, matrix metalloproteinases (MMPs), IFN and lipid-handling genes, across all major liver cell types. Notably, among these populations, only Kupffer cells were consistently enriched for hallmark senescence genes with age, including a pronounced inflammaging signature (Fig. 3i and Extended Data Fig. 4c). By contrast, in aged cardiac tissue a similar pattern was observed in the myeloid leukocyte population, although increased Cdkn1a expression was not limited exclusively to myeloid cells (Extended Data Fig. 4d,e).

Comparative transcriptomic analysis of aged Kupffer cells and in vitro Sen(IR) and Sen(Doxo) macrophages identified 67 commonly expressed genes, defining a macrophage senescence (MSen) signature (Fig. 3j). While containing M1 and M2 genes, the set also includes senescence-specific genes that may distinguish senescent macrophages from other subsets (Fig. 3k). Using Gene Set Variation Analysis (GSVA), the MSen transcriptomic signature identified senescent macrophages among M1 and M2 macrophages in a manner that outperformed the SenMayo, CellAge and Senescence Gene Ontology signatures (Fig. 3l and Extended Data Fig.

5a). The same MSen signature was applied across all cell populations and tissues in the Tabula Muris Senis and was highly selective for identifying aged, but not young, Kupffer cells, or other cell types (Fig. 3m,n). Collectively, the data indicate that tissue-resident macrophages, Kupffer cells, represent a major pool of senescent cells in aged livers and possibly other metabolic tissues.


a
Cdkn2a (p16)
mRNA Transcript levels (Relative to Young)
0.001971
0.000169
0.000291
Liver
Heart
VAT
b
hepatic stellate cell
plasmacytoid dendritic cell
NK cell
B cell
myeloid leukocyte
% Cells Expressed
Age (Months)
Gene
Cdkn2a
Cdkn1a
Log2 [TPM+1]
% Cells Expressed
c
hepatic stellate cell
plasmacytoid dendritic cell
NK cell
B cell
myeloid leukocyte
Age (Months)
Cdkn2a
Cdkn1a
Trp53
Glb1
Mki67
Bcl2l2
Lmnb1
Hmgb1
Gadd45b
Ccl2
Ccl3
Ccl4
Ccl5
Cxcl2
Cxcl9
Cxcl10
Mmp9
Mmp12
Mmp13
Mmp14
Mmp19
Gdf15
Tnf
Il1a
Il1b
Il6
Il12b
Il18
Tlr1
Tlr2
Tlr3
Tlr4
Tlr6
Tlr7
Tlr8
Tlr11
Tlr12
Tlr13
Oas1a
Oas1b
Oas1g
Ifi44
Ifit1
Ifit2
Ifit3
Isg15
Mx1
Mx2
Irf9
Stat1
Stat2
Abca1
Abcg1
Cd36
Cd38
Plin2
Trem2
Sra1
Pparg
Fasn
d
Tabula Muris Senis: Heart by cell type
Tabula Muris Senis: Heart by age
UMAP1
UMAP2
Cell_type
cardiac neuron
cardiomyocyte
endocardial cell
endothelial cell of coronary artery
erythrocyte
fibroblast of cardiac tissue
leukocyte
mast cell
smooth muscle cell
Age
1m
3m
18m
21m
24m
30m
e
Leukocyte
Smooth muscle cell
Endocardial cell
Endothelial cell of coronary artery
% Cells Expressed
Age (Months)
Gene
Cdkn2a
Cdkn1a

Extended data figure 4. (**a**) Mean, and +/− SE, gene expression (RT-qPCR) of Cdkn2a from N = 5, 2–4 month young (Y) vs. 21–24-month-old (O) mice. Asterisks represent the p-value of t-test ≥0.05 (ns), <0.05 (✱), <0.01 (✱✱), <0.001 (✱✱✱), <0.0001 (✱✱✱✱). (**b**) The percent cell is positive for Cdkn1a (blue) and Cdkn2a (red) across the remainder of liver cells across age. (**c**) Bubble map of genes grouped by hallmarks or macrophage senescence. Size represents the fraction of cells expressing each gene, and color reflects average expression for the remainder of liver cells. (**d**) UMAP analysis of the Tabula Muris Senis data set representing all cells in the liver annotated by cell type. UMAP analysis of the Tabula Muris Senis data set representing all cells in the liver annotated by age. (**e**) The percent cell is positive for Cdkn1a (blue) and Cdkn2a (red) across all cells in the heart and aorta data set.



Extended data figure 5. (**a**) GSVA scoring on M1, M2, Sen(IR), and control conditions of CellAge, gene ontology (GO) for senescence from the gene ontology database. (**b-f**) Median difference in the distribution of MSen Seurat score across all macrophages in MASLD liver disease and atherosclerosis. P-value represents results of a t-test. Included is the distribution of scores (x-axis) across all cells in data sets compared to the proportion of genes expressed in MSen signature (y-axis).

5.4 Senescent macrophages form lipid droplets and express TREM2

To understand the physiological mechanisms driving macrophage senescence during aging, we analyzed transcriptomic and proteomic datasets from aged Kupffer cells and in vitro senescent macrophages. Both populations showed increased expression of genes involved in cholesterol metabolism, along with elevated levels of markers characteristic of lipid-laden, disease-associated macrophages, including *Trem2* and *Plin2* (Figs. 2d and 3i,k). These findings led us to hypothesize that senescent macrophages constitute a subset of lipid-laden macrophages implicated in metabolic diseases, including MASLD and atherosclerosis. To evaluate this, we analyzed five public datasets and observed a significant upregulation of the MSen gene signature in Kupffer cells from MASLD livers and in atherosclerotic plaques (Extended Data Fig. 5b–f). Furthermore, deep proteomic analysis revealed that senescent macrophages upregulate several proteins related to M2 (cluster 1), M1 (cluster 2) and exclusively in the C3 cluster (Fig. 4a). Investigation into the clusters reveals the upregulation of lipid-related proteins compared to control and M1 conditions (Fig. 4b). Pathway enrichment into the C3 cluster highlights lipid remodeling terms with 26.7% of proteins perturbed (Fig. 4c). Consistent with this, we found that senescent macrophages exhibited greater lipid droplet accumulation compared to control macrophages (Fig. 4d,e).

TREM2 macrophages have been implicated in several diseases like metabolic dysfunction, chronic inflammation and tissue degeneration, including metabolic dysfunction-associated steatohepatitis (MASH) and neurodegenerative diseases such as Alzheimer disease. Interestingly, TREM2 is highly upregulated in Sen(IR) macrophages compared to M0, M1 and M2 macrophages, with glycosylated TREM2 suggesting membrane localization (Fig. 4f). In addition, we observed that the simultaneous activation of *Trem2*, p16 and p21 is associated with M2 anti-inflammatory macrophages, whereas the upregulation of p21, TREM2, and downregulation of p16 is a unique signature of senescent macrophages (Fig. 4f). Furthermore, *Trem2*−/− senescent macrophages had reduced p21 expression, suggesting that TREM2 plays an active role in regulating senescence (Fig. 4f).

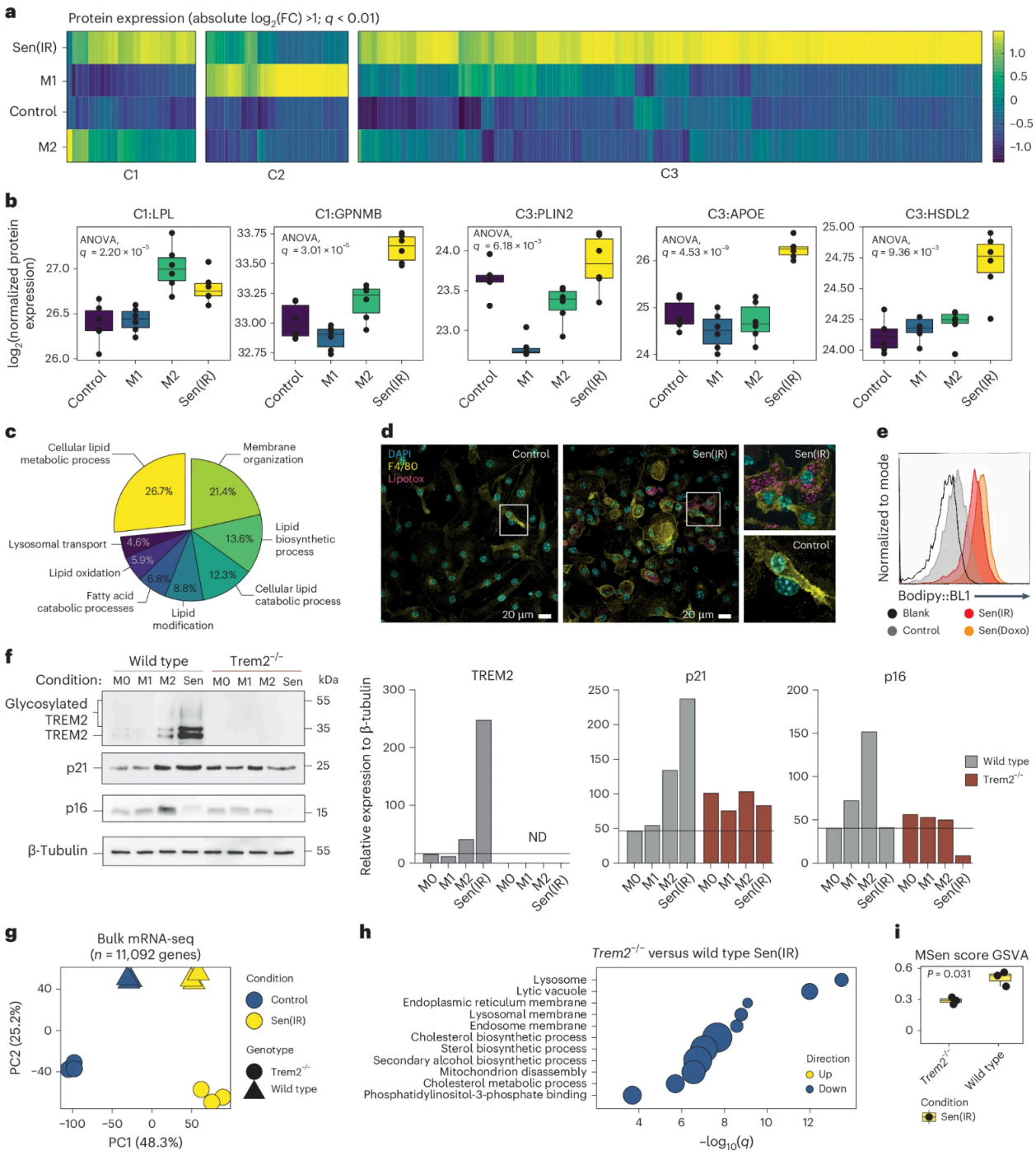
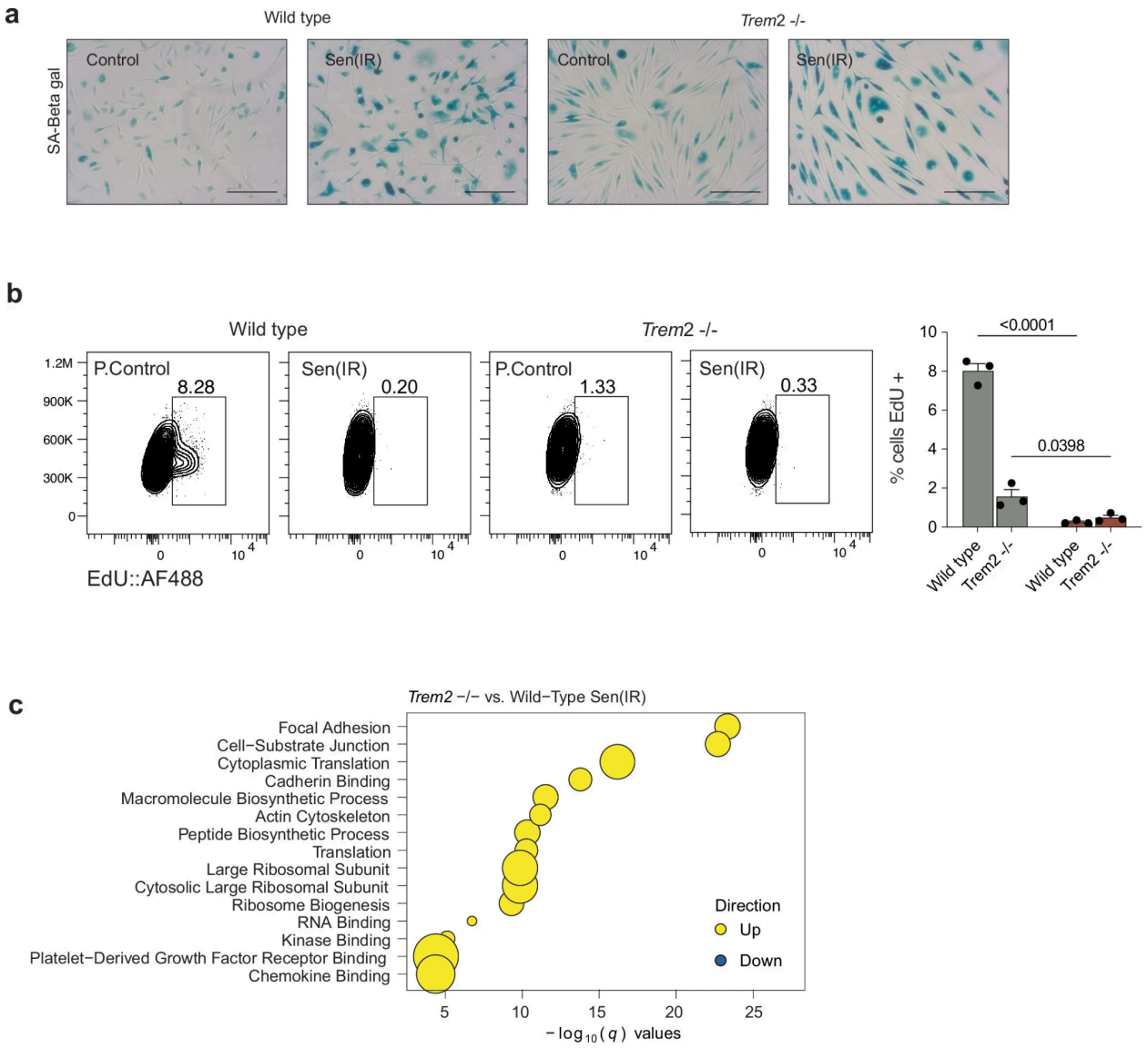

a
Protein expression (absolute log2(FC) >1; q < 0.01)
Sen(IR)
M1
Control
M2
C1
C2
C3
1.0
0.5
0
−0.5
−1.0
b
C1:LPL
C1:GPNMB
C3:PLIN2
C3:APOE
C3:HSDL2
log2(normalized protein expression)
ANOVA, q = 2.20 × 10−5
ANOVA, q = 3.01 × 10−5
ANOVA, q = 6.18 × 10−3
ANOVA, q = 4.53 × 10−9
ANOVA, q = 9.36 × 10−3
Control
M1
M2
Sen(IR)
c
Cellular lipid metabolic process
Membrane organization
Lipid biosynthetic process
Cellular lipid catabolic process
Lipid modification
Fatty acid catabolic processes
Lipid oxidation
Lysosomal transport
26.7%
21.4%
13.6%
12.3%
8.8%
6.8%
5.9%
4.6%
d
DAPI
F4/80
Lipotox
Control
Sen(IR)
20 µm
e
Normalized to mode
Bodipy::BL1
Blank
Control
Sen(IR)
Sen(Doxo)
f
Wild type
Trem2−/−
Condition:
M0 M1 M2 Sen
kDa
Glycosylated TREM2
TREM2
p21
p16
β-Tubulin
55
35
25
15
55
TREM2
p21
p16
Relative expression to β-tubulin
ND
Wild type
Trem2−/−
g
Bulk mRNA-seq
(n = 11,092 genes)
PC2 (25.2%)
PC1 (48.3%)
Condition
Control
Sen(IR)
Genotype
Trem2−/−
Wild type
h
Trem2−/− versus wild type Sen(IR)
Lysosome
Lytic vacuole
Endoplasmic reticulum membrane
Lysosomal membrane
Endosome membrane
Cholesterol biosynthetic process
Sterol biosynthetic process
Secondary alcohol biosynthetic process
Mitochondrion disassembly
Cholesterol metabolic process
Phosphatidylinositol-3-phosphate binding
Direction
Up
Down
−log10(q)
i
MSen score GSVA
P = 0.031
Trem2−/−
Wild type
Condition
Sen(IR)
j
MSen signature
Sen(IR) wild type
Sen(IR) Trem2−/−
Rgs2 Atf3 Gadd45b Hilpda Plk2 Mmp13 Ccr3 Dusp1 Trem2 Clec7a Plin2 H2bc4 Cd274 Rsad2 Ifit2 Irf8 Cdkn1a Cd40 Isg15 Usp18
Cyp4f18 Srgn Plk3 Fgl2 Gdf15 Slc3a2 Id2 Sat1 Ccrl2 Impact Grina Cxcr4 H4c9
Ccl4 Zfas1 Ubc Ier5 Tap1 Pmaip1 Trib1 Basp1 H2-DMa Ccr1 Sp100 H2-Q4
Ddit3 H2-D1 H2-K1 H2-DMb1 Rhob Sp140 Id1 Ccnd2 Tnf Ccl7 Ccl12 Acod1 Ms4a6b Btg2 Sp110 Irf1

Figure 4. a, Protein expression (LC–MS/MS) projected as a *z*-score of $\log_2$(FC) over control conditions. Clustering represents the three major clades of a dendrogram. **b**, $\log_2$-transformed raw protein expression for selected lipid-laden proteins. Box-and-whisker plots display the median (center line), interquartile range (25th to 75th percentiles; box), and minimum and maximum values (whiskers). $n = 6$ biological replicates were analyzed. Statistical *P* values reflect results from a one-way ANOVA identifying differences in at least one group. **c**, KEGG pathway enrichment for all proteins upregulated in Sen(IR) conditions over control macrophages. **d**, Immunostaining by microscopy for lipid-body labeling (green-LipoTOX) in Sen(IR) conditions. Green arrows represent LipoTOX+ cells. **e**, Bodipy (lipid droplet) staining for represented conditions. Total histograms are normalized to mode. **f**, SDS–PAGE gels and immunoblotting (western blot) for TREM2 (both glycosylated and total), p21 and p16. ImageJ quantification for band intensity is shown to the right and represents relative intensity over the loading control. **g**, PCA on bulk RNA-seq samples from senescent macrophages (Sen(IR) (10 days post irradiation)) and passage control condition (Control) on a WT or *Trem2*$^{-/-}$ background. **h**, Gene Ontology analysis for statistically significant downregulated DEGs in senescence in response to the *Trem2*$^{-/-}$ background. The size of the data points represents the relative odds ratio. **i**, MSen scoring of bulk RNA-seq samples using GSVA methods. Box-and-whisker plots display the median (center line), interquartile range (25th to 75th percentiles; box), and minimum and maximum values (whiskers). $n = 3$ biological replicates were analyzed. *P* values represent results from Student's *t*-test. **j**, Scaled transcriptomic expression of the 67 MSen genes broken into the four major clades of a dendrogram.

To determine the functional role of TREM2, *Trem2*−/− mice were used to evaluate hallmark features of senescence. SA-β-gal activity and cell-cycle arrest phenotypes were unchanged in response to the loss of TREM2 (Extended Data Fig. 6a,b), but a profound change in morphology was observed, and proliferation rates were also attenuated in the Trem2−/− background (Extended Data Fig. 6b). Efferocytosis was reduced in WT senescent macrophages, consistent with reports that TREM2 shedding impairs TREM2-dependent efferocytosis in chronically activated macrophages48 (Extended Data Fig. 3j). To define the global impact of TREM2 on macrophage senescence, we performed unbiased transcriptomic analysis. Principal components analysis (PCA) revealed distinct clustering across all conditions, with the first principal component (PC1) separating control and senescent cells and the second principal component (PC2) reflecting genotype differences (Fig. 4g). Pathway analysis of downregulated genes in *Trem2*−/− senescent macrophages highlighted autophagy-related cellular compartments and cholesterol metabolism, while upregulated genes were enriched for focal adhesion, translation and actin cytoskeleton remodeling (Fig. 4h and Extended Data Fig. 6c). We next asked whether Trem2 regulates the MSen transcriptomic signature developed in Fig. 3k. Interestingly, the loss of TREM2 downregulates the MSen gene score and prevents the expression of key MSen-related genes, including *Cdkn1a*, p21 (Fig. 4i,j). Collectively, these data suggest that TREM2 plays a key role in regulating p21, SASP gene expression and lipid biology in senescent macrophages.



Extended data figure 6. (**a**) Senescence-associated β-galactosidase assay imaging for wild-type and *Trem2* –/– senescent macrophages at 20x magnification. Scale bars represent 20-micron distances. (**b**) Click-it EdU labeling of cells to assess % cells in S-phase. Bar graph quantification is an average of three independent biological replicates. N = 3 biological replicates, p-value from Tukey-test post-ANOVA analysis. (**c**) Gene ontology analysis for statistically significant upregulated DEGs within senescence in response to the *Trem2* –/– background. The size of the data points represents the relative odds ratio.

5.5 Excess Ac-LDL drives of macrophage senescence in vitro

To characterize the lipid species in senescent macrophages, we performed shotgun lipidomics and identified ceramides (Cer d18:0 and Cer d18:1) and cholesterol esters to be enriched in senescence as well as a subtle downregulation of hexosylceramides (Fig. 5a). In addition, the composition of fatty acids represents polyunsaturated fatty acids in senescence (Fig. 5b). Cholesterol was found to be esterified to the bulk of the polyunsaturated fatty acid pool with arachidonic acid (20:4) and dihomo-γ-linolenic acid (20:3), bioactive fatty acids implicated in cellular senescence and the SASP, being the highest ranked compared to other lipid species50 (Fig. 5c). The accumulation of cholesterol esters and lipid droplets suggests that senescent macrophages adopt a lipid-laden, foam cell-like phenotype that may contribute to chronic inflammation, metabolic dysfunction and tissue degeneration in aging and disease.

High serum levels of low-density lipoprotein (LDL) cholesterol is a major risk factor for metabolic disease and is known to increase intracellular cholesterol levels in macrophages. We hypothesized that excess cholesterol loading via LDL could serve as a driver of macrophage senescence *in vitro* (Fig. 5d). To test this, macrophages were treated with an acetylated form of LDL (Ac-LDL) which bypasses the LDL receptor, providing a pharmacological method to rapidly load macrophages with cholesterol (Fig. 5e). In response to Ac-LDL, we observed a time-dependent increase in TREM2 and p21 expression, while p16 was modestly decreased (Fig. 5f). Increased SA-β-gal activity and reduced cell proliferation were also observed during prolonged Ac-LDL exposure (Fig. 5g,h). To quantify changes in gene expression in response to Ac-LDL, macrophages were treated with four independent batches of Ac-LDL to embrace the natural variability of commercialized LDL. Under high-cholesterol conditions, both Cdkn1a (p21) and Trem2 were upregulated, whereas *Cdkn2a* (p16) did not vary significantly (Fig. 5i).

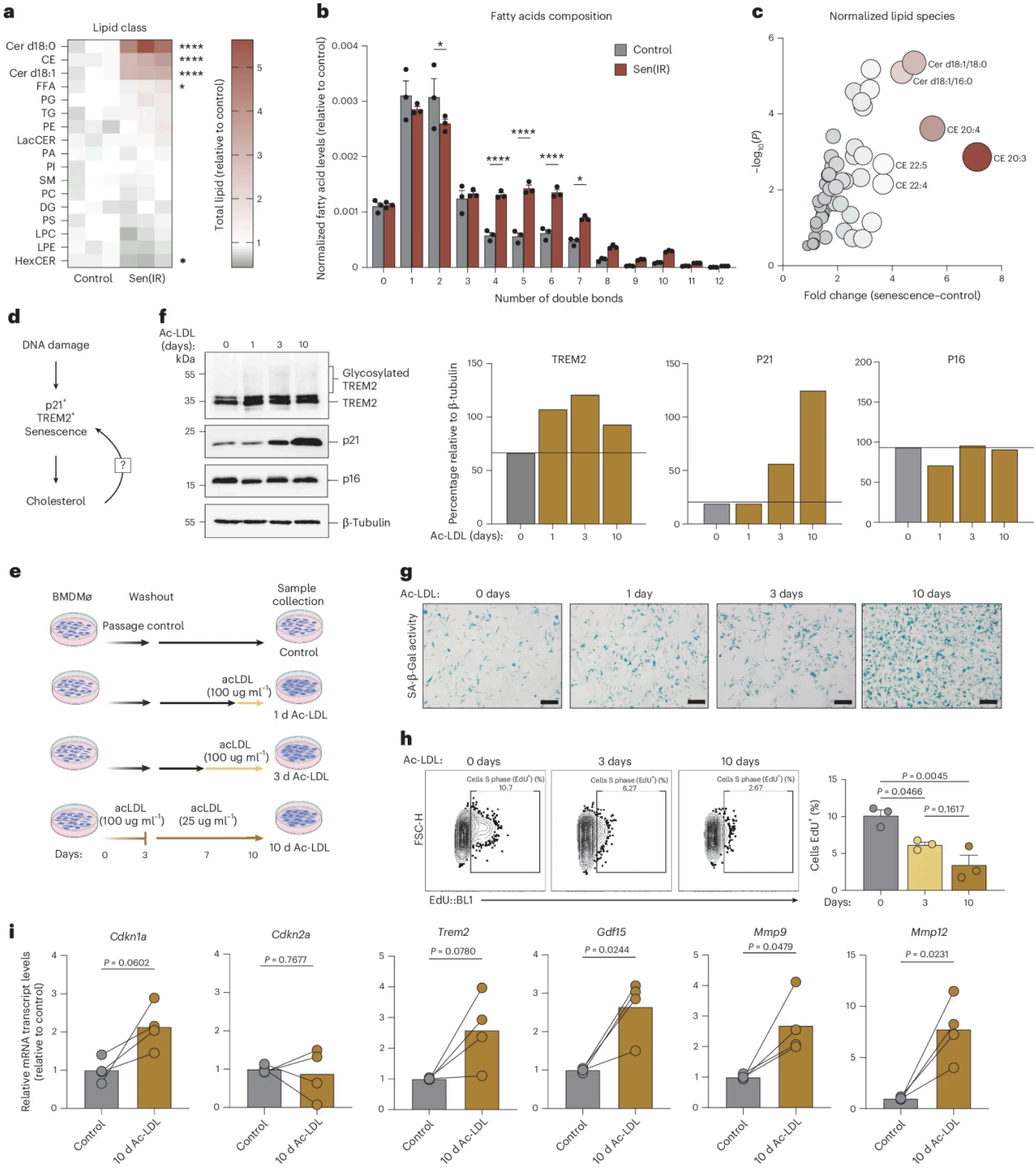


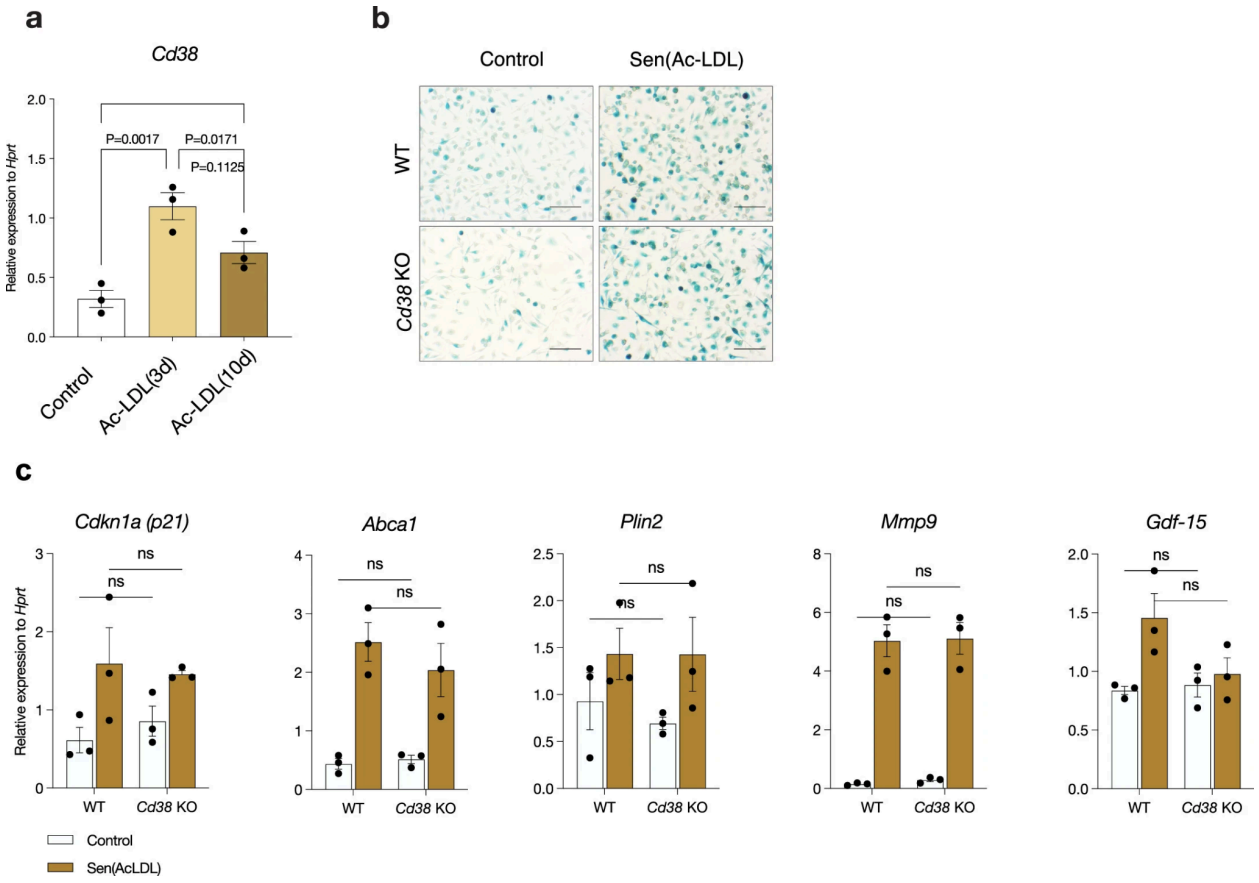
Figure 5. a, Heatmap representation of fold change differences of normalized lipid abundance (nmol lipid per 1×10^6 cells per average cell size) for all lipid species via shotgun lipidomics (LC–MS/MS) in Sen(IR) macrophages relative to control macrophages. Asterisks represent the *P* value of the ANOVA: ns, ≥0.05; $*P < 0.05$; $**P < 0.01$; $***P < 0.001$; $****P < 0.0001$. **b**,

Normalized fatty acid levels (nmol fatty acid per 1×10^6 cells per average cell size) relative to control macrophages via shotgun lipidomics (LC–MS/MS). Bar: average ± s.e.m. of $n = 3$ biological replicates. Asterisks represent the P value of the t-test: ns, ≥ 0.05; $*P < 0.05$; $**P < 0.01$; $***P < 0.001$; $****P < 0.0001$. **c**, Volcano plot of the most enriched lipid species in senescence relative to control macrophages. The color and size of the data points represent the FC gradient. **d**, Model illustration hypothesizing cholesterol as a driver of macrophage senescence. **e**, Model illustration of an in vitro model system of Ac-LDL-induced macrophage senescence. **f**, SDS–PAGE gels and immunostaining (western blot) for TREM2 (both glycosylated and total), p21 and p16 in response to more time in Ac-LDL. ImageJ quantification for band intensity is shown to the right and represents the relative intensity over the loading control. **g**, SA-β-gal assay imaging at ×20 magnification. Scale bar: 10 μm. **h**, Click-iT EdU labeling of Ac-LDL-treated cells to assess cell-cycle dynamics. The average ± s.e.m. cell fraction in S phase (EdU^+) is shown to the right. P value derived from an ANOVA. $n = 3$ biological replicates were used. **i**, Mean ± s.e.m. mRNA transcript levels relative to control for hallmark senescence genes. P value of paired t-tests from $n = 4$ biological independent experiments. BMDMø, bone marrow-derived macrophage.

In addition, we observed selective upregulation of SASP genes such as *Gdf15*, *Mmp9* and *Mmp12* (Fig. 5i). Collectively, these results demonstrate that cholesterol ester loading promotes a senescent, foam cell-like macrophage phenotype characterized by lipid accumulation and SASP activation.

It has recently been proposed that cholesterol accumulation, resulting from genetic deletion of the cholesterol efflux ATP-binding cassette, ABCA1, drives senescence through a

mechanism involving CD38 activation and NAD^+ decline. CD38 expression was also increased during DNA damage-induced senescence (Fig. 1i), and a senescence-associated decline in NAD^+ levels is a well-known feature of aging. Furthermore, Cd38 mRNA was elevated during acute exposure to Ac-LDL and remained modestly elevated during later stages of senescence (Extended Data Fig. 7a). These findings suggest that cholesterol may contribute to macrophage senescence, at least in part, through a CD38-dependent mechanism. However, as we discussed earlier, our data suggest CD38 is not required for DNA damage and natural aging-induced senescence (Fig. 1i and Extended Data Fig. 1k–m). To test the role of CD38 in cholesterol-driven macrophage senescence, *Cd38* KO mice were subjected to Ac-LDL loading. Across multiple assays, no significant differences in senescence gene expression (*Cdkn1a, Mmp9, Gdf15*), cholesterol sensing (*Abca1*) or SA-β-gal activity were observed compared to WT macrophages, suggesting CD38 is not necessary for cholesterol-induced senescence (Extended Data Fig. 7b,c), consistent with our earlier results.



Extended data figure 7. (**a**) Relative *Cd38* mRNA transcript levels across control, 3 days acLDL (foamy) and 10 days acLDL (sen). Asterisks represent the p-value of ANOVA ≥ 0.05 (ns), <0.05 (✱), <0.01 (✱✱), <0.001 (✱✱✱), <0.0001 (✱✱✱✱). (**b**) Senescence associated beta galactosidase assay imaging for Cd38 –/– macrophages compared to WT control at 20 x magnification. Scale bars represent 10 um. (**c**) Relative mRNA transcript levels for senescence and SASP genes across control and 10 days Ac-LDL (sen) for WT and Cd38 –/– genotypes. Asterisks represent the p-value of ANOVA ≥ 0.05 (ns), <0.05 (✱), <0.01 (✱✱), <0.001 (✱✱✱), <0.0001 (✱✱✱✱).

5.6 ABT-263 efficiently and selectively targets senescent macrophages for apoptosis

We next hypothesized that Ac-LDL-induced senescent macrophages can contribute to diseases associated with hypercholesterolemia. To target these cells for apoptosis, we investigated a panel of pro- and anti-apoptotic genes and identified *Bcl-2*, a key gene involved in anti-apoptotic pathways, as well as pro-apoptotic mitochondrial genes such as Bak1 and Bax (Fig. 6a). BCL-2 is a direct inhibitor of mitochondrial BAX and BAK proteins and given this pattern in transcription, it was hypothesized that pharmacological inhibition of BCL-2 should allow mitochondrial BAX or BAK to drive apoptosis (Fig. 6b). To test this hypothesis, we used the known senolytics ABT-263 (Navitoclax), a BCL family inhibitor, and Dasatinib and Quercetin (D + Q). Selective elimination of senescent macrophages was observed in response to ABT-263, unlike D + Q, which induced cytotoxicity in both senescent and nonsenescent cells (Extended Data Fig. 8a,b). A dose- and time-dependent apoptotic effect was also observed with ABT-263, with a half maximal inhibitory concentration (IC50) value in the nanomolar range (Fig. 6c,d and Extended Data Fig. 8c). Next, we asked how effective ABT-263 is at targeting macrophage senescence across various polarized states. To test this, we treated M1 and M2 macrophages with ABT-263, along with Ac-LDL-induced senescent macrophages. After a 24-h exposure to ABT-263, apoptosis was only observed in senescent conditions, suggesting that ABT-263 is selective and effective at killing senescent macrophages, and not generally activated pro- or anti-inflammatory macrophages (Fig. 6e).

To assess the effects of ABT-263 on $p21^{+}$ senescent macrophages in vivo, young and aged mice were treated by oral gavage using an intermittent ‘hit-and-run’ dosing strategy (Fig. 6f). The liver, VAT and spleen were collected to determine the effect of senescent macrophage clearance on systemic inflammation and MASLD. Using immunofluorescence microscopy, the

number of p21+ and F4/80+ macrophages in the liver increased from ~5% to ~50% during aging and was significantly reduced to ~10% in response to ABT-263 (Fig. 6g,h). Interestingly macrophages represent 60%–80% of p21+ cells in young and aged livers (Extended Data Fig. 8d). Systemically, it was observed that the relative spleen weight was decreased, suggesting repression of splenomegaly and systemic inflammation (Fig. 6i). Lower SA-β-gal activity in the

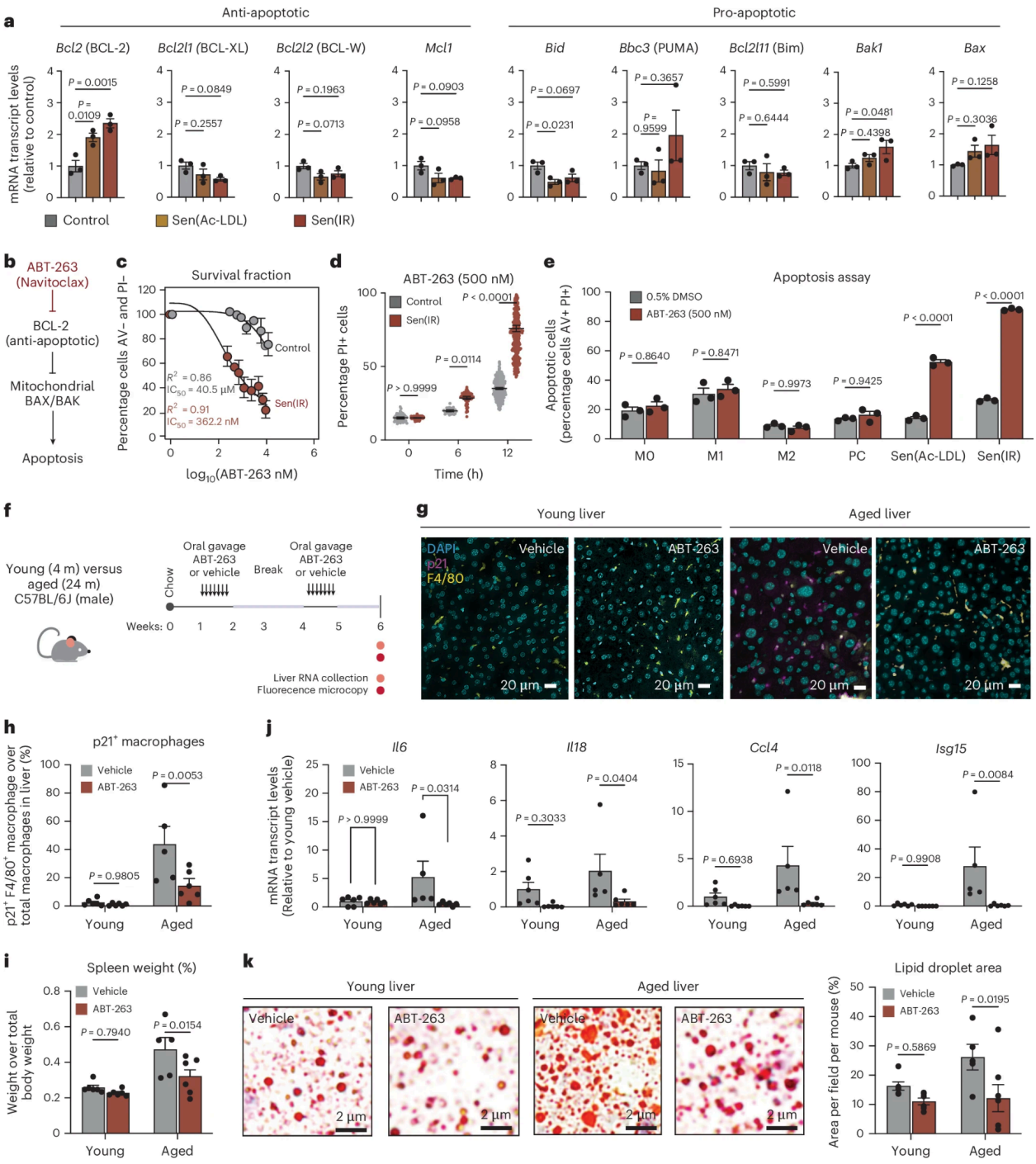
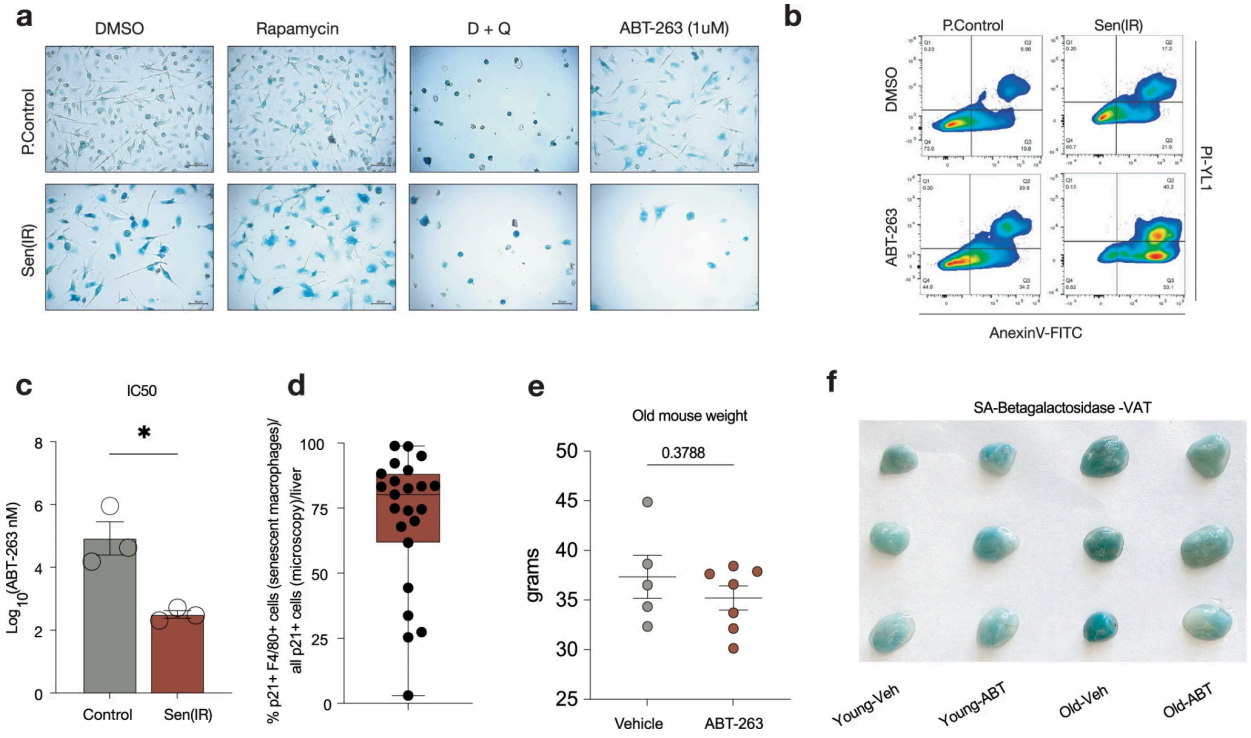


Figure 6. **a**, Average ± s.e.m. mRNA transcript levels (RT–qPCR) for a collection of pro- and anti-apoptotic genes relative to control. *P* value derived from an ANOVA test. $n = 3$ biological replicates. **b**, Model illustration hypothesizing that ABT-263 drives apoptosis in senescent cells via BCL-2. **c**, Dose response curve (±s.e.m.) identifying the IC50 for specific senescent

macrophage killing. The R^2 value represents the coefficient of correlation from $n = 3$ biological replicates. **d**, Flow cytometry quantification of dead cell gates via microscopy in response to ABT-263. *P* value of Tukey's test from two-way ANOVA. Data points represent percentage propidium iodide positive (PI+) cells (±s.e.m.) for $n = 384$ biological replicates. **e**, Flow cytometry quantification of apoptotic cell gates (Annexin V (AV)+ and PI+), ± s.e.m., in response to ABT-263 across a spectrum of polarized macrophage phenotypes. M0 represents naive macrophages, PC represents passage control macrophages. *P* value of Tukey's test from two-way ANOVA of $n = 3$ biological replicates. **f**, Model illustration of young (4 month) and aged (24 month) male mice treated with ABT-263 via oral gavage every day for 7 days on weeks 1 and 4. **g**, Immunofluorescence microscopy staining for macrophages (F4/80) and p21 in treated liver tissues. Images taken at ×40 magnification. Scale bar: 20 μm. **h**, Relative $p21^+$ $F4/80^+$ (senescent macrophages) abundance relative to total macrophages (±s.e.m.). $n = 6$ mice were used in each young condition, $n = 5$ aged male mice in the placebo control and $n = 7$ aged male mice on ABT-263. *P* value of Tukey's test post ANOVA. **i**, Spleen to total mouse weight ratio (±s.e.m.) in $n = 6$ male mice used in each young condition, $n = 5$ aged male mice in the placebo control and $n = 7$ aged mice on ABT-263. *P* value of Tukey's test post ANOVA. **j**, Average ± s.e.m. mRNA transcript levels (RT–qPCR) for a collection of proinflammatory genes relative to young control. *P* value of Tukey's test post ANOVA. $n = 6$ male mice were used in each young condition, $n = 5$ aged mice in the placebo control and $n = 7$ aged mice on ABT-263. **k**, Oil Red O stain representative images of $n = 6$ male mice used in each young condition, $n = 5$ aged mice in the placebo control and $n = 7$ aged mice on ABT-263. Average ± s.e.m. lipid droplet area and volume were used in the statistics. *P* value of Tukey's test post two-way ANOVA.

VAT was observed and ABT-263 had no effect on total mouse weight (Extended Data Fig. 8e,f). The effect of p21+ macrophage clearance on liver inflammation resulted in significant downregulation of multiple cytokines and chemokines (Fig. 6j). In addition, we observed reduced lipid droplet area in both the young and aged livers in response to ABT-263 (Fig. 6k). Overall, these results identify ABT-263 as a potent senolytic capable of selectively targeting macrophage senescence *in vivo*, and reducing inflammation and steatosis associated with aging.



Extended data figure 8. (**a**) SA beta galactosidase assay imaging for BMDM macrophages at 20x magnification treated with DMSO control, Rapamycin (50 nM), D (15 uM) + Q (20 uM), and ABT-263 (1 uM) for 24 hours. Scale bars represent 20 uM distance. (**b**) Representative flow cytometry gates of BMDM macrophages treated with ABT-263 1 uM for 24 hours. Gates represent AV+ and PI+ cell populations. (**c**) Average IC50 quantified on nm scale. N = 3 biological replicates. Asterisks represent the p-value of t-test ≥0.05 (ns), <0.05 (✱), <0.01

(✱✱), <0.001 (✱✱✱), <0.0001 (✱✱✱✱). (**d**) P21 + F4/80+ (senescent macrophages) abundance relative to p21+ cells in n = 5-6 liver tissues per condition. P-value of Tukey test post ANOVA. (**e**) Average mouse weight +/− SE of N = 5–7 aged mice treated with Vehicle or ABT-263. (**f**) Whole tissue staining of SA beta-galactosidase images for young (4 m) and old (24 m) VAT tissue in response to ABT-263.

5.7 ABT-263 targets a senescent macrophage signature in MASLD

To assess the pathological relevance of macrophage senescence, *CETP-APOE**3-Leiden transgenic mice on a B6 background were placed on a high-fat high-cholesterol diet (HFHCD) to model MASLD and MASH. The mice were crossed with three genetic backgrounds (129/SvJ, C57BL/6J and BXD19/Tyj) that exhibit varying degrees of liver fibrosis (Fig. 7a,b). Of note, these mice only develop MASH when fed on HFHCD for 16 weeks, and not just a high-fat diet alone. Liver samples were collected throughout the diet and pathology validated the genetic susceptibility to fibrosis, with the BXD19/Tyj strain being sensitive and the 129/SvJ strain resistant to fibrosis (Fig. 7b,c). Liver tissue samples were subjected to RNA-seq to identify MSen genes associated with macrophage senescence, such as *Cdkn1a* and *Trem2*. A strain- and time-dependent interaction was observed across all genotypes, with the highest expression of senescence markers in the BXD19/Tyj strain and the lowest in the 129/SvJ strain (Fig. 7d). Quantification of the MSen score revealed that the relationship between diet, time and macrophage senescence was strongest in the BXD19/Tyj strain compared to the 129/SvJ strain (Fig. 7e). These data suggest that strain-specific differences in fibrosis and senescent macrophage accumulation may influence the progression of liver MASLD. Based on these findings, we hypothesized that macrophages from these strains may exhibit varying intrinsic susceptibility to senescence. To test this, BMDMs were isolated from each strain and gene expression analysis

revealed strain-specific upregulation of *Cdkn1a* (p21), *Trem2* and SASP genes in Sen(IR) macrophages, with stronger effects in strains more prone to fibrosis, such as BXD19/Tyj and C57BL/6J, compared to 129/SvJ mice (Fig. 7f). Expression of *Cdkn2a* (p16) was also assessed; however, no significant differences were observed in each mouse strain (Extended Data Fig. 9a). These findings suggest that hypercholesterolemia drives macrophage senescence in vivo, and that the extent of fibrosis and senescent macrophage accumulation may be positively correlated and influenced by genetic determinants through cell-intrinsic mechanisms.

To test the contribution of macrophage senescence to fatty liver disease progression, we treated HFHCD-fed C57BL/6J APOE*CETP transgenic mice with ABT-263 or vehicle control. Treatment commenced at week 12 of the diet, because RNA-seq analysis indicated a strong increase in expression of our MSen genes in the liver at that time point (Fig. 7d–g). Interestingly, ABT-263-treated mice exhibited a significant reduction in body weight without changes in food intake (Fig. 7h,i). In the progression to MASH, splenomegaly is common because of systemic inflammation, and is reduced in ABT-263-treated mice, along with a decrease in serum tumor necrosis factor levels (Fig. 7j,k). Serum metabolites remained largely unchanged, aside from a modest effect on blood glucose, and circulating liver enzymes (alanine transaminase (ALT) and aspartate transaminase (AST)) were unaffected (Extended Data Fig. 9b–d). Notably, the liver improved dramatically, with treated livers appearing smaller and darker red compared to the enlarged, yellow-steatotic appearance typically observed in HFHCD-fed controls (Fig. 7l,m). Total liver gene expression revealed no effect on *Cdkn2a* (p16) and a reduction in *Cdkn1a* (p21), *Trem2* and inflammatory macrophage markers like *Cd68* and *Cd38*. (Fig. 7n). By contrast, we observed only modest decreases in *Cdkn1a* or *Cd38* expression in other tissues such as the

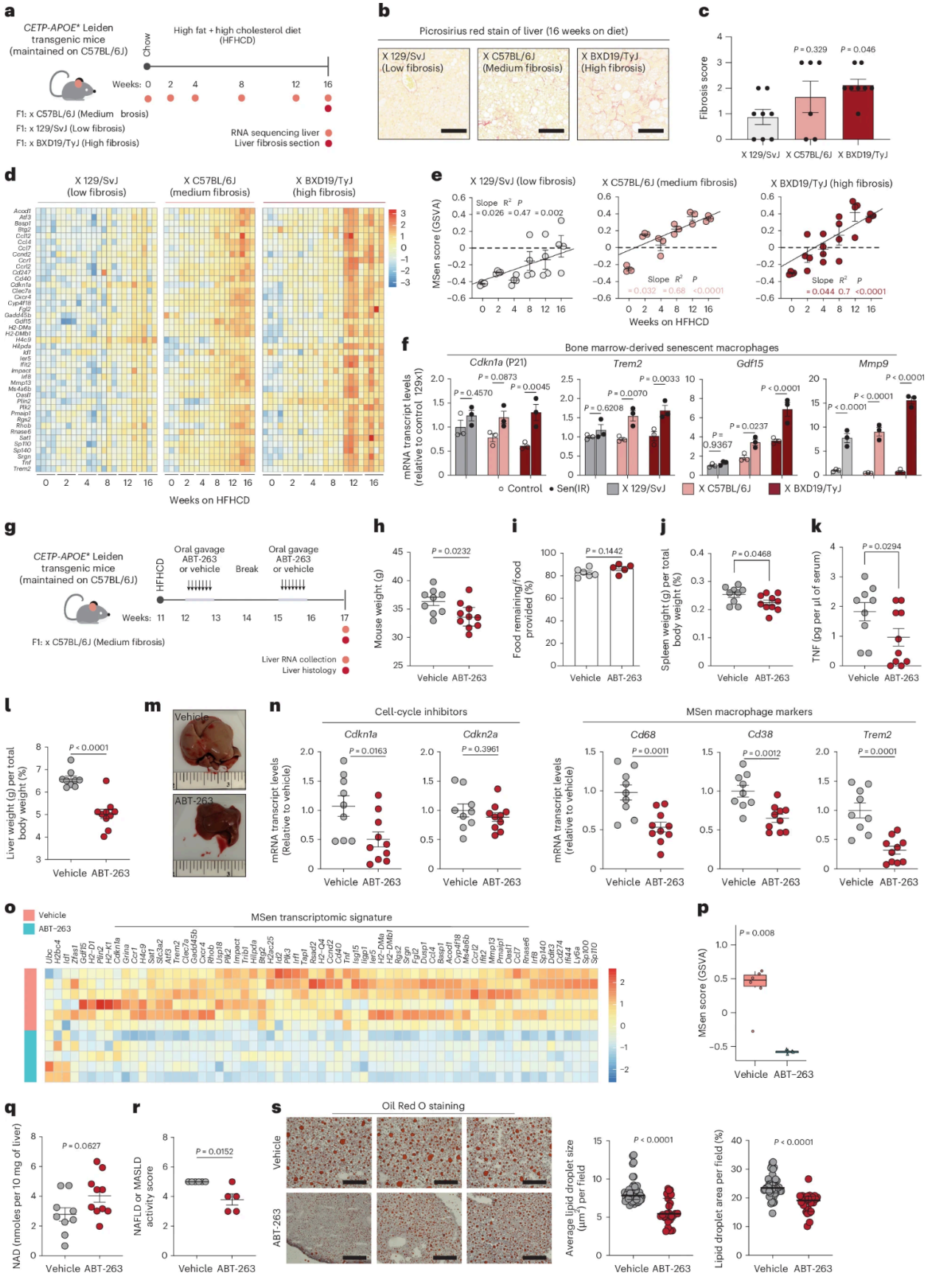

a
CETP-APOE* Leiden transgenic mice (maintained on C57BL/6J)
Chow
High fat + high cholesterol diet (HFHCD)
Weeks: 0 2 4 8 12 16
F1: x C57BL/6J (Medium brosis)
F1: x 129/SvJ (Low fibrosis)
F1: x BXD19/TyJ (High fibrosis)
RNA sequencing liver
Liver fibrosis section
b
Picrosirius red stain of liver (16 weeks on diet)
X 129/SvJ (Low fibrosis)
X C57BL/6J (Medium fibrosis)
X BXD19/TyJ (High fibrosis)
c
Fibrosis score
P = 0.329
P = 0.046
X 129/SvJ X C57BL/6J X BXD19/TyJ
d
X 129/SvJ (low fibrosis)
X C57BL/6J (medium fibrosis)
X BXD19/TyJ (high fibrosis)
Weeks on HFHCD
e
X 129/SvJ (low fibrosis)
X C57BL/6J (medium fibrosis)
X BXD19/TyJ (high fibrosis)
MSen score (GSVA)
Slope R² P
= 0.026 = 0.47 = 0.002
Slope R² P
= 0.032 = 0.68 <0.0001
Slope R² P
= 0.044 0.7 <0.0001
Weeks on HFHCD
f
Bone marrow-derived senescent macrophages
Cdkn1a (P21)
Trem2
Gdf15
Mmp9
mRNA transcript levels (relative to control 129x1)
P = 0.4570
P = 0.0873
P = 0.0045
P = 0.6208
P = 0.0070
P = 0.0033
P = 0.9367
P = 0.0237
P < 0.0001
P < 0.0001
P < 0.0001
P < 0.0001
Control Sen(IR)
X 129/SvJ
X C57BL/6J
X BXD19/TyJ
g
CETP-APOE* Leiden transgenic mice (maintained on C57BL/6J)
HFHCD
Oral gavage ABT-263 or vehicle
Break
Oral gavage ABT-263 or vehicle
Weeks: 11 12 13 14 15 16 17
F1: x C57BL/6J (Medium fibrosis)
Liver RNA collection
Liver histology
h
Mouse weight (g)
P = 0.0232
Vehicle ABT-263
i
Food remaining/food provided (%)
P = 0.1442
Vehicle ABT-263
j
Spleen weight (g) per total body weight (%)
P = 0.0468
Vehicle ABT-263
k
TNF (pg per µl of serum)
P = 0.0294
Vehicle ABT-263
l
Liver weight (g) per total body weight (%)
P < 0.0001
Vehicle ABT-263
m
Vehicle
ABT-263
n
Cell-cycle inhibitors
Cdkn1a
Cdkn2a
mRNA transcript levels (Relative to vehicle)
P = 0.0163
P = 0.3961
Vehicle ABT-263
MSen macrophage markers
Cd68
Cd38
Trem2
mRNA transcript levels (relative to vehicle)
P = 0.0011
P = 0.0012
P = 0.0001
Vehicle ABT-263
o
Vehicle
ABT-263
MSen transcriptomic signature
p
MSen score (GSVA)
P = 0.008
Vehicle ABT-263
q
NAD (nmoles per 10 mg of liver)
P = 0.0627
Vehicle ABT-263
r
NAFLD or MASLD activity score
P = 0.0152
Vehicle ABT-263
s
Oil Red O staining
Vehicle
ABT-263
Average lipid droplet size (µm²) per field
P < 0.0001
Vehicle ABT-263
Lipid droplet area per field (%)
P < 0.0001
Vehicle ABT-263

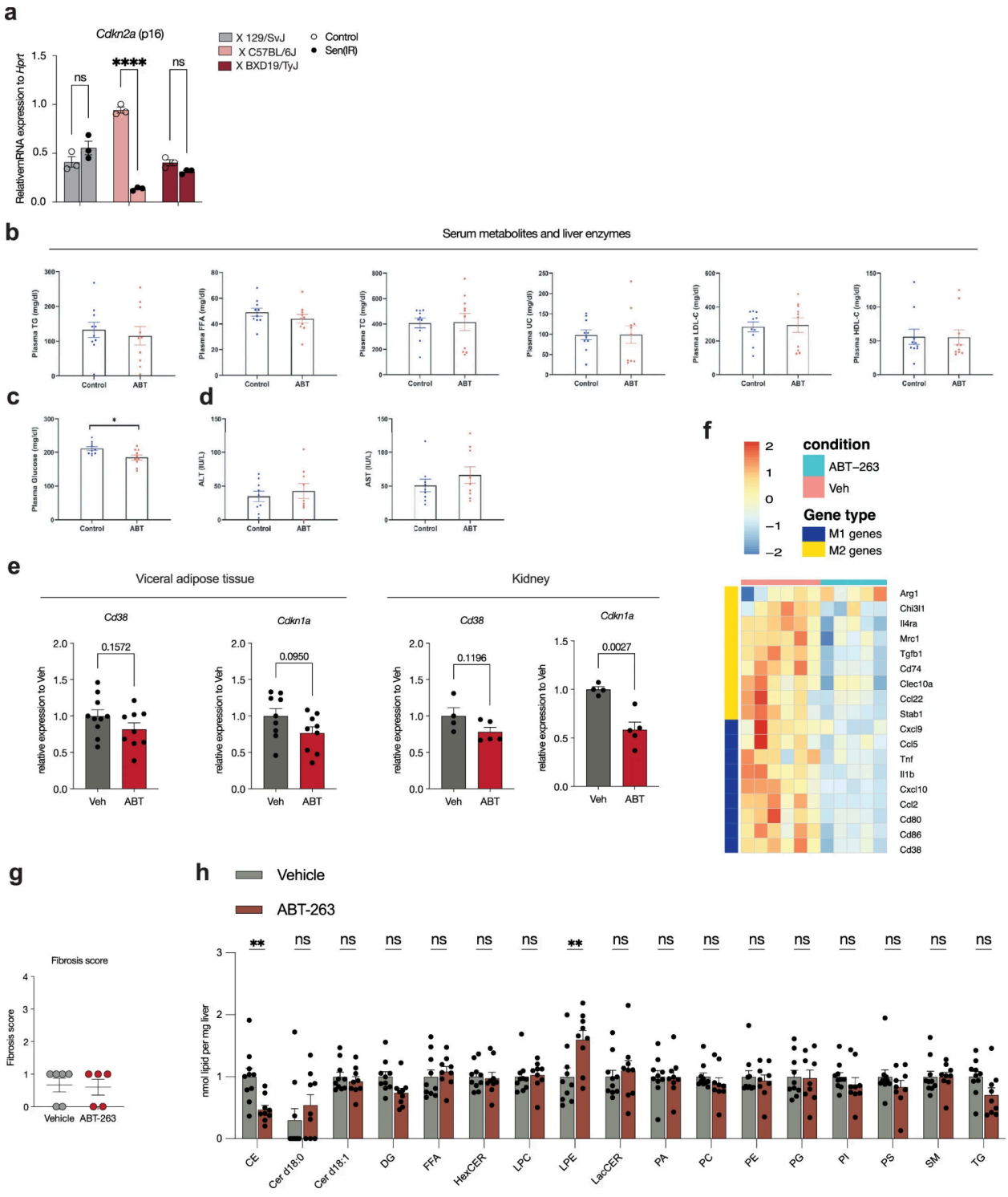
Figure 7. a, Model illustration of *CETP-APOE** Leiden transgenic mice maintained on C57BL/6J then crossed to three additional genetic backgrounds susceptible (BXD19/TyJ and C57BL/6J) and resistant (129/SvJ) to developing to MASLD. **b**, Representative picrosirius red stain for liver fibrosis after 16 weeks on HFHCD. Scale bars represent a 20 μm distance. **c**, Pathology grades of fibrosis of $n = 4–6$ male liver sections stained with picrosirius red stain. Data represent median ± s.e.m. **d**, Bulk RNA-seq of transcript levels for MSen gene signature across weeks 0–16 on HFHCD. **e**, Mean ± s.e.m. MSen scores across weeks 0–16 on HFHCD for each genetic background. Best-fit line and *P* value derived from a simple linear regression model of $n = 3–6$ male mice per time point. **f**, Mean ± s.e.m. mRNA transcript levels (RT–qPCR) relative to control of BMDMs from *CETP-APOE**Leiden mice crossed on different three backgrounds. *P* value from a two-way ANOVA. $n = 3$ biological replicates per strain and condition were used. **g**, Model illustration of *CETP-APOE**Leiden transgenic mice crossed on the C57BL/6J genetic background. Mice were treated with ABT-263 via oral gavage every day for 7 days on weeks 12 and 15. **h**, Mean ± s.e.m. weight of $n = 9$ placebo mice and $n = 10$ ABT-263-treated mice at 17 weeks. *P* value derived from a two-sided *t*-test. **i**, Mean ± s.e. change in food intake for $n = 6$ placebo cages and $n = 5$ ABT-263-treated cages at 17 weeks. **j**, Mean ± s.e. spleen weight (in grams) relative to total weight of $n = 9$ placebo mice and $n = 10$ ABT-263-treated mice at 17 weeks. *P* value derived from a two-sided *t*-test. **k**, Enzyme-linked immunosorbent assay quantification for picograms of tumor necrosis factor found in every microliter of serum collected. *P* value derived from a one-sided *t*-test. Mean ± s.e.m. of $n = 9$ placebo mice and $n = 10$ ABT-263-treated mice at 17 weeks. **l**, Mean liver weight (in grams) relative to total weight ± s.e. of $n = 9$ placebo mice and $n = 10$ ABT-263-treated mice at 17 weeks. *P* value derived from a two-sided *t*-test. **m**, Representative liver photographs at 17 weeks immediately after tissue

harvest. Scale rule: inches. **n**, Mean mRNA transcript levels (RT–qPCR) for SASP, senescent and macrophage genes in bulk liver samples relative to placebo control. *P* value derived from a two-sided *t*-test. Bar plots: average ± s.e.m. of $n = 9$ placebo mice and $n = 10$ ABT-263-treated mice at 17 weeks. **o**, Bulk RNA-seq of the MSen transcriptomic signature (genes derived from aged macrophages in vivo and senescent macrophages in vitro) in response to the senolytic drug, ABT-263. Scale bar: $\log_2[\text{TPM} + 1]$ expression on a *z*-score axis. $n = 6$ vehicle and $n = 5$ ABT-263-treated mice used in this experiment. **p**, GSVA scoring of MSen genes in the livers of vehicle- or drug-treated mice. Box-and-whisker plots display the median (center line), interquartile range (25th to 75th percentiles; box), and minimum and maximum values (whiskers). *P* values were calculated using a nonparametric Wilcoxon test. $n = 6$ vehicle-treated and $n = 5$ ABT-263-treated mice were analyzed. **q**, Total NAD (pmol per mg of liver analyzed) quantified by LC–MS/MS. Mean ± s.e.m. of NAD distribution in response to ABT-263. $n = 9$ placebo mice and $n = 10$ ABT-263-treated mice at 17 weeks. *P* value derived from a two-sided *t*-test. **r**, Nonalcoholic fatty liver disease (MASLD) activity score based on pathology grades for each condition. Bar: mean ± s.e. *P* value derived from Student's *t*-test. **s**, Oil Red O stains are shown for three representative mice treated with vehicle or ABT-263. Scale bars represent a 20 μm distance. Mean ± s.e.m. lipid droplet size and area analyzed in eight images per liver section, and the average size (μm^2) from eight slides for each mouse was used for statistical analysis. $n = 6$ vehicle and $n = 5$ ABT-263-treated mice used in this analysis. *P* value derived from Student's *t*-test.

kidney or VAT (Extended Data Fig. 9e), suggesting that cholesterol-driven macrophage senescence primarily affects the liver. Furthermore, using unbiased transcriptomics, we observed

reduced expression of M1 and M2 genes and a significant decrease in the MSen transcriptomic signature (Fig. 7o,p and Extended Data Fig. 9f).

High CD38 expression, linked to senescent cell burden, can lead to NAD+ degradation in the liver. Given the reduction in liver Cd38 expression and reduction in the MSen signature following senolytic treatment, we hypothesized that liver NAD^+ levels might be restored after targeting senescent macrophages. When measured, liver NAD^+ levels in ABT-263-treated mice increased by 30%, suggesting that senescent macrophages regulate tissue NAD^+ metabolism likely via a Cd38-dependent mechanism (Fig. 7q). Histological analysis of liver sections stained with picrosirius red revealed no significant change in fibrosis grade; however, a reduction in the nonalcoholic fatty liver disease activity score, driven by improvements in steatosis, was observed (Fig. 7r and Extended Data Fig. 9g). Oil Red O staining showed a significant decrease in lipid droplet size and area in ABT-263-treated mice (Fig. 7s). In addition, ABT-263 treatment reshaped the liver lipidome, reducing cholesterol esters and triglycerides while increasing lysophosphatidylethanolamine (Extended Data Fig. 9h). Together, these findings suggest that macrophage senescence occurs in cholesterol-driven liver disease and that targeting senescent macrophages reduces systemic inflammation and improves liver steatosis in MASLD, therefore preventing CD38-dependent NAD+ decline. These results complement a recent study showing that elimination of p21+ senescent cells during aging improves metabolic health and extends lifespan in mice, and suggest this may be dependent in part on targeting $p21^+Trem2^+$ senescent macrophages.



Extended data figure 9. (**a**) Relative Cdkn2a mRNA transcript levels of BMDMs from CETP-APOE* Leiden mice crossed on different three backgrounds. Asterisks represent the p-value of ANOVA ≥ 0.05 (ns), <0.05 (✱), <0.01 (✱✱), <0.001 (✱✱✱), <0.0001 (✱✱✱✱).

(**b-d**) Serum metabolite, serum lipid levels, and serum liver enzymes related to pathology MASH mice. ND was observed outside blood glucose. Asterisks represent the p-value of t-test ≥0.05 (ns), <0.05 (✱), <0.01 (✱✱), <0.001 (✱✱✱), <0.0001 (✱✱✱✱). (**e**) Relative mRNA transcript levels for inflammatory genes in bulk visceral adipose (VAT) and kidney samples. P-value represents the results of the t-test. (**f**) Bulk-RNAseq of the M1 and M2 genes in response to the senolytic drug, ABT-263. Scale bar represents Log2[TPM + 1] expression on a z-score axis. N = 6 Vehicle, and N = 5 ABT-263 treated mice used in this experiment. (**g**) Pathology graded histology reports for fibrosis on 5-6 MASH mice with and without ABT-263. (**h**) Fold change differences of normalized lipid abundance (nmol lipid per mg liver) for all lipid species via shotgun lipidomics (LC-MS/MS) relative to vehicle. Asterisks represent the p-value of t-test ≥0.05 (ns), <0.05 (✱), <0.01 (✱✱), <0.001 (✱✱✱), <0.0001 (✱✱✱✱).

5.8 Scar-associated macrophages express a human senescent macrophage gene signature

To determine whether human macrophages can undergo senescence, macrophages derived from peripheral blood mononuclear cells (PBMCs) were subjected to the Sen(IR) and Sen(Doxo) models, similar to the mouse BMDM protocols (Fig. 8a). We observed a significant increase in *TREM2, CDKN1A* (p21), *GDF15* and *CD38* expression in both Sen(IR) and Sen(Doxo) macrophages (Fig. 8b). The expression of *CDKN2A, IFNα, IFNβ, MMP9* and *MMP12* did not change significantly (Fig. 8b and Extended Data Fig. 10). Interestingly, the increased protein expression of p21 and reduced p16 expression were similar to that seen in mouse senescent macrophages (Fig. 8c). In addition, SA-β-gal activity and reduced proliferative capacity were observed in human Sen(IR) macrophages (Fig. 8d,e). Together, these findings suggest that the Sen(IR) model in human macrophages serves as a reliable system for investigating the mechanisms and biomarkers of human macrophage senescence.

To further explore human senescent macrophage biology, an unbiased bulk RNA-seq approach was used to capture global transcriptomic changes. In this experiment, we observed a donor-specific response to IR and Doxo, suggesting that genetics has an influence on senescence susceptibility, similar to that we observed in senescent macrophages from varying strains of mice. Among donors, PCA demonstrated clear separation between senescent and control macrophages, with 1,200 DEGs identified (analysis of variance (ANOVA), with a modest q value <0.1) (Fig. 8f). This clustering indicated a distinct transcriptional phenotype in senescent

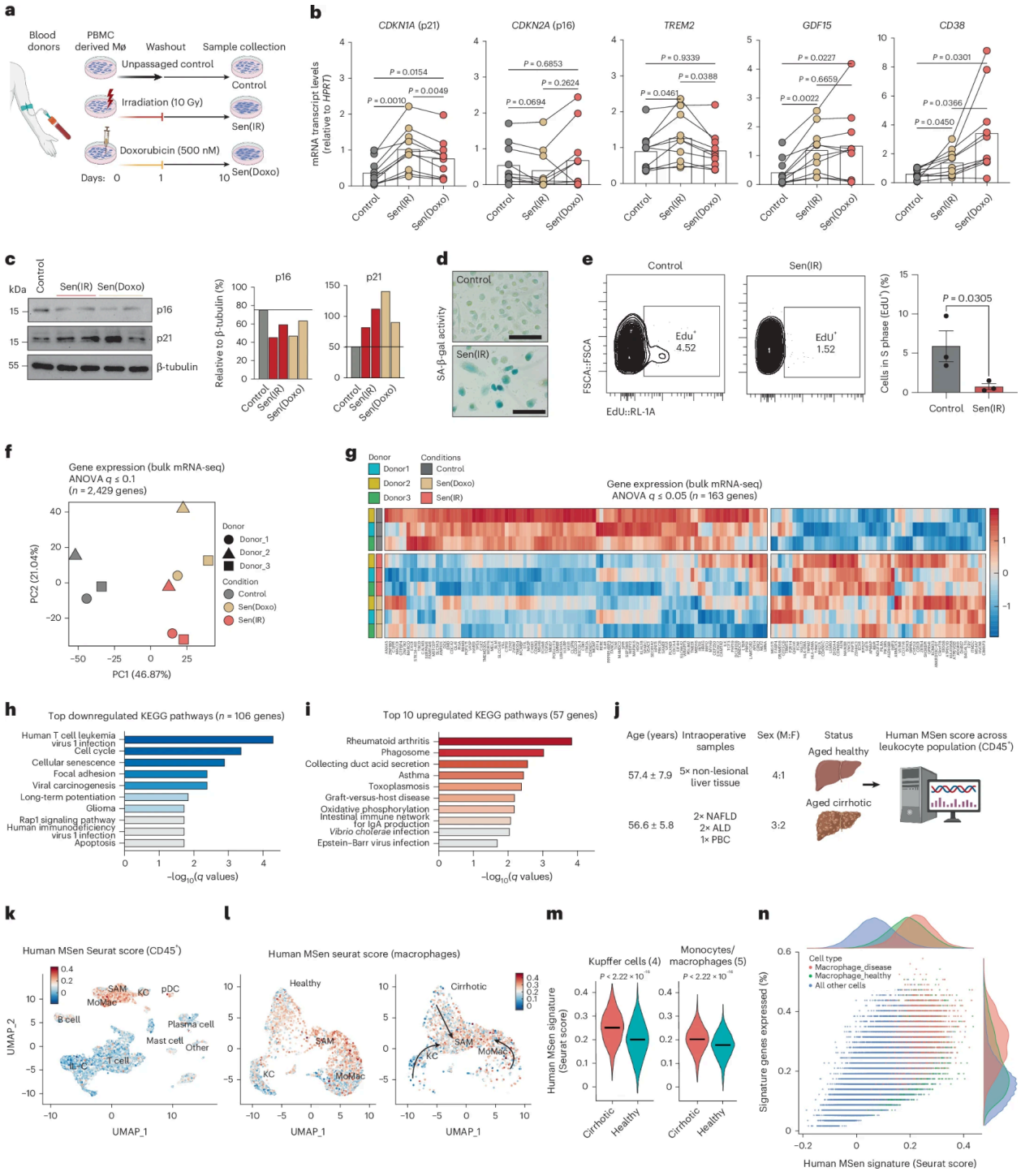


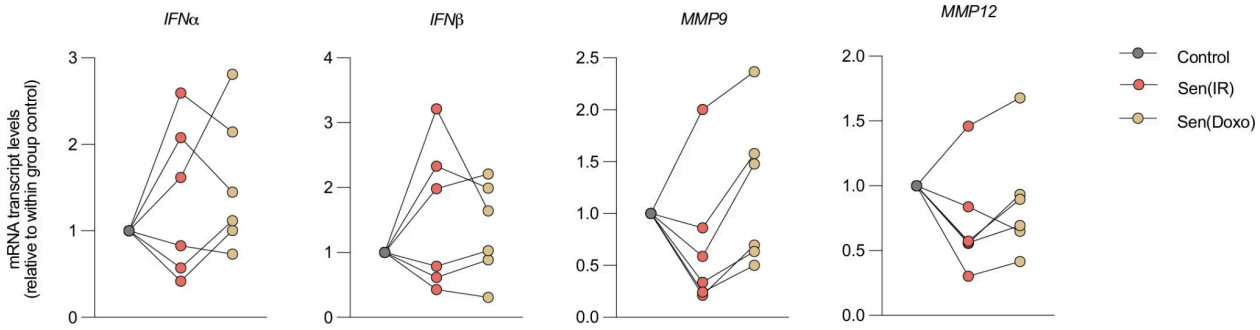
Figure 8. **a**, Illustration of the in vitro model system using exogenous DNA damage with irradiation and Doxo on PBMC-derived macrophages from male and female human donors. **b**, Mean ± s.e. gene expression (RT–qPCR) normalized to control. $n = 9$ donors (mixed male and

female) for control and Sen(IR) conditions. $n = 8$ for Sen(Doxo) conditions. *P* value from Tukey's test post repeated measures ANOVA analysis. **c**, SDS–PAGE gels and immunostaining (western blot) for p21 and p16 in response to 10 days post DNA damage. ImageJ quantification for band intensity is shown to the right and represents relative intensity over the loading control. **d**, SA-β-gal images of human senescent macrophages. **e**, Click-iT EdU labeling of cells to assess proliferation dynamics. Axes represent the percentage of cells positive for the stain relative to the parental gate, as detected by flow cytometry. The bar plot represents the mean ± s.e. of $n = 3$ independent donors. *P* value derived from unpaired one-sided *t*-test. **f**, PCA on bulk RNA-seq samples from 10 days post DNA damage for three blood donors. **g**, Heatmap projection of all statistically significant DEGs compared to control conditions. **h**, KEGG pathway enrichment analysis for the top ten pathways downregulated in human senescent macrophages. **i**, KEGG pathway enrichment analysis for the top ten pathways upregulated in human senescent macrophages. **j**, Model illustration of running MSen score on publicly accessible single-cell dataset of human liver biopsy samples from five people with liver cirrhosis and five with a healthy liver. **k**, UMAP projection of all annotated $CD45^+$ cell types and colored by human MSen Seurat score. **l**, UMAP projection of *CD68*$^+$ cells (macrophages) in healthy and cirrhotic tissue samples. Color denotes human MSen Seurat score. **m**, Distribution of MSen Seurat score across resident macrophage (Kupffer cells) and non-resident monocyte and macrophage populations in healthy and cirrhotic conditions. *P* value represents the results of a two-sided *t*-test. **n**, Distribution of human MSen score across all $CD45^+$ cell types in the dataset. ALD, alcohol-related liver disease; F, female; KC, Kupffer cell; IgA, immunoglobulin A; IL-C, innate lymphoid cell; M, male; MoMac, monocyte-derived macrophage; Mø, macrophage; PBC, primary biliary cholangitis; pDC, plasmacytoid dendritic cell.

macrophages, with 163 genes being differentially expressed (ANOVA, $q < 0.05$) across all donor conditions during senescence (Fig. 8g). Upregulated genes included redox and detoxification factors (*MGST1, QSOX1, ALDH3B1*), mitochondrial regulators *(ISCU, NDUFA4, COX7A1*) and lysosomal or vesicular components *(ATP6V1D, ATP6V0E1, MAN2B1, SIDT1*), reflecting increased lysosomal activity characteristic of senescence. Metabolic and lipid-handling genes (*FABP4, GRAMD1B, APMAP*) and canonical senescence markers (*CDKN1A and CDKN1C*) were elevated, alongside antigen presentation and immune-modulatory transcripts (*HLA-DRA, HLA-DMA, FCN1, MS4A7, ADGRE1*), indicating an inflammatory phenotype. By contrast, genes governing cell-cycle progression and DNA replication were markedly repressed, including *CDK1, CDC20, CHEK1, MCM7 and TOP2A*, consistent with irreversible proliferative arrest. DNA repair factors (*EXO1, MSH6, BLM, RECQL4*) and nuclear lamina components *(LMNB1 and LMNA*) were also reduced, reflecting deep senescence and impaired genome maintenance (Fig. 8g). KEGG analysis revealed that downregulated genes were primarily involved in cell proliferation pathways, while the upregulated genes were associated with inflammatory responses (Fig. 8h,i). Together, these transcriptional changes define a stable senescent macrophage phenotype characterized by heightened stress and lysosomal programs coupled with altered proliferative, metabolic and immune functions.

To evaluate whether senescent macrophages represent *TREM2*$^{+}$ macrophages in liver disease, we analyzed a publicly available single-cell RNA-seq dataset of human liver cirrhosis that identified a *TREM2*$^{+}$ scar-associated macrophage (SAM) population (Fig. 8j). Using the genes identified in our bulk human MSen transcriptomic analysis as a scoring method, we observed significant enrichment for senescence-associated genes in *Cd45*+ immune cells in both

healthy and diseased livers, with macrophages being the most enriched (Fig. 8k,l). Further analysis into *Cd45*$^{+}$*Cd68*$^{+}$ macrophages revealed a pre-existing SAM population enriched for senescence in the human control samples (Fig. 8m). In the context of cirrhosis, Kupffer cells and monocytes and/or macrophages appear to transition into SAMs that score high for the human MSen signature and outrank all other immune cells in the liver (Fig. 8m,n). These results indicate that macrophage senescence is present in human chronic liver diseases, including MASLD and cirrhosis, and may represent a therapeutic target.



Extended data figure 10. Relative gene expression (RT-qPCR_ normalized to within donor control. N=0 donors, no gene was significant by p-value statistics. Each line represents paired data points.

Chapter 6:

Discussion and conclusions

In this study, we characterized DNA damage and cholesterol-induced macrophage senescence, uncovering stable senescent phenotypes defined by irreversible cell-cycle arrest and a robust SASP phenotype. A key finding was the upregulation of *Cdkn1a* (p21) expression during senescence, supporting p21 as a more reliable marker of macrophage senescence compared to *Cdkn2a* (p16), which was paradoxically downregulated or unchanged in both mouse and human macrophage models. Our data are also consistent with recent publications describing distinct p21+ or p16+ senescent cells, referred to as senotypes. Nevertheless, our data suggest that neither p21 nor p16 alone is sufficient to definitively identify senescent macrophages, reinforcing the need for multiple markers and cell-specific approaches. By comparing senescent macrophages with classical M1 and M2 polarized states, we identified additional distinguishing features, notably high expression of *Trem2*, altered nuclear morphology, lipid metabolism and type I IFN hyperactivation.

Lipidomic analyses revealed that cholesterol storage, particularly storage of cholesterol esters and ceramides, not only marked senescent macrophages, but also acted as a physiological driver of the senescent state. This finding links senescence to metabolic dysfunction and highlights an important, previously underexplored lipid axis that drives the senescent cell burden in age-related diseases. Furthermore, we demonstrated that the senolytic ABT-263 selectively eliminated $p21^{+}$ senescent macrophages both *in vitro* and *in vivo*, resulting in reduced hepatic steatosis and systemic inflammation. Moreover, prior studies using ABT-263 in aged mice reported improvements in organ function and metabolic health. Our findings suggest that clearance of senescent macrophages may account, at least in part, for these benefits. This therapeutic effect is particularly timely given the rising global burden of metabolic diseases driven by dietary excess and aging.

Our findings raise the intriguing possibility that diets rich in excess cholesterol accelerate aging by driving senescence in tissue-resident macrophages, an aging hallmark traditionally associated with advanced age. Our data also suggest that senolytic strategies could potentially treat not only MASLD, but also other cholesterol-driven diseases such as atherosclerosis, where senescent-like macrophages have been observed. Future studies will need to determine whether targeting senescent macrophages can halt or reverse the broader spectrum of age-associated inflammatory disorders where these cells have been recently implicated, including cancer.

Another critical question centers on how cholesterol acts as a stressor to induce senescence. Cholesterol has essential roles in membrane structure and cell signaling, but excess intracellular cholesterol can be cytotoxic and drive inflammation. Although cholesterol itself has not been directly linked to genomic instability, its contribution to mitochondrial dysfunction, oxidative stress and endoplasmic reticulum stress may promote a stress response that drives senescence. Elucidating the molecular mechanisms connecting lipid overload to macrophage senescence will be crucial for understanding the intersection of metabolism and inflammaging at a deeper mechanistic level.

In conclusion, this study establishes *p21*$^{+}$*TREM2*$^{+}$ senescent macrophages as a distinct, pathogenic population that drives sterile inflammation in aging and MASLD. However, several important limitations of our study remain. First, our study uses male mice as the primary source of BMDMs and for *in vivo* studies. However, given the strong genetic influence on senescent macrophage phenotypes, it is possible that sex chromosomes may influence key senescent hallmarks, which is currently under investigation in our laboratory. Second, our in vivo analysis primarily focuses on characterizing and identifying senescent Kupffer cells in the liver. We

hypothesize that other tissue-resident macrophage populations, particularly in organs with large tissue-resident macrophage reservoirs such as the brain, skin, VAT and heart, are also susceptible to senescence. Importantly, these macrophages may undergo senescence via distinct mechanisms, resulting in diverse phenotypic states and biomarker profiles that will require tailored identification strategies. Thus, future work should prioritize the development of macrophage specific senescence reporter mice that could facilitate the selective targeting and tracking of senescent macrophages in complex tissues and conditions. Establishing these tools would enable the field to determine not only the burden and dynamics of macrophage senescence during aging and disease, but also causal relationships with pathology and macrophage-targeted senolytic strategies as promising therapeutic interventions to combat chronic inflammation, metabolic dysfunction and age-related tissue decline.

Chapter 7

Future Directions: From biomarkers to bedside

7.1 Limitations: Distinct state may not mean novel driver in MASLD

Several strengths of this study reinforce the robustness of cellular senescence being a plausible cell state in macrophages and provide important insight into the physiological mechanisms of chronic inflammation in the context of aging. To begin, this study is the first of its kind to use *In vitro* cell-state characterization experiments of cellular senescence in macrophages and identified a distinct $p21^{+}TREM2^{+}$ macrophage population that exhibited canonical features of cellular senescence, evidence that inevitably address a longstanding debate regarding whether mature macrophages can adopt a bona fide senescent state (Behmoaras & Gil, 2021). These experiments established a molecular and functional framework for defining macrophage senescence and provided evidence that this phenotype represents a discrete cellular state rather than a generalized inflammatory activation program (Hall et al., 2016, 2017; L. Wang et al., 2024). Complementary single-cell transcriptomic analyses further strengthened these observations by demonstrating that senescence-associated transcriptional programs are enriched in macrophage populations within aged tissues. Reanalysis of the Tabula Muris Senis dataset investigating p21 accumulation, rather than p16, showed that Kupffer cells express p21 and preferentially accumulated lipid-regulating, senescence- and inflammaging-associated signatures during aging compared with hepatocytes or endothelial cells (Tabula Muris Consortium, 2020). This re-analysis supported the physiological relevance of macrophage senescence *in vivo* and matched lipid regulating findings since the 1990s (Hayek et al., 1997). Furthermore, senescent macrophages ($p21^{+}F4/80^{+}$), represented 80% +/- 10% of the total $p21^{+}$ cells in the aged liver and *in vivo* senolytic with ABT-263 demonstrated effective depletion of $p21^{+}$ macrophages in aged mice alongside reductions in hepatic inflammation and steatosis, providing translational evidence that this population is therapeutically targetable in the context of aging.

Despite these strengths in understanding senescent macrophage function and accumulation in the context of normal physiology, several limitations remain in defining the precise contribution of senescent macrophages in the context of patho-physiology, specifically in one of the leading age related metabolic diseases, metabolic dysfunction–associated steatotic liver disease (MASLD)(Le et al., 2025).

MASLD is a multifactorial disease involving complex interactions among senescent hepatocytes, senescent stellate cells, senescent endothelial cells, and now senescent immune populations(Kumar et al., 2026; Le et al., 2025; Mastoridou et al., 2026; Vu et al., 2026). Additionally, the *Cetp-Apoe*3* leiden model used to develop MASLD mice is not biased towards macrophage senescence. We demonstrate throughout the studies that macrophages harboring these mutations drive senescence, but this can also be the case for the rest of the liver cell populations. Therefore, broad senolytic treatment improved disease phenotypes, but it is unknown which senescent cell populations that have independently been implicated in steatosis, inflammation, and fibrosis (Du et al., 2025; Gold et al., 2025; Ogrodnik et al., 2017; Y. Yang et al., 2025). No macrophage-restricted senolytic approach or genetic depletion strategy was used to selectively eliminate $p21^{+}TREM2^{+}$ macrophages while preserving other senescent populations.

As a result, while these findings strongly support the existence of a bona fide senescent macrophage state and demonstrate its accumulation in aged and diseased tissues, they do not definitively establish whether this population functions as a necessary or sufficient driver of MASLD progression. Future studies using lineage-specific depletion models and mechanistic interrogation of intercellular signaling networks will be necessary to determine the extent to which senescent macrophages directly drive disease pathology versus acting as one component of a broader senescent tissue ecosystem.

7.2 The double-edged nature of senescence is overlooked

Another important limitation is that the context-dependent nature of senescent macrophages in MASLD is not fully explored. A growing body of literature demonstrates that senescence is not universally pathogenic and can serve beneficial physiological functions depending on tissue context, timing, and duration (Ohtani et al., 2012). Transient senescence programs have been implicated in tumor suppression during early carcinogenesis, tissue repair during acute injury, wound healing, and developmental tissue remodeling (Grosse et al., 2020; Ohtani et al., 2012; Park et al., 2021; X. Wang et al., 2023). This broader complexity is not extensively addressed in the current study, which primarily frames $p21^{+}TREM2^{+}$ macrophages as pathological drivers of metabolic dysfunction.

This distinction is particularly important because several findings suggest that macrophages possess context-dependent functional roles in highly metabolic tissues like the liver. The current *In vitro* experiments demonstrated enhanced phagocytic capacity, but poor efferocytosis of dead cell debris, and transcriptional analyses identified heightened responsiveness to LPS. In other disease settings, $TREM2^{+}$ macrophage populations have been reported to exhibit both protective and pathogenic functions depending on the tissue environment and stage of disease progression, including contexts such as cancer, neurodegeneration, and fibrosis(Telemaco Contreras Colmenares et al., 2024). As a result, the current experiments conducted highlight a lipid-specific role for TREM2, but more work is required to investigate its functional role *in vitro* and *in vivo*.

The current data also strongly support the accumulation of these cells during aging and disease, but the temporal and context-specific consequences of their persistence remain incompletely defined. Future studies examining whether $p21^{+}TREM2^{+}$ macrophages contribute to

early tissue repair, debris clearance, or transient adaptive responses before becoming maladaptive during chronic disease progression would provide a more complete understanding of their biological role and help refine early biomarkers of pathophysiology.

7.3 Broader implications: The missing steps to move into the clinic

Another important idea relates to the study's translational potential. The macrophage senescence (MSen) transcriptomic signature that can identify senescent macrophages from large high resolution single cell data sets, of which include scRNAseq and spatial transcriptomics. This represents a meaningful macrophage-centered framework to distinguish senescent macrophages from other inflammatory states and enables re-annotation of existing single-cell datasets that include clinical data sets.

An example of this include the *in vitro* human monocyte-derived macrophages and human cirrhotic liver datasets, where $TREM2^{+}$ scar-associated macrophages exhibited strong MSen enrichment. These findings strengthen the relevance of the model in human disease and establish a valuable resource for future studies investigating immune senescence MASLD.

This data together highlights the large potential of the MSen signature on a path toward clinically actionable biomarkers. Low-dimensional diagnostic tools: such as circulating SASP biomarkers, imaging modalities, or simplified flow cytometric panels should be tools to use in combination with the MSen score to identify highly correlative, and possibly casual, clinical readouts to replace the highly laborious and expensive high resolution single cell technologies. Additionally, prospective human cohorts should be examined to determine whether MSen burden correlates with disease progression, fibrosis risk, or treatment response. As a result, the ability to translate these findings into patient stratification strategies or therapeutic decision-making remains limited, but contains high potential.

Bibliography

Acklin, S., Zhang, M., Du, W., Zhao, X., Plotkin, M., Chang, J., Campisi, J., Zhou, D., & Xia, F. (2020). Depletion of senescent-like neuronal cells alleviates cisplatin-induced peripheral neuropathy in mice. *Scientific Reports*, *10*(1), 14170.

Anerillas, C., Mazan-Mamczarz, K., Herman, A. B., Munk, R., Lam, K.-W. G., Calvo-Rubio, M., Garrido, A., Tsitsipatis, D., Martindale, J. L., Altés, G., Rossi, M., Piao, Y., Fan, J., Cui, C.-Y., De, S., Abdelmohsen, K., de Cabo, R., & Gorospe, M. (2023). The YAP-TEAD complex promotes senescent cell survival by lowering endoplasmic reticulum stress. *Nature Aging*, *3*(10), 1237–1250.

Avolio, R., Inglés-Ferrándiz, M., Ciocia, A., Coll, O., Bonnin, S., Guitart, T., Ribó, A., & Gebauer, F. (2022). Coordinated post-transcriptional control of oncogene-induced senescence by UNR/CSDE1. *Cell Reports*, *38*(2), 110211.

Azarm, K., Bhardwaj, A., Kim, E., & Smith, S. (2020). Persistent telomere cohesion protects aged cells from premature senescence. *Nature Communications*, *11*(1), 3321.

Behmoaras, J., & Gil, J. (2021). Similarities and interplay between senescent cells and macrophages. *The Journal of Cell Biology*, *220*(2). https://doi.org/10.1083/jcb.202010162

Benayoun, B. A., Pollina, E. A., Singh, P. P., Mahmoudi, S., Harel, I., Casey, K. M., Dulken, B. W., Kundaje, A., & Brunet, A. (2019). Remodeling of epigenome and transcriptome landscapes with aging in mice reveals widespread induction of inflammatory responses. *Genome Research*, *29*(4), 697–709.

Camell, C. D., Yousefzadeh, M. J., Zhu, Y., Prata, L. G. P. L., Huggins, M. A., Pierson, M., Zhang, L., O'Kelly, R. D., Pirtskhalava, T., Xun, P., Ejima, K., Xue, A., Tripathi, U.,

Espindola-Netto, J. M., Giorgadze, N., Atkinson, E. J., Inman, C. L., Johnson, K. O., Cholensky, S. H., … Robbins, P. D. (2021). Senolytics reduce coronavirus-related mortality in old mice. *Science (New York, N.Y.)*, *373*(6552). https://doi.org/10.1126/science.abe4832

Chaib, S., Tchkonia, T., & Kirkland, J. L. (2022). Cellular senescence and senolytics: the path to the clinic. *Nature Medicine*, *28*(8), 1556–1568.

Contrepois, K., Coudereau, C., Benayoun, B. A., Schuler, N., Roux, P.-F., Bischof, O., Courbeyrette, R., Carvalho, C., Thuret, J.-Y., Ma, Z., Derbois, C., Nevers, M.-C., Volland, H., Redon, C. E., Bonner, W. M., Deleuze, J.-F., Wiel, C., Bernard, D., Snyder, M. P., … Mann, C. (2017). Histone variant H2A.J accumulates in senescent cells and promotes inflammatory gene expression. *Nature Communications*, *8*, 14995.

Coppé, J.-P., Patil, C. K., Rodier, F., Sun, Y., Muñoz, D. P., Goldstein, J., Nelson, P. S., Desprez, P.-Y., & Campisi, J. (2008). Senescence-associated secretory phenotypes reveal cell-nonautonomous functions of oncogenic RAS and the p53 tumor suppressor. *PLoS Biology*, *6*(12), 2853–2868.

Correia-Melo, C., Marques, F. D. M., Anderson, R., Hewitt, G., Hewitt, R., Cole, J., Carroll, B. M., Miwa, S., Birch, J., Merz, A., Rushton, M. D., Charles, M., Jurk, D., Tait, S. W. G., Czapiewski, R., Greaves, L., Nelson, G., Bohlooly-Y, M., Rodriguez-Cuenca, S., … Passos, J. F. (2016). Mitochondria are required for pro-ageing features of the senescent phenotype. *The EMBO Journal*, *35*(7), 724–742.

Covarrubias, A. J., Aksoylar, H. I., Yu, J., Snyder, N. W., Worth, A. J., Iyer, S. S., Wang, J., Ben-Sahra, I., Byles, V., Polynne-Stapornkul, T., Espinosa, E. C., Lamming, D., Manning, B. D., Zhang, Y., Blair, I. A., & Horng, T. (2016). Akt-mTORC1 signaling regulates Acly to integrate metabolic input to control of macrophage activation. *eLife*, *5*.

https://doi.org/10.7554/eLife.11612

Demaria, M., Ohtani, N., Youssef, S. A., Rodier, F., Toussaint, W., Mitchell, J. R., Laberge, R.-M., Vijg, J., Van Steeg, H., Dollé, M. E. T., Hoeijmakers, J. H. J., de Bruin, A., Hara, E., & Campisi, J. (2014). An essential role for senescent cells in optimal wound healing through secretion of PDGF-AA. *Developmental Cell*, *31*(6), 722–733.

de Mera-Rodríguez, J. A., Álvarez-Hernán, G., Gañán, Y., Martín-Partido, G., Rodríguez-León, J., & Francisco-Morcillo, J. (2021). Is Senescence-Associated β-Galactosidase a Reliable Marker of Cellular Senescence During Embryonic Development? *Frontiers in Cell and Developmental Biology*, *9*, 623175.

Dimri, G. P., Lee, X., Basile, G., Acosta, M., Scott, G., Roskelley, C., Medrano, E. E., Linskens, M., Rubelj, I., & Pereira-Smith, O. (1995). A biomarker that identifies senescent human cells in culture and in aging skin in vivo. *Proceedings of the National Academy of Sciences of the United States of America*, *92*(20), 9363–9367.

Du, K., Umbaugh, D. S., Wang, L., Jun, J. H., Dutta, R. K., Oh, S. H., Ren, N., Zhang, Q., Ko, D. C., Ferreira, A., Hill, J., Gao, G., Pullen, S. S., Jain, V., Gregory, S., Abdelmalek, M. F., & Diehl, A. M. (2025). Targeting senescent hepatocytes for treatment of metabolic dysfunction-associated steatotic liver disease and multi-organ dysfunction. *Nature Communications*, *16*(1), 3038.

El Maï, M., Marzullo, M., de Castro, I. P., & Ferreira, M. G. (2020). Opposing p53 and mTOR/AKT promote an in vivo switch from apoptosis to senescence upon telomere shortening in zebrafish. *eLife*, *9*. https://doi.org/10.7554/eLife.54935

Franceschi, C., & Campisi, J. (2014). Chronic inflammation (inflammaging) and its potential contribution to age-associated diseases. *The Journals of Gerontology. Series A, Biological*

Sciences and Medical Sciences, *69 Suppl 1*, S4–S9.

Gasek, N. S., Kuchel, G. A., Kirkland, J. L., & Xu, M. (2021). Strategies for targeting senescent cells in human disease. *Nature Aging*, *1*(10), 870–879.

Gold, N. M., Ding, Q., Yang, Y., Pu, S., Cao, W., Ge, X., Yang, P., Okeke, M. N., Nisar, A., Pan, Y., Luo, Q., Wang, X., Xu, H., Tian, R., Zi, M., Zhang, X., Li, S., & He, Y. (2025). Therapeutic potential of nicotinamide and ABT263 in alcohol-associated liver disease through targeting cellular senescence. *MedComm*, *6*(2), e70086.

Grosse, L., Wagner, N., Emelyanov, A., Molina, C., Lacas-Gervais, S., Wagner, K.-D., & Bulavin, D. V. (2020). Defined p16 Senescent Cell Types Are Indispensable for Mouse Healthspan. *Cell Metabolism*, *32*(1), 87–99.e6.

Gulen, M. F., Samson, N., Keller, A., Schwabenland, M., Liu, C., Glück, S., Thacker, V. V., Favre, L., Mangeat, B., Kroese, L. J., Krimpenfort, P., Prinz, M., & Ablasser, A. (2023). cGAS-STING drives ageing-related inflammation and neurodegeneration. *Nature*, *620*(7973), 374–380.

Hall, B. M., Balan, V., Gleiberman, A. S., Strom, E., Krasnov, P., Virtuoso, L. P., Rydkina, E., Vujcic, S., Balan, K., Gitlin, I. I., Leonova, K. I., Consiglio, C. R., Gollnick, S. O., Chernova, O. B., & Gudkov, A. V. (2017). *p16(Ink4a) and senescence-associated β-galactosidase can be induced in macrophages as part of a reversible response to physiological stimuli*. https://doi.org/10.18632/aging.101268

Hall, B. M., Balan, V., Gleiberman, A. S., Strom, E., Krasnov, P., Virtuoso, L. P., Rydkina, E., Vujcic, S., Balan, K., Gitlin, I., Leonova, K., Polinsky, A., Chernova, O. B., & Gudkov, A. V. (2016). *Aging of mice is associated with p16(Ink4a)- and β-galactosidase-positive macrophage accumulation that can be induced in young mice by senescent cells*.

https://doi.org/10.18632/aging.100991

Hannou, S. A., Wouters, K., Paumelle, R., & Staels, B. (2015). Functional genomics of the CDKN2A/B locus in cardiovascular and metabolic disease: what have we learned from GWASs? *Trends in Endocrinology and Metabolism: TEM*, *26*(4), 176–184.

Hashimoto, D., Chow, A., Noizat, C., Teo, P., Beasley, M. B., Leboeuf, M., Becker, C. D., See, P., Price, J., Lucas, D., Greter, M., Mortha, A., Boyer, S. W., Forsberg, E. C., Tanaka, M., van Rooijen, N., García-Sastre, A., Stanley, E. R., Ginhoux, F., … Merad, M. (2013). Tissue-resident macrophages self-maintain locally throughout adult life with minimal contribution from circulating monocytes. *Immunity*, *38*(4), 792–804.

Haston, S., Gonzalez-Gualda, E., Morsli, S., Ge, J., Reen, V., Calderwood, A., Moutsopoulos, I., Panousopoulos, L., Deletic, P., Carreno, G., Guiho, R., Manshaei, S., Gonzalez-Meljem, J. M., Lim, H. Y., Simpson, D. J., Birch, J., Pallikonda, H. A., Chandra, T., Macias, D., … Martinez-Barbera, J. P. (2023). Clearance of senescent macrophages ameliorates tumorigenesis in KRAS-driven lung cancer. *Cancer Cell*, *41*(7), 1242–1260.e6.

Hayek, M. G., Mura, C., Wu, D., Beharka, A. A., Han, S. N., Paulson, K. E., Hwang, D., & Meydani, S. N. (1997). Enhanced expression of inducible cyclooxygenase with age in murine macrophages. *Journal of Immunology (Baltimore, Md. : 1950)*, *159*(5), 2445–2451.

Igelmann, S., Lessard, F., Uchenunu, O., Bouchard, J., Fernandez-Ruiz, A., Rowell, M.-C., Lopes-Paciencia, S., Papadopoli, D., Fouillen, A., Ponce, K. J., Huot, G., Mignacca, L., Benfdil, M., Kalegari, P., Wahba, H. M., Pencik, J., Vuong, N., Quenneville, J., Guillon, J., … Ferbeyre, G. (2021). A hydride transfer complex reprograms NAD metabolism and bypasses senescence. *Molecular Cell*, *81*(18), 3848–3865.e19.

Jiang, D., Sun, W., Wu, T., Zou, M., Vasamsetti, S. B., Zhang, X., Zhao, Y., Phillippi, J. A.,

Sawalha, A. H., Tavakoli, S., Dutta, P., Florentin, J., Chan, S. Y., Tollison, T. S., Di Wu, Cui, J., Huntress, I., Peng, X., Finkel, T., & Li, G. (2022). Post-GWAS functional analysis identifies CUX1 as a regulator of p16 and cellular senescence. *Nature Aging*, *2*(2), 140–154.

Karimian, K., Groot, A., Huso, V., Kahidi, R., Tan, K.-T., Sholes, S., Keener, R., McDyer, J. F., Alder, J. K., Li, H., Rechtsteiner, A., & Greider, C. W. (2024). Human telomere length is chromosome end-specific and conserved across individuals. *Science (New York, N.Y.)*, *384*(6695), 533–539.

Kumar, P., Hassan, M., Tacke, F., & Engelmann, C. (2026). Mitochondria-endoplasmic reticulum contact sites in hepatocytic senescence. *Cellular & Molecular Biology Letters*, *31*(1), 13.

Lanna, A., Vaz, B., D'Ambra, C., Valvo, S., Vuotto, C., Chiurchiù, V., Devine, O., Sanchez, M., Borsellino, G., Akbar, A. N., De Bardi, M., Gilroy, D. W., Dustin, M. L., Blumer, B., & Karin, M. (2022). An intercellular transfer of telomeres rescues T cells from senescence and promotes long-term immunological memory. *Nature Cell Biology*, *24*(10), 1461–1474.

Le, P., Tatar, M., Dasarathy, S., Alkhouri, N., Herman, W. H., Taksler, G. B., Deshpande, A., Ye, W., Adekunle, O. A., McCullough, A., & Rothberg, M. B. (2025). Estimated Burden of Metabolic Dysfunction-Associated Steatotic Liver Disease in US Adults, 2020 to 2050. *JAMA Network Open*, *8*(1), e2454707.

Li, C., Xie, N., Li, Y., Liu, C., Hou, F. F., & Wang, J. (2019). N-acetylcysteine ameliorates cisplatin-induced renal senescence and renal interstitial fibrosis through sirtuin1 activation and p53 deacetylation. *Free Radical Biology & Medicine*, *130*, 512–527.

Liebig, J. K., Kuphal, S., & Bosserhoff, A. K. (2020). HuRdling Senescence: HuR Breaks BRAF-Induced Senescence in Melanocytes and Supports Melanoma Growth. *Cancers*, *12*(5). https://doi.org/10.3390/cancers12051299

Li, S., Livingston, M. J., Ma, Z., Hu, X., Wen, L., Ding, H.-F., Zhou, D., & Dong, Z. (2023). Tubular cell senescence promotes maladaptive kidney repair and chronic kidney disease after cisplatin nephrotoxicity. *JCI Insight*, *8*(8). https://doi.org/10.1172/jci.insight.166643

Liu, X.-L., Ding, J., & Meng, L.-H. (2018). Oncogene-induced senescence: a double edged sword in cancer. *Acta Pharmacologica Sinica*, *39*(10), 1553–1558.

López-Domínguez, J. A., Rodríguez-López, S., Ahumada-Castro, U., Desprez, P.-Y., Konovalenko, M., Laberge, R.-M., Cárdenas, C., Villalba, J. M., & Campisi, J. (2021). transcript variant 2 is a marker of aging and cellular senescence. *Aging*, *13*(10), 13380–13392.

López-Otín, C., Blasco, M. A., Partridge, L., Serrano, M., & Kroemer, G. (2023). Hallmarks of aging: An expanding universe. *Cell*, *186*(2), 243–278.

Lu, A. T., Fei, Z., Haghani, A., Robeck, T. R., Zoller, J. A., Li, C. Z., Lowe, R., Yan, Q., Zhang, J., Vu, H., Ablaeva, J., Acosta-Rodriguez, V. A., Adams, D. M., Almunia, J., Aloysius, A., Ardehali, R., Arneson, A., Baker, C. S., Banks, G., … Horvath, S. (2023). Universal DNA methylation age across mammalian tissues. *Nature Aging*, *3*(9), 1144–1166.

Martínez-Zamudio, R. I., Stefa, A., Nabuco Leva Ferreira Freitas, J. A., Vasilopoulos, T., Simpson, M., Doré, G., Roux, P.-F., Galan, M. A., Chokshi, R. J., Bischof, O., & Herbig, U. (2023). Escape from oncogene-induced senescence is controlled by POU2F2 and memorized by chromatin scars. *Cell Genomics*, *3*(4), 100293.

Martin, G. M., Sprague, C. A., & Epstein, C. J. (1970). Replicative life-span of cultivated human cells. Effects of donor's age, tissue, and genotype. *Laboratory Investigation; a Journal of Technical Methods and Pathology*, *23*(1), 86–92.

Mastoridou, E. M., Goussia, A. C., Kataki, A., Koniaris, E., Glantzounis, G. K., Papoudou-Bai,

A., Kanavaros, P., & Charchanti, A. V. (2026). The Interplay Between Cellular Senescence and Lipid Metabolism in the Progression of Metabolic Dysfunction-Associated Steatotic Liver Disease (MASLD). *International Journal of Molecular Sciences*, *27*(2). https://doi.org/10.3390/ijms27021066

McHugh, D., Sun, B., Gutierrez-Muñoz, C., Hernández-González, F., Mellone, M., Guiho, R., Duran, I., Pombo, J., Pietrocola, F., Birch, J., Kallemeijn, W. W., Khadayate, S., Dharmalingam, G., Vernia, S., Tate, E. W., Martínez-Barbera, J. P., Withers, D. J., Thomas, G. J., Serrano, M., & Gil, J. (2023). COPI vesicle formation and N-myristoylation are targetable vulnerabilities of senescent cells. *Nature Cell Biology*, *25*(12), 1804–1820.

Moiseeva, O., Bourdeau, V., Roux, A., Deschênes-Simard, X., & Ferbeyre, G. (2009). Mitochondrial dysfunction contributes to oncogene-induced senescence. *Molecular and Cellular Biology*, *29*(16), 4495–4507.

Muñoz-Espín, D., Cañamero, M., Maraver, A., Gómez-López, G., Contreras, J., Murillo-Cuesta, S., Rodríguez-Baeza, A., Varela-Nieto, I., Ruberte, J., Collado, M., & Serrano, M. (2013). Programmed cell senescence during mammalian embryonic development. *Cell*, *155*(5), 1104–1118.

Muñoz-Lorente, M. A., Cano-Martin, A. C., & Blasco, M. A. (2019). Mice with hyper-long telomeres show less metabolic aging and longer lifespans. *Nature Communications*, *10*(1), 4723.

Ogrodnik, M., Miwa, S., Tchkonia, T., Tiniakos, D., Wilson, C. L., Lahat, A., Day, C. P., Burt, A., Palmer, A., Anstee, Q. M., Grellscheid, S. N., Hoeijmakers, J. H. J., Barnhoorn, S., Mann, D. A., Bird, T. G., Vermeij, W. P., Kirkland, J. L., Passos, J. F., von Zglinicki, T., & Jurk, D. (2017). Cellular senescence drives age-dependent hepatic steatosis. *Nature*

Communications, *8*(1), 15691.

Ohtani, N., Takahashi, A., Mann, D. J., & Hara, E. (2012). Cellular senescence: a double-edged sword in the fight against cancer. *Experimental Dermatology*, *21*, 1–4.

Olan, I., Parry, A. J., Schoenfelder, S., Narita, M., Ito, Y., Chan, A. S. L., Slater, G. S. C., Bihary, D., Bando, M., Shirahige, K., Kimura, H., Samarajiwa, S. A., Fraser, P., & Narita, M. (2020). Transcription-dependent cohesin repositioning rewires chromatin loops in cellular senescence. *Nature Communications*, *11*(1), 6049.

Paffenholz, S. V., Salvagno, C., Ho, Y.-J., Limjoco, M., Baslan, T., Tian, S., Kulick, A., de Stanchina, E., Wilkinson, J. E., Barriga, F. M., Zamarin, D., Cubillos-Ruiz, J. R., Leibold, J., & Lowe, S. W. (2022). Senescence induction dictates response to chemo- and immunotherapy in preclinical models of ovarian cancer. *Proceedings of the National Academy of Sciences of the United States of America*, *119*(5). https://doi.org/10.1073/pnas.2117754119

Park, S. S., Choi, Y. W., Kim, J.-H., Kim, H. S., & Park, T. J. (2021). Senescent tumor cells: an overlooked adversary in the battle against cancer. *Experimental & Molecular Medicine*, *53*(12), 1834–1841.

Peng, X., Wu, Y., Brouwer, U., van Vliet, T., Wang, B., Demaria, M., Barazzuol, L., & Coppes, R. P. (2020). Cellular senescence contributes to radiation-induced hyposalivation by affecting the stem/progenitor cell niche. *Cell Death & Disease*, *11*(10), 854.

Rabhi, N., Desevin, K., Belkina, A. C., Tilston-Lunel, A., Varelas, X., Layne, M. D., & Farmer, S. R. (2022). Obesity-induced senescent macrophages activate a fibrotic transcriptional program in adipocyte progenitors. *Life Science Alliance*, *5*(5).

https://doi.org/10.26508/lsa.202101286

Riley, J. S., Quarato, G., Cloix, C., Lopez, J., O'Prey, J., Pearson, M., Chapman, J., Sesaki, H., Carlin, L. M., Passos, J. F., Wheeler, A. P., Oberst, A., Ryan, K. M., & Tait, S. W. (2018). Mitochondrial inner membrane permeabilisation enables mtDNA release during apoptosis. *The EMBO Journal*, *37*(17). https://doi.org/10.15252/embj.201899238

Roh, K., Noh, J., Kim, Y., Jang, Y., Kim, J., Choi, H., Lee, Y., Ji, M., Kang, D., Kim, M.-S., Paik, M.-J., Chung, J., Kim, J.-H., & Kang, C. (2023). Lysosomal control of senescence and inflammation through cholesterol partitioning. *Nature Metabolism*, *5*(3), 398–413.

Rossiello, F., Jurk, D., Passos, J. F., & di Fagagna F, D. 'adda. (2022). Telomere dysfunction in ageing and age-related diseases. *Nature Cell Biology*, *24*(2). https://doi.org/10.1038/s41556-022-00842-x

Rübe, C. E., Bäumert, C., Schuler, N., Isermann, A., Schmal, Z., Glanemann, M., Mann, C., & Scherthan, H. (2021). Human skin aging is associated with increased expression of the histone variant H2A.J in the epidermis. *NPJ Aging and Mechanisms of Disease*, *7*(1), 7.

Sadhu, S., Decker, C., Sansbury, B. E., Marinello, M., Seyfried, A., Howard, J., Mori, M., Hosseini, Z., Arunachalam, T., Finn, A. V., Lamar, J. M., Jourd'heuil, D., Guo, L., MacNamara, K. C., Spite, M., & Fredman, G. (2021). Radiation-Induced Macrophage Senescence Impairs Resolution Programs and Drives Cardiovascular Inflammation. *Journal of Immunology (Baltimore, Md. : 1950)*, *207*(7), 1812–1823.

Sen, P., Donahue, G., Li, C., Egervari, G., Yang, N., Lan, Y., Robertson, N., Shah, P. P., Kerkhoven, E., Schultz, D. C., Adams, P. D., & Berger, S. L. (2023). Spurious intragenic transcription is a feature of mammalian cellular senescence and tissue aging. *Nature Aging*,

3(4), 402–417.

Silwal, P., Nguyen-Thai, A. M., Mohammad, H. A., Wang, Y., Robbins, P. D., Lee, J. Y., & Vo, N. V. (2023). Cellular Senescence in Intervertebral Disc Aging and Degeneration: Molecular Mechanisms and Potential Therapeutic Opportunities. *Biomolecules*, *13*(4). https://doi.org/10.3390/biom13040686

Sriratanasak, N., Chunhacha, P., Ei, Z. Z., & Chanvorachote, P. (2022). Cisplatin Induces Senescent Lung Cancer Cell-Mediated Stemness Induction via GRP78/Akt-Dependent Mechanism. *Biomedicines*, *10*(11). https://doi.org/10.3390/biomedicines10112703

Suda, K., Moriyama, Y., Razali, N., Chiu, Y., Masukagami, Y., Nishimura, K., Barbee, H., Takase, H., Sugiyama, S., Yamazaki, Y., Sato, Y., Higashiyama, T., Johmura, Y., Nakanishi, M., & Kono, K. (2024). Plasma membrane damage limits replicative lifespan in yeast and induces premature senescence in human fibroblasts. *Nature Aging*, *4*(3), 319–335.

Su, L., Dong, Y., Wang, Y., Wang, Y., Guan, B., Lu, Y., Wu, J., Wang, X., Li, D., Meng, A., & Fan, F. (2021). Potential role of senescent macrophages in radiation-induced pulmonary fibrosis. *Cell Death & Disease*, *12*(6), 527.

Tabula Muris Consortium. (2020). A single-cell transcriptomic atlas characterizes ageing tissues in the mouse. *Nature*, *583*(7817), 590–595.

Tarumi, W., Murai, K., Nakahata, Y., & Masui, K. (2026). The Paradox of Senescence in Glioblastoma: SASP as an Emerging Cancer Hallmark. *Cancers*, *18*(4). https://doi.org/10.3390/cancers18040550

Telemaco Contreras Colmenares, M., de Oliveira Matos, A., Henrique Dos Santos Dantas, P., Rodrigues do Carmo Neto, J., Silva-Sales, M., & Sales-Campos, H. (2024). Unveiling the impact of TREM-2 Macrophages in metabolic disorders. *Cellular Immunology*, *405-406*,

104882.

Tewary, G., Freyter, B., Al-Razaq, M. A., Auerbach, H., Laschke, M. W., Kübelbeck, T., Kolb, A., Mangelinck, A., Mann, C., Kramer, D., & Rübe, C. E. (2024). Immunomodulatory Effects of Histone Variant H2A.J in Ionizing Radiation Dermatitis. *International Journal of Radiation Oncology, Biology, Physics*, *118*(3), 801–816.

Victorelli, S., Salmonowicz, H., Chapman, J., Martini, H., Vizioli, M. G., Riley, J. S., Cloix, C., Hall-Younger, E., Machado Espindola-Netto, J., Jurk, D., Lagnado, A. B., Sales Gomez, L., Farr, J. N., Saul, D., Reed, R., Kelly, G., Eppard, M., Greaves, L. C., Dou, Z., … Passos, J. F. (2023). Apoptotic stress causes mtDNA release during senescence and drives the SASP. *Nature*, *622*(7983), 627–636.

Villot, R., Poirier, A., Bakan, I., Boulay, K., Fernández, E., Devillers, R., Gama-Braga, L., Tribouillard, L., Gagné, A., Duchesne, É., Caron, D., Bérubé, J.-S., Bérubé, J.-C., Coulombe, Y., Orain, M., Gélinas, Y., Gobeil, S., Bossé, Y., Masson, J.-Y., … Laplante, M. (2021). ZNF768 links oncogenic RAS to cellular senescence. *Nature Communications*, *12*(1), 4841.

Vu, H., Sun, Y., Xiong, Z., Tan, X., Radford-Smith, D., Causer, A., Dickens, A. M., Hyötyläinen, T., Evstafev, I., Oresic, M., Nefzger, C., O'Sullivan, E. D., Watt, M. J., Ramm, G. A., Clouston, A., Irvine, K. M., Nguyen, Q. H., & Powell, E. E. (2026). Progressive fibrosis in human MASLD is associated with spatially linked transcriptomic signatures of metabolic reprogramming and senescence. *JHEP Reports : Innovation in Hepatology*, *8*(2), 101657.

Wang, H., Fu, H., Zhu, R., Wu, X., Ji, X., Li, X., Jiang, H., Lin, Z., Tang, X., Sun, S., Chen, J., Wang, X., Li, Q., Ji, Y., & Chen, H. (2020). BRD4 contributes to LPS-induced macrophage senescence and promotes progression of atherosclerosis-associated lipid uptake. *Aging*,

12(10), 9240–9259.

Wang, L., Hong, W., Zhu, H., He, Q., Yang, B., Wang, J., & Weng, Q. (2024). Macrophage senescence in health and diseases. *Acta Pharmaceutica Sinica. B*, *14*(4), 1508–1524.

Wang, X., Ramos, R., Phan, A. Q., Yamaga, K., Flesher, J. L., Jiang, S., Oh, J. W., Jin, S., Jahid, S., Kuan, C.-H., Nguyen, T. K., Liang, H. Y., Shettigar, N. U., Hou, R., Tran, K. H., Nguyen, A., Vu, K. N., Phung, J. L., Ingal, J. P., … Plikus, M. V. (2023). Signalling by senescent melanocytes hyperactivates hair growth. *Nature*, *618*(7966), 808–817.

West, C. E., Karim, M., Falaguera, M. J., Speidel, L., Green, C. J., Logie, L., Schwartzentruber, J., Ochoa, D., Lord, J. M., Ferguson, M. A. J., Bountra, C., Wilkinson, G. F., Vaughan, B., Leach, A. R., Dunham, I., & Marsden, B. D. (2023). Integrative GWAS and co-localisation analysis suggests novel genes associated with age-related multimorbidity. *Scientific Data*, *10*(1), 655.

Wu, D., Tan, H., Su, W., Cheng, D., Wang, G., Wang, J., Ma, D. A., Dong, G. M., & Sun, P. (2022). MZF1 mediates oncogene-induced senescence by promoting the transcription of p16. *Oncogene*, *41*(3), 414–426.

Wu, T., Wu, Y., Jiang, D., Sun, W., Zou, M., Vasamsetti, S. B., Dutta, P., Leers, S. A., Di, W., & Li, G. (2023). SATB2, coordinated with CUX1, regulates IL-1β-induced senescence-like phenotype in endothelial cells by fine-tuning the atherosclerosis-associated p16 expression. *Aging Cell*, *22*(2), e13765.

Yang, J.-H., Hayano, M., Griffin, P. T., Amorim, J. A., Bonkowski, M. S., Apostolides, J. K., Salfati, E. L., Blanchette, M., Munding, E. M., Bhakta, M., Chew, Y. C., Guo, W., Yang, X., Maybury-Lewis, S., Tian, X., Ross, J. M., Coppotelli, G., Meer, M. V., Rogers-Hammond, R., … Sinclair, D. A. (2024). Loss of epigenetic information as a cause of mammalian

aging. *Cell*, *187*(5), 1312–1313.

Yang, Y., Jn-Simon, N., He, Y., Sun, C., Zhang, P., Hu, W., Tian, T., Zeng, H., Basha, S., Huerta, A. S., Sun, L.-Z., Yin, X.-M., Hromas, R., Zheng, G., Pi, L., & Zhou, D. (2025). A BCL-xL/BCL-2 PROTAC effectively clears senescent cells in the liver and reduces MASH-driven hepatocellular carcinoma in mice. *Nature Aging*, *5*(3), 386–400.

Yousefzadeh, M. J., Flores, R. R., Zhu, Y., Schmiechen, Z. C., Brooks, R. W., Trussoni, C. E., Cui, Y., Angelini, L., Lee, K.-A., McGowan, S. J., Burrack, A. L., Wang, D., Dong, Q., Lu, A., Sano, T., O'Kelly, R. D., McGuckian, C. A., Kato, J. I., Bank, M. P., … Niedernhofer, L. J. (2021). An aged immune system drives senescence and ageing of solid organs. *Nature*, *594*(7861), 100–105.

Zampetidis, C. P., Galanos, P., Angelopoulou, A., Zhu, Y., Polyzou, A., Karamitros, T., Kotsinas, A., Lagopati, N., Mourkioti, I., Mirzazadeh, R., Polyzos, A., Garnerone, S., Mizi, A., Gusmao, E. G., Sofiadis, K., Gál, Z., Larsen, D. H., Pefani, D.-E., Demaria, M., … Gorgoulis, V. G. (2021). A recurrent chromosomal inversion suffices for driving escape from oncogene-induced senescence via subTAD reorganization. *Molecular Cell*, *81*(23), 4907–4923.e8.

Zhang, X., Peng, Y., Yuan, Y., Gao, Y., Hu, F., Wang, J., Zhu, X., Feng, X., Cheng, Y., Wei, Y., Fan, X., Xie, Y., Lv, Y., Ashktorab, H., Smoot, D., Li, S., Meltzer, S. J., Hou, G., & Jin, Z. (2020). Histone methyltransferase SET8 is regulated by miR-192/215 and induces oncogene-induced senescence via p53-dependent DNA damage in human gastric carcinoma cells. *Cell Death & Disease*, *11*(10), 937.

Zhao, J., Zhang, L., Lu, A., Han, Y., Colangelo, D., Bukata, C., Scibetta, A., Yousefzadeh, M. J., Li, X., Gurkar, A. U., McGowan, S. J., Angelini, L., O'Kelly, R., Li, H., Corbo, L., Sano, T.,

Nick, H., Pola, E., Pilla, S. P. S., … Robbins, P. D. (2020). ATM is a key driver of NF-κB-dependent DNA-damage-induced senescence, stem cell dysfunction and aging. *Aging*, *12*(6), 4688–4710.

Zhou Y. Z., Xia Z. Y., Wang M. D., & Yang J. W. (2026). [The role of aging in degenerative temporomandibular joint diseases: from cellular senescence to systemic imbalance]. *Zhonghua kou qiang yi xue za zhi = Zhonghua kouqiang yixue zazhi = Chinese journal of stomatology*, *61*(3), 430–439.

Ziegler, D. V., Martin, N., & Bernard, D. (2021). Cellular senescence links mitochondria-ER contacts and aging. *Communications Biology*, *4*(1), 1323.